NORTHWESTERN UNIVERSITY

Structural and Chemical Investigations of Nanotribology Using *In Situ* Transmission Electron Microscopy and Defect Based Analytical Modeling

A DISSERTATION

SUBMITTED TO THE GRADUATE SCHOOL
IN PARTIAL FULFILLMENT OF THE REQUIREMENTS

for the degree

DOCTOR OF PHILOSOPHY

Field of Materials Science and Engineering

By

Ariel M'ndange-Pfupfu

EVANSTON, ILLINOIS

December 2012

ABSTRACT

Structural and Chemical Investigations of Nanotribology Using *In Situ* Transmission Electron Microscopy and Defect Based Analytical Modeling

Ariel M'ndange-Pfupfu

A combination of structural and chemical investigations into nanoscale tribological processes were carried out both experimentally and theoretically. Using *in situ* transmission electron microscopy (TEM) techniques, imaging and spectroscopy were performed in real time on a sliding contact. Uniquely, this approach allows for direct, comprehensive observations of tribological phenomena and an unprecedented amount of quantification. Sliding-induced changes in the carbon bonding structure were observed in amorphous hydrogenated "N3FC" diamond-like carbon films. Taking into account electron beam effects, the rate of the transformation from sp^3- to sp^2-hybridized bonding was quantified as between 0.009% and 0.018% of the sampled film volume per sliding pass, and discovered not to be limited to the surface. Further investigations of these samples using an environmental TEM to apply various pressures of N_2 and H_2 gas showed that the same bonding phase transformation occured more rapidly than the vacuum experiments. In addition, in 0.15 torr N_2, significant amounts of sliding-induced tribochemical wear were observed in regions of the surface highly localized to where the sliding contact was made, totaling approximately $1.2 \times 10^6 \, nm^3$ of lost material over 100 sliding passes. The same experiments in H_2 showed little discernible wear, and the differences in surface chemical activity are discussed.

Separately, traditionally bulk defect theory was used to examine the role of dislocations in crystalline nanotribology. A model was developed to calculate the shear and plowing

components of friction in a model system: the shear component being due to the drag of misfit

dislocations and the plowing component due to creep-mediated deformation around the asperity.

Asperity velocity, shape, and normal load dependence are discussed in addition to thermal

effects. Furthermore, the role of mobile arrays of dislocations is examined with regards to the

shielding effects such arrays would experience from directional phonon drag. For the relevant

range of scattering angles and cross-sections, the adjustment due to shielding is calculated to be

6-25%, small enough that the widely used single dislocation approximation can be considered

valid. These sorts of multifaceted approaches to tribology are necessary if we want to continue

developing our understanding at a fundamental level.

Acknowledgements

The work described in this dissertation was far from an individual effort, and I want to first acknowledge the many people who have contributed in a variety of ways to making this possible. My advisor Laurie Marks has shown amazing levels of patience, insight, and wisdom, without which I would have found it hard to focus my efforts. I appreciate the encouragement to develop not just research skills but presentation, writing, outreach, networking, and in general the tools necessary to become a good all-around scientist. Along with funding from the NSF, DoE, AFOSR, and Northwestern NSEC program, I was well supported during these years, and I am thankful for that. I am also grateful to my defense committee – Prof. Lincoln Lauhon, Prof. Peter Voorhees, and Prof. Leon Keer for showing interest in my work and the unique perspectives they bring to it.

Much of my experiments were performed in collaboration with government laboratories, specifically the Electron Microscopy Center at Argonne National Laboratory and the Center for Functional Nanomaterials at Brookhaven National Laboratory. Without these facilities and their staff – Dr. Russ Cook and Dr. Jim Ciston in particular – I would have found the technical aspect of these projects much more challenging. Dr. Shuyou Li also provided invaluable assistance at Northwestern's EPIC TEM facility. Dr. Osman Eryilmaz and Dr. Ali Erdemir at Argonne provided me with the DLC samples discussed in Chapters 4 and 5, as well as their insights and ideas, both of which were priceless. I must also thank Nanofactory Instruments for providing

support for the *in situ* TEM sample holder, and of course Dr. Arno Merkle for his advice and counsel on its operation.

Last but not least are those who have enriched my life outside the microscope room, who have truly inspired me when the work was at its most difficult, and who I have grown with as a person. To the past and current members of the Marks Group, including Arno, Jim, Jim, Andrés, Danielle, Emilie, Yougui, Yifeng, Betty, Yuyuan, Chuandao, Deniz, Emily, and Shuangping, thank you for your camaraderie and the fruitful discussions. To the administrators of Northwestern's Materials Science program, especially Molli and Peggy, it has meant the world to me how willing you have been to help me out. To my good friends Katie, Sheldon, Matt, Louise, Lisette, and Jane, I hope to see you soon and often. To Jon and Maggie, thanks for always making me feel at home even thousands of miles away. To the members of the Materials Science intramural hockey team, we'll get it next year. To everyone in SPG improv, I'm not really sure what to say. And to Cari, it would take longer than a doctoral program to fully explain why I'm grateful for your presence in my life. I can only look forward to the opportunity.

I want to thank my brothers and parents for their limitless support and love, which I have always counted on since I was old enough to realize it. I am not planning on pursuing a second PhD, but I take everything you say very seriously and I could not ask for a better family.

Table of Contents

List of Tables

List of Figures

Chapter 1

Introduction

1.1 History of Tribology

Tribology is an old discipline that has recently been seeing an increase in attention. Like other fields of science and engineering, interest waxes and wanes cyclically over the years, but tribology has the distinction of being truly historic, with evidence of its importance stretching back to Ancient Egypt, as shown in Figure 1.1. [1] This is because tribologists are concerned with fundamental, practical questions: what occurs at the interface between two surfaces in relative motion, and how can the sliding contact be controlled to affect the behavior of the system?
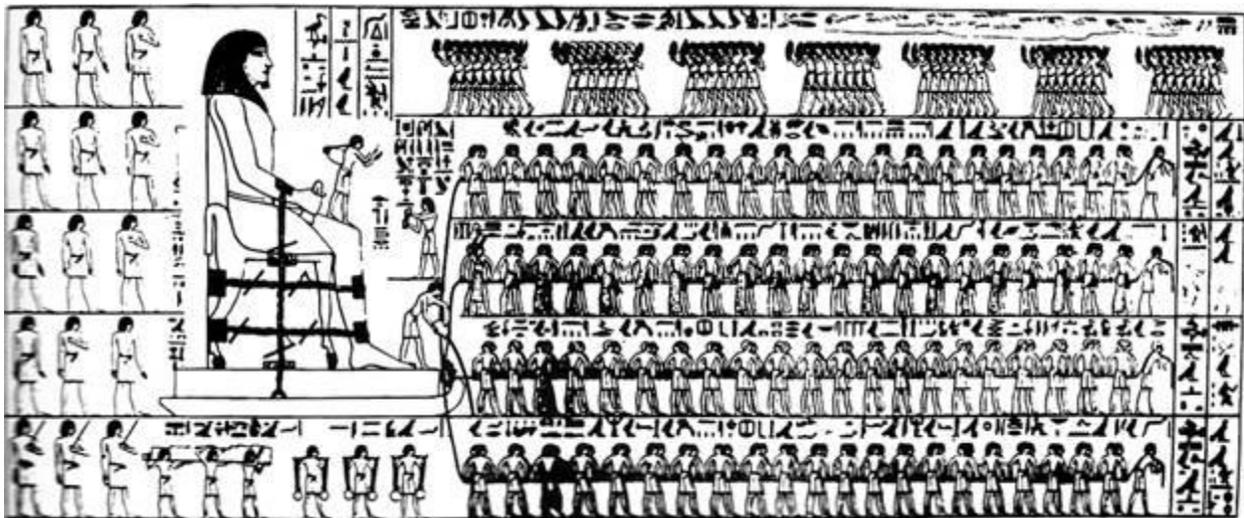
Figure 1.1. Painting from the tomb of Tehuti-Hetep, circa 1880 B.C. The properties of friction were appreciated in the ancient Sumerian and Egyptian civilizations. The man at the foot of the statue is pouring a lubricant, probably oil, to make the statue easier to slide. [1]

Answering these questions remains important today, in a wide variety of applications and for a number of reasons. With the current global focus on energy savings, wasteful processes have come under particular scrutiny. In fact, economic considerations were the impetus behind the coining of the word tribology to refer to the study of friction, wear, lubrication, and related areas. Studies over the past forty years estimate that 4-5% of industrialized countries' gross domestic product is consumed by tribological losses, which can happen at any stage of the lifetime of a device, from manufacturing to operation. [2-4] Of particular importance in this context are the dissipation and waste of applied energy due to friction, and the loss of material at the interface due to wear, which accumulates to decrease the usable lifespan of components.

These problems have traditionally been addressed with both practical and theoretical approaches. Both empirical observation and simple trial and error have undoubtedly resulted in significant advances over time. However, as stricter demands on performance are placed on modern devices, the inefficiencies of this approach become untenable. As a result, there is currently a keen interest in the scientific analysis of tribology.

Leonardo da Vinci is considered the first to propose rules for friction in this vein. His two laws of friction, rediscovered by Amontons in 1699 (along with a third contribution by Coulomb) form the basis of what is still taught in introductory physics classes:

(1) $F = \mu F_N$

(2) $F \not\propto A$

(3) $F \not\propto v$

Here F is the friction force, μ is a scalar coefficient of friction, F_N is the normal force, A is the contact area, and v is the relative velocity between the surfaces. The first law, then, stipulates a linear relationship between the applied normal force and the resulting friction, and the second and third laws claim the independence of friction from the size and velocity of the contact, respectively (illustrated in Figure 1.2). These theories remain useful as estimations in many cases, especially at the macroscale. Classroom experiments done with a stopwatch, a book, and an inclined plane will still conform to the three laws, as neither contact area nor sliding velocity will seem to affect the result whereas normal force will. The laws do not explain the reasons behind the behavior, however: the causes for friction and wear at a fundamental level. It was not until 1950, when Bowden and Tabor proposed the asperity model, that scientists began to see the limitations of these famous laws and where the search for the origins of friction would lead.
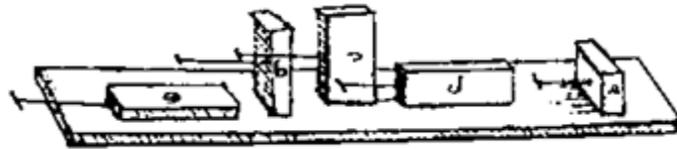
Figure 1.2. Sketches from the Codex Atlanticus and Codex Arundel showing Leonardo da Vinci's studies of the contact area dependence of friction. [1]

Bowden and Tabor's realization was that contact between two surfaces was in fact made by the many microscopic asperities that come about due to surface roughness. This elucidated the role of the normal force (it causes more asperities to come into contact) as well as why macroscopic contact area did not seem to matter (the true contact area of asperity tips is so small as to be imperceptibly different at different orientations). While this idea enabled the development of new engineering methods such as elastohydrodynamic and boundary lubrication, it also made a deeper claim: that the origins of frictional losses were to be found at the

microscale, at the level of the asperity itself, with macroscale friction simply being a cumulative effect of many small interactions. With this in mind, and the advent and perfection of technologies and experimental methods capable of probing not just the microscale but nano- and atomic-scale surfaces as well, scientists have been able to study tribology more carefully and in more detail than ever before.

What has been discovered in recent years, in general, is that tribology is extremely complicated. The frictional force in most cases cannot be described by a single set of equations, it is the result of many forces acting in different ways in response to stimuli which are interdependent. Furthermore, tribological deformation mechanisms depend crucially on the materials involved and just as strongly on the environment in which they're being tested. The materials themselves have properties which change at the nanoscale, often as a function of how the material sample is created. Yet another factor is that tribological interactions occur at the surface, which behaves quite differently than the well-studied bulk. Indeed, as the scale of interest shrinks, so does the surface-to-volume ratio, and surface effects – including tribology – become proportionally more important as a determinant of behavior. Chapter 2 will outline a brief summary of recent theoretical developments and surface sensitive experimental techniques that have been used to approach what is now known to be a complex problem.

1.2 Objectives of this Research

The product of rapidly advancing technology and methods is the complex and diverse field of nanotribology, which attempts to link tribological performance with nanoscale observations. In many ways, however, we as scientists are still far from a useful understanding of tribology.

Because of its multifaceted nature and the difficulty of observation, experiments tend to expose only part of the picture. For example, the classic buried interface problem refers to the inability to directly observe a sliding interface during the sliding process. In typical experimental techniques, only forces are measurable during the sliding test – the interface itself can only be observed after the fact. This results in many experiments which must leap from the initial conditions to the *post facto* observations, leaving a gap in understanding and forcing the use of assumptions. Similarly, attempts to measure chemical processes that occur during sliding are often disconnected from physical observations, and vice versa.

The aim of this thesis is to address these problems using nontraditional approaches which draw upon materials science as an interdisciplinary tool for tying fundamental material processes to a wide variety of macroscale behavior. Just as materials science combines the perspectives of physics, chemistry, and engineering to form a more comprehensive understanding of the connections between phenomena, the theme of this thesis is the combination of different experimental and theoretical perspectives to form more concrete conclusions about specific tribological phenomena. The wide variety of tribological problems cannot be neatly answered with one or two epiphanies, but a broad look at the field can set the boundaries for a map of tribological phenomena, a map that can be filled in with precise and focused experimentation and calculation. The goal of such a map is not just scientific understanding in its own right, but the increased ability to use prediction rather than trial and error in engineering design, and the opportunity to use tribology in a creative way, not just as a constraint or optimization variable.

1.3 Organization of this Dissertation

I will first review recent nanotribology work utilizing *in situ* transmission electron microscopy (TEM) in Chapter 2. In Chapter 3, I will go through in depth the methods and materials used throughout these studies. The following two chapters will be dedicated to my investigation of the nanotribology of diamond-like carbon thin films using *in situ* scanning probe techniques in a TEM. With the ability to manipulate a single asperity inside the microscope and recreate sliding conditions, I was able to make both direct physical and chemical observations of the behavior of the samples in real time, which led to new conclusions and quantification of the interactions of the probe tip with the sample. Chapter 4 will outline experiments conducted in vacuum with analysis of the changes in carbon bonding in the films as a result of sliding. Chapter 5 will cover experiments done in an environmental TEM with exposure to various types and pressures of gas, and the resulting tribochemical interactions. In the second part of this thesis, I will describe my approaches to theoretical problems. Chapter 6 discusses using a dislocation-based framework to combine the shear and plowing friction experienced by an asperity moving through a crystal into one analytical model. Chapter 7 involves the modeling of the phonon drag on an array of moving dislocations. Chapter 8 considers future directions for these avenues of research. The appendix contains practical advice for experimentation using this particular *in situ* setup.

Chapter 2

Review of *In Situ* TEM Nanotribology Research

2.1 Motivations for *In Situ* Electron Microscopy

Measuring dynamic behavior inside a transmission electron microscope dates back nearly to the first observation of mobile dislocations in the TEM at Cavendish Labs by Whelan and Hirsch in 1956. [5] The electron beam resulted in heating and stresses that changed during their experiment, which resulted in observable dislocation motion. Today, this would not be considered a robust *in situ* test as it lacked a significant degree of control, and indeed from that initial point, developments in *in situ* methods have focused repeatedly on the salient points of control and validity – both self-consistency and comparability to other results.

What I will focus on here are the applications of this approach to the field of tribology. Bringing two counterfaces in contact with each other results in many complex phenomena, and *in situ* TEM provides a unique opportunity to study the contact from both structural and chemical standpoints at the nanoscale. This is a relatively new idea, considering that the field of tribology and *in situ* experimentation both developed around the same time in England. Whether this is due to slow knowledge transfer between fields or because the requisite technology was not mainstream, today tribological experiments are fairly easily done with highly functional sample holders available commercially for a wide number of instruments and techniques. In the case of holders that incorporate scanning probes, they are often borrowed from traditional scanning

probe microscopy (SPM), with modern devices even able to perform scanning tunneling microscopy (STM) or atomic force microscopy (AFM) experiments inside the TEM column. Over time, experiments continue to be refined to have more functionality, better accuracy and precision, greater ease of use, and more robust quantification.

Classic mechanical methods such as tensile, compression, bending, and indentation testing have long been used in conjunction with nanoscale electron microscopy. [6] By manipulating a probe tip inside the microscope, sliding experiments are added to the suite of tools available. However, we will see that whereas in macroscale experiments, one would measure the aggregate friction force or wear; in the TEM individual modes of deformation can be accessed, both mechanical and otherwise. In this review I will consider experimental investigations of several of these deformation mechanisms, looking at each individually but also as a component of the larger picture in tribology.

2.2 Diffusion

Because *in situ* TEM is done at the nanoscale, phenomena peculiar to the nanoscale are often of great interest. Diffusion of certain materials, for instance, takes place extremely rapidly at these small scales, as is taken advantage of in some nanowire growth methods. From a tribological standpoint, diffusion represents a way of deforming a material under stress (mechanical, thermal, or otherwise) and is thus an important topic of study. Lockwood et al. showed that during a cyclic wear test on an aluminum-gallium alloy, enough thermal energy was generated for the ion-implanted gallium layer to diffuse to the surface and phase-separate to form liquid droplets. Using an SPM-TEM sample holder capable of performing a cyclic wear test at 5

μm/s, they slid a diamond probe back and forth normal to the sample plane. After approximately 500 cycles, individual droplets on the order of 10 nanometers were detectable *in situ*, and could be combined and re-separated by the probe tip. The details of the behavior of these droplets are of particular interest from an engineering standpoint, as they form a third body which may significantly affect the tribological properties of the sample. [7]

From a macroscopic standpoint, diffusion represents one component out of many contributors to wear. During cutting or machining, diffusion wear plays a key role in the lifetime of the component, and at higher temperatures it can come to be proportionally more and more significant. During high speed cutting where temperatures can reach upwards of 1000 °C, diffusion wear increases exponentially with temperature. [8] It is therefore remarkable that significant diffusion-controlled tribological changes (migration of Ga to the surface, phase separation, and droplet agglomeration) can occur at room temperature at very small scales, fundamentally altering the properties of the material at a scale much smaller than what is typically observed.

In a similar experiment involving the diffusion of gold, Merkle and Marks showed that liquid like growth behavior in gold thin films is possible at room temperature – again, due to enhanced diffusion at small scales. What he observed was similar to what typically occurs during high temperature thin film growth. In this STM-TEM experiment, a section of gold film formed a meniscus with the tungsten probe tip when the probe was electrically biased to 100 mV, and as the tip was retracted from the sample, a neck region was created. Not only was this observed in real time, but a drag coefficient was estimated by converting the diffusion rate of gold to a viscosity of 1.61 Pa·s, which corresponds to a drag coefficient of 1×10^{-11} N·s·m^{-1} for a contact

area of 0.008 μm^2. While the tip bias does constitute a thermal effect, the Joule heating was

estimated to result in a temperature of 166 °C, well below the melting point of gold (1064 °C).

[9]

In both cases, the conclusion is that the thermodynamics allow for diffusion-controlled

tribological phenomena well below the temperature that they would normally occur at

macroscopically. While some of this is due to small scale effects which greatly accelerate surface

diffusion, it is also evident that the applied mechanical or electrical energy of the asperity tip at

any scale can certainly be dissipated through diffusion mechanisms which have strong

tribological implications.

2.3 Grain Growth and Recrystallization

The modes of deformation exhibited by a material at the nanoscale are crucial to its

macroscale properties and behavior. Defects in crystalline materials such as dislocations are one

such mechanism. However, this category also includes grain boundary sliding, migration,

rotation, etc. Due to the size of grain boundaries and their appearance in the TEM, *in situ*

approaches have proven useful. The study of grain boundaries *in situ* has been done in a variety

of ways including using annealing holders [10], strain holders [11], or even the stress caused by

the electron beam itself. [12] Under any of these conditions, it is possible for a thin film to

exhibit grain migration or growth in order to accommodate the applied stress. Liao et al. used an

STM-TEM holder to perform a tribological test. By sliding a tungsten probe tip on a gold film at

approximately 200 nm/s, he observed both widespread grain growth and rapid recrystallization

of the film in the local region of 0.8 μm around the tip. The recrystallization front velocity was measured to be greater than 3 μm/s. [13]

This work reinforces the idea that tribological contact can produce the same sort of material response as other applied stresses. Interestingly, as opposed to the other approaches, the deformation here was quite localized to the region near where the sliding contact was made. While the change in grain boundary structure will undoubtedly affect the macroscale behavior of the material, the extent to which it is limited to only those areas where asperity-asperity contact has been made is a significant factor.

2.4 Sliding Induced Phase Transformation

Tribology is a dynamic process and therefore the materials involved vary in their properties and behavior over the course of sliding. Microstructural evolution and phase transformations are two possible mechanisms by which a material may change over time, and both have been observed at the macroscale and *in situ*.

Wang et al. looked at the structural evolution of amorphous carbon thin films when contacted by a sharp gold asperity. They are able to visually observe the formation of amorphous carbon nanofilaments (100-200 nm in length, 7-10 nm in diameter) and wear particles as a result of single fracture events by bringing the asperity and sample into contact with an applied velocity of 0.89 μm/s. Upon cyclic lateral loading of the gold fracture surface with the carbon counterface – 10 cycles of 600 nm displacement at 0.1 Hz – they found that the wear exhibited a higher degree of graphitic order, in some cases to the extent of forming a carbon onion structure with an interplanar spacing of 0.334 nm, consistent with {002} graphite fringes. One advantage of this

sort of experiment is that it allows for secondary observations; in this case, that gold nanoparticles were present in the carbon wear debris. [14]

This phenomenon of carbon changing its bonding state in response to applied shear stress was also observed by Merkle and Marks with a similar *in situ* apparatus. They studied amorphous "NFC6" diamond-like carbon (DLC) films using tungsten probes in a STM-TEM sample holder. By repeatedly sliding at approximately 1 μm/s and taking electron energy loss spectra (EELS) every 50-100 cycles, they found that the film's carbon bonding shifted towards a higher proportion of sp^2 hybridized bonding. [15] I continued this approach in vacuum studies of "N3FC" DLC films (discussed in Chapter 4), and using an environmental TEM (discussed in Chapter 5).

These results can be compared to those seen at the macroscale. Liu and Meletis performed macroscale wear testing of diamond-like carbon coated discs using a Ti-6Al-4V alloy tip. The applied load was 10 N (Hertzian stress ~70 MPa) and sliding speed 0.05 m/s. The tests were done at room temperature and atmosphere. When the wear debris was examined inside a TEM, diffraction showed that it had undergone significant ordering compared to the as-deposited DLC film, and using imaging they were able to see small graphitic particles 5-10 nm in diameter. [16] This was by no means the only such experiment to see evidence of this phenomenon. [17-19]

It is therefore no surprise that nanoscale sliding tests can produce a similar effect. As we have established, even though the conversion of metastable as-deposited amorphous carbon to graphite is a thermodynamically favorable process usually thought of as thermally regulated, applied shear stress can provide the system with enough energy to use this transformation as a

dissipation mechanism. However, as I will detail in later chapters, the *in situ* experiments offer

conclusions that macroscale tests do not, namely that the bonding transformation progressed

proportionally to the number of sliding passes, and that the transformation was not just localized

to the wear tracks but that small regions of unordered sp^2 bonding would form dispersed

throughout the sampled volume. The delocalized aspect of this sort of bonding transformation

lies in contrast with the extremely localized grain boundary deformation mechanisms discussed

earlier, and the tribochemical wear mechanisms I will discuss in the following section.

2.5 Wear

There have been many attempts to investigate the processes and mechanisms of wear itself at

the nanoscale, as it has crucial implications for the engineering of virtually all devices with

moving parts. Using AFM, Bhaskaran et al. are able to show atom-by-atom wear in diamond-like

carbon – though because this is not an *in situ* technique, tip shapes need to be modeled *post facto*

in order to back out what deformations have occurred. [20] Still, this work exemplifies the level

of detail to which it is now possible to look at wear, with further work by Jacobs et al. applying

transition state theory to the removal of a single atom of material from a film. [21]

Using *in situ* internal reflection spectroscopy, Olsen et al. investigated the tribochemical

reactions of DLC films at low loads (7.8 kPa). The as-deposited sample was found to contain

carbonyl groups on the surface, which were removed during sliding. The sliding process was

seen to oxidize the surface, forming carbon-oxygen bonds as well as tertiary vinyl groups. The

contact area in these experiments is approximately 200 mm^2, which leaves the door open for *in*

situ scanning probe experiments to more closely look at the nanoscale changes during sliding. [22]

Peng et al. study nanowear on single crystal silicon using AFM, looking at wear tracks and tip structure *post facto*. They coated silicon nitride AFM probes with ~150 nm thick layers of gold and silver, and slid them on a single crystal silicon wafer at a speed of 480 μm/s and an applied load of 504 nN. A field emission SEM was used to measure the tip wear periodically, and they conclude that both the Si-Au and Si-Ag systems exhibit a combination of abrasive and adhesive wear. [23] Nearly the same experiment is performed by Ribeiro et al. using SPM-TEM, where a number of observations of stress contours are made during the experiment, leading to an entirely different perspective of the process and a different model as a result. [24]

The tribochemical aspects of DLC wear in various environments have been well documented experimentally and theoretically. [25-30] Some studies focus on the exact species present in the environment after sliding, others on friction and wear rates, but *in situ* TEM experiments can still contribute by offering detailed EELS spectra showing nanoscale bonding changes coupled with imaging of the same region during a sliding test. [31] Chapter 5 details my own experiments involving tribochemical wear of DLC in different gas environments, where I combine structural and chemical observations to put together a comprehensive picture that fills in the gap between the AFM and macroscale regimes.

Every experimental technique has its strengths and weaknesses, and the strength of *in situ* TEM techniques is to offer a broad tribological perspective that encompasses many different phenomena – from the mechanical action of the probe to real-time defect movement to the

chemical changes that are occurring simultaneously. There are many challenges to be overcome, including quantification, precision/repeatability, electron beam effects, and control of the sample to avoid drift, but as the *in situ* field as a whole matures, its continued applicability to the field of tribology will undoubtedly be refined and extended.

Chapter 3

Methods and Materials

3.1 Modern Experimental Methods

I want to first take a step back and discuss more general experimental approaches to tribology before detailing the method that I used in this research and why. Tribology is a complex, multifaceted problem, and as such it is studied in a wide variety of ways which also differ by field. It is imperative to choose the right approach based on the hypothesis to be tested. In this work I will focus on the fundamental science underlying tribology, as opposed to considering parameters more relevant to engineering. By taking a classic materials science approach, I aim to tie macroscale performance to small scale properties. While many experimental techniques can measure frictional forces, only newer techniques can recreate interfacial contact at a small scale. It is important to consider behavior at the nanoscale in order to learn about fundamental mechanisms, as macroscale behavior is a composite of many factors.
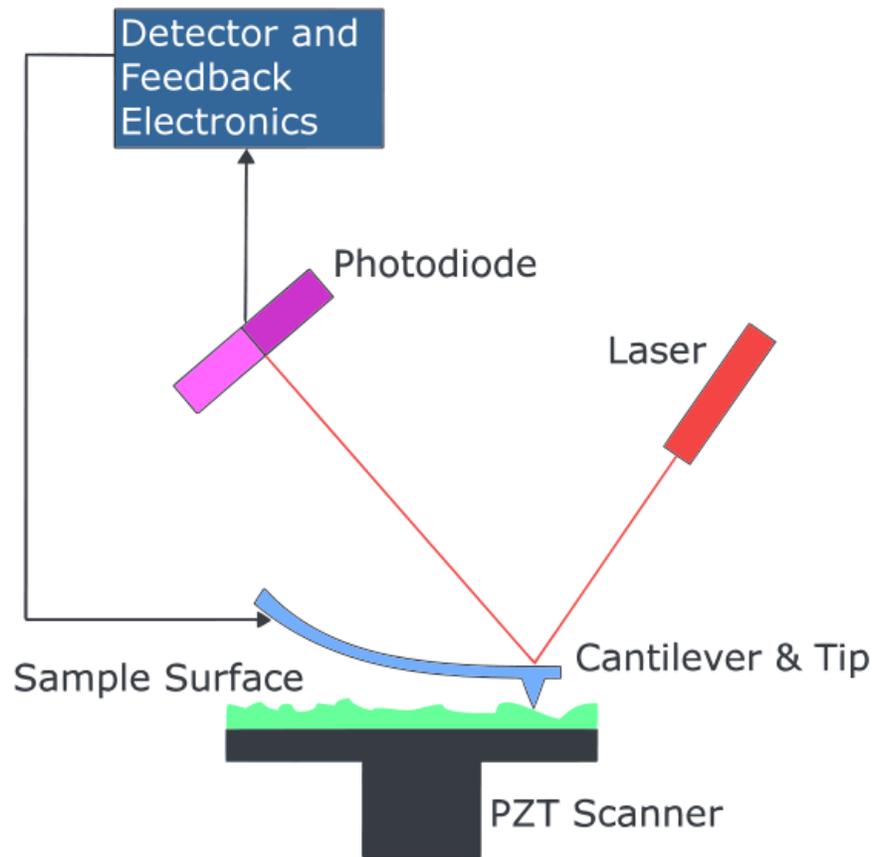
Figure 3.1. Typical schematic of an AFM courtesy of Wikipedia. The tip is rastered along the surface and a 2D image is usually created from either the changing z-position of the tip or the force necessary to maintain a constant height. Other modes are available as well.

Perhaps the most popular approach for small scale study of tribology in recent years has been the AFM and related scanning probe techniques. AFM uses piezoelectrics, cantilevered springs, and optical sensing to take extremely precise measurements. A schematic is shown in Figure 3.1. The probe size in AFM results in a contact area as low as the tens of square nanometers. The ability to perform atomic-scale sliding experiments with a single asperity on a sample resulted in a much more localized view of how friction varied across a sample surface at the nanoscale. An operating mode called lateral force microscopy (LFM) in particular has been useful in mapping friction forces on a sample surface as contrast in an image (see Figure 3.2 for example), and the

ability to see the different behavior of different regions still has the capability to inspire new

realizations and increase our understanding of friction at a fundamental level.
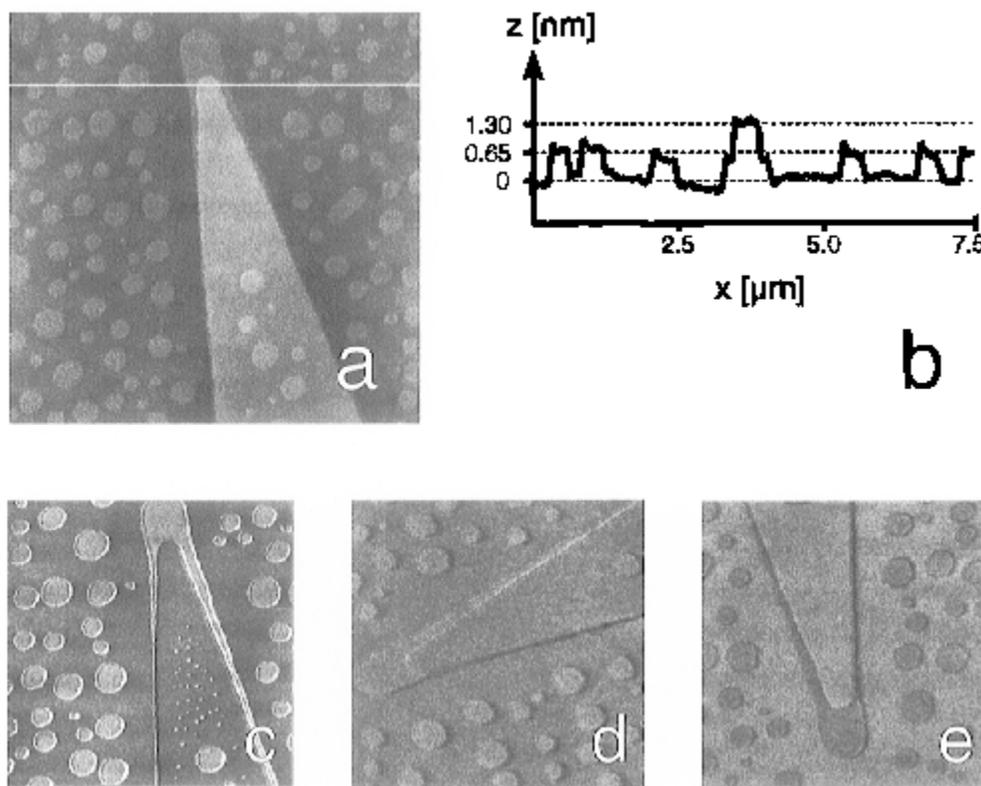
Figure 3.2. Triglycine sulfate studied with lateral force microscopy. (a) is a 7.5 μm^2 topography map while (c), (d), and (e) show friction force scans of the same area at different orientations, highlighting the dependence of friction on the details and directionality of the crystal. [32] (c) Kluwer Academic Publishers 1996

At its core, however, AFM remains quite similar to macroscale tribometer experiments in

that the sliding process itself cannot be observed. The effects of tribology can be seen, and the

phenomena at work inferred, but the only indication of what is actually occurring at the interface

is a graph of the frictional force measurement. This susceptibility to the buried interface problem

leaves something to be desired in terms of being able to simultaneously observe and execute

sliding experiments.

In the past few decades, *in situ* experimentation inside a transmission electron microscope (TEM) began to be feasible. Experiments performed inside the TEM column benefit from the highly spatially resolved micrographs based on the slight interactions and scattering of high energy electrons transmitted through a sample thin enough to be electron transparent. As opposed to simple data collection from samples, this allowed the TEM to become a platform on which a multitude of processes could be investigated.

Technological advances lead to the development of more sophisticated *in situ* TEM sample holders. The Nanofactory HS-100 sample holder holds a standard size 3mm TEM grid, as well as a 0.25 mm diameter probe tip mounted as shown in Figure 3.3 and capable of motion in three dimensions. A bias can be applied through the probe tip, and by measuring the current through the tip the holder can perform current-voltage measurements as well as scanning tunneling microscopy. I chose to use this system for my experiments because the probe tip could also be used as a means of making sliding contact with the sample in a way that would still be visible to the structural and chemical measurements in the TEM. So, for this kind of sliding experiment on electron-transparent thin films, the buried interface problem is avoided and I can observe the sliding interface directly, in real time, while also recording electron diffraction patterns and chemical analysis through electron energy loss spectroscopy (EELS). [33, 34]

Many different imaging modes exist, but in this work I will focus on bright field images comprised from the entirety of the transmitted electron beam. In this case, the primary source of contrast is from diffraction effects. Most electrons will be transmitted without interacting with the sample, but depending on the orientation of the crystal lattice, the distribution of intensities will be affected. In the work described in this thesis, however, the samples are amorphous and

therefore interpretation is somewhat simpler. As the mass and thickness of the sample increases, so does the likelihood of electron scattering, which results in dimmer intensity in the recorded image at that point. So, for samples with nearly homogenous mass, bright field micrographs mostly reflect the film thickness and can be thought of approximately as topography maps.

3.2 *In Situ* STM-TEM

Just as the AFM provides a precise link between the spatial morphology of a sample and its frictional properties, I endeavor to use a scanning probe technique that will create direct and quantifiable connections between different viewpoints: between the initial probe and sample to the wear track produced after the test, between the physical responses to a sliding asperity and the chemical ones, etc. The more solid connections that can be made, the better job the human brain can do at creating a consistent and comprehensive theory.

In this thesis, I approach this goal by using a Nanofactory HS-100 *in situ* TEM sample holder with mounted STM probe and stage for operation inside the TEM column, as shown in Figure 3.3.
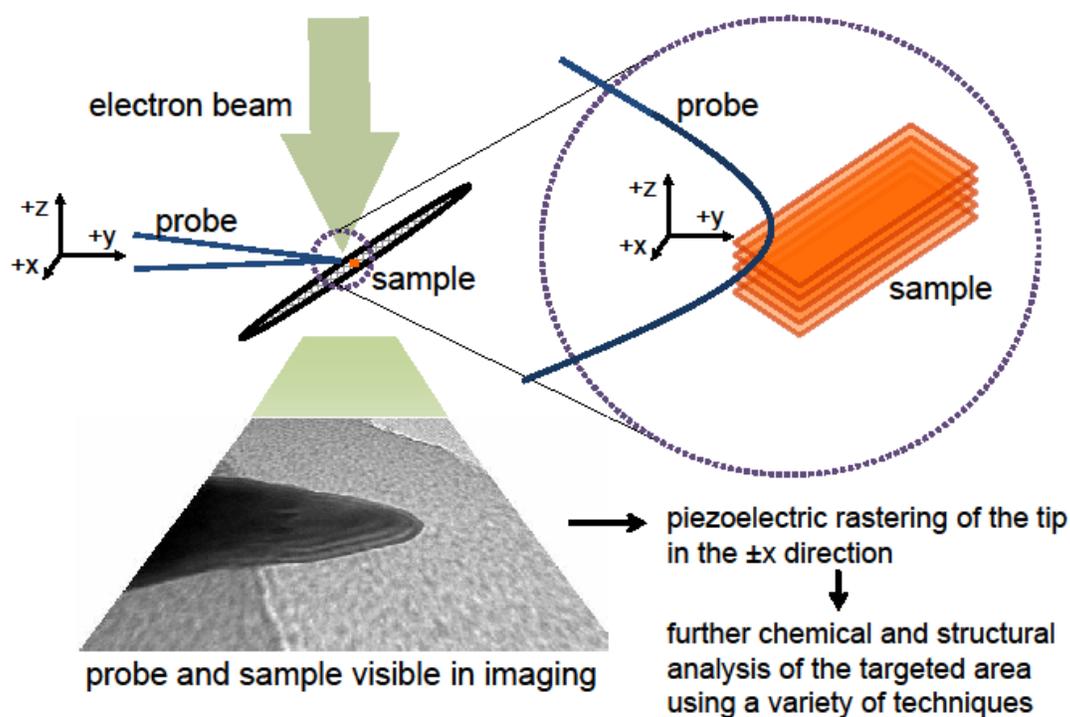
Figure 3.3. Schematic of the Nanofactory HS-100 STM-TEM holder inside the microscope column. The TEM micrograph shown represents a typical view of the probe tip inside the microscope column. The motion directions available to the tip are labeled x, y, and z, and are not absolute coordinates. The sample itself is mounted in a full-size TEM grid rotated 45° about the x-axis as shown, and the sliding is typically done in the $\pm x$ direction.

The scanning probe allows for single asperity contact between a variety of probes and the sample. The probes can be custom made from a variety of materials, in the desired aspect ratio, with radius of curvature as low as 10 nanometers. Samples can be mounted on standard sized 3 mm TEM grids, which can be seen in Figure 3.4. Coarse micrometer-scale motion of the tip is available through a stick slip mechanism and fine, reversible motion on the nanoscale is available through a piezoelectric tube – both controllable via computer. Essentially, the probe can be manipulated in such a way as to perform a repetitive sliding motion in full view inside the microscope column.
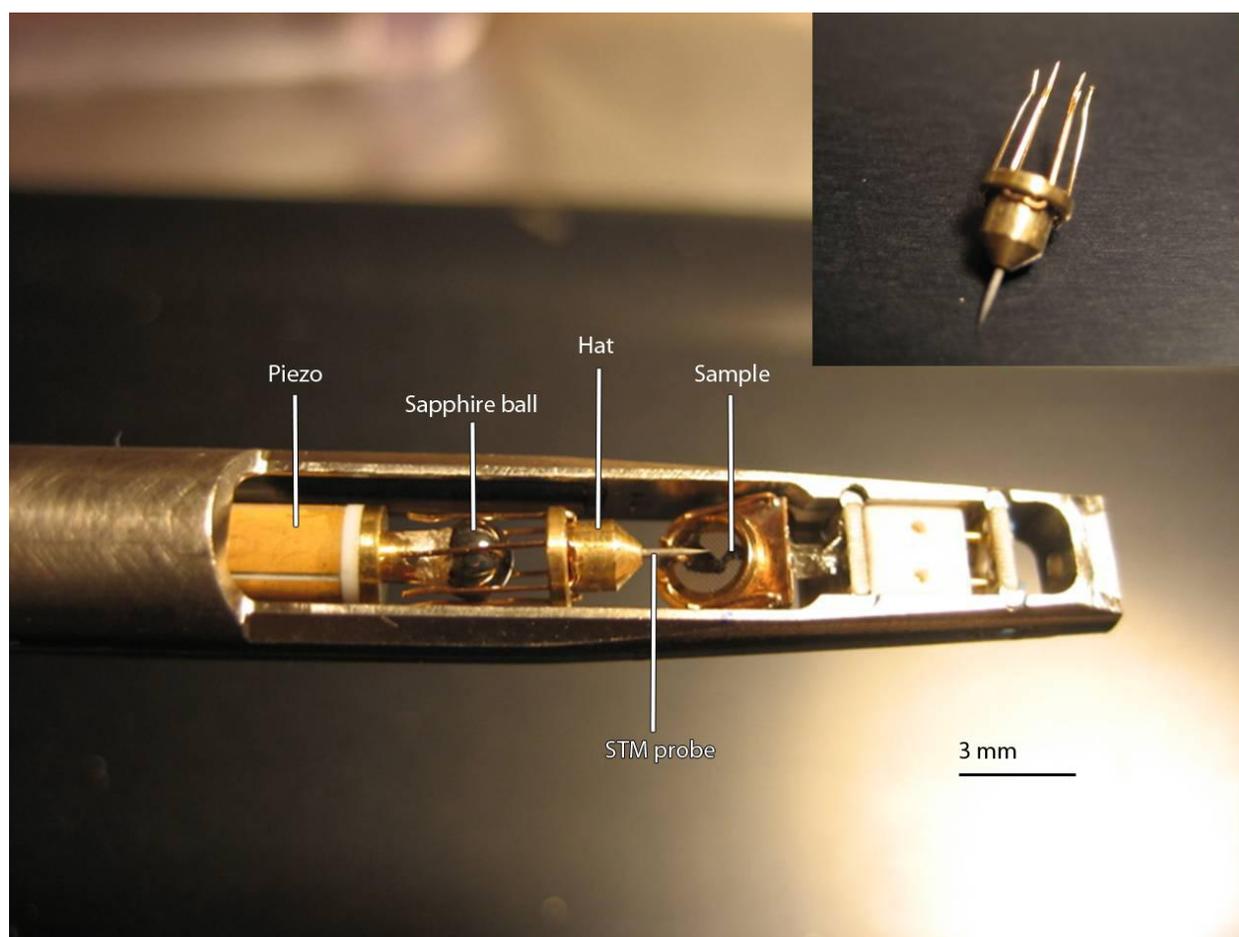
Figure 3.4. Photograph of the tip of the Nanofactory HS-100 STM-TEM sample holder. Shown are the mounted sample, probe, and control mechanisms: piezoelectric tube and a rotatable sapphire ball pulsed for coarse stick-slip motion.

The TEM does not only provide highly spatially resolved imaging and diffraction, but a suite of built in instrumentation including chemical analysis via spectroscopy that can be spatially correlated with the sample images. Overall, this approach results in a comprehensive view of the sample's interaction with the tip and the environment from a number of perspectives. Compared to other experimental techniques, this *in situ* TEM method offers the scale and control of AFM experiments with unprecedented visibility and a number of measurement options. The ability to make direct quantifiable observations of tribological phenomena during sliding is an important

advantage of this approach, and the capability to correlate different types of observations on the same sample with a high degree of spatial resolution provides a strong base on which conclusions can be drawn.

3.3 Experimental Method

There are many practical considerations to successfully performing a sliding test in the microscope. These will be outlined in an appendix; here I will describe the simpler "ideal" experiment.

3.3.1 Sample Selection

For samples, I chose to investigate the behavior of carbon films for a variety of reasons. Carbon in various forms is one of the most common solid lubricants, and graphite has been manufactured and used for this purpose for over a century. More recently, diamond and diamond-like carbon films have been of increasing interest in part because of their desirable tribological properties when used as coatings. DLC is a metastable, amorphous form of carbon that consists of a variable composition of sp^3 hybridized (tetrahedral) carbon, sp^2 hybridized (trigonal) carbon, and hydrogen, ranging up to "pure" tetrahedral amorphous carbon (ta-c) with 100% sp^3 bonding (see Figure 3.5). [35] The significant fraction of diamond-like bonding – as well as the presence of hydrogen as a passivating agent – results in a hard (on the order of 2000-5000 kg mm^{-2} [36]) and chemically nonreactive surface, which contributes to a high resistance to adhesive and abrasive wear. In addition, the ability to form a transfer film during sliding can reduce wear and increase lifetimes in sliding experiments. [37, 38] Good mechanical, chemical,

and tribological properties, as well as its effectiveness as a diffusion barrier combine to make

DLC an attractive coating option for a variety of applications.
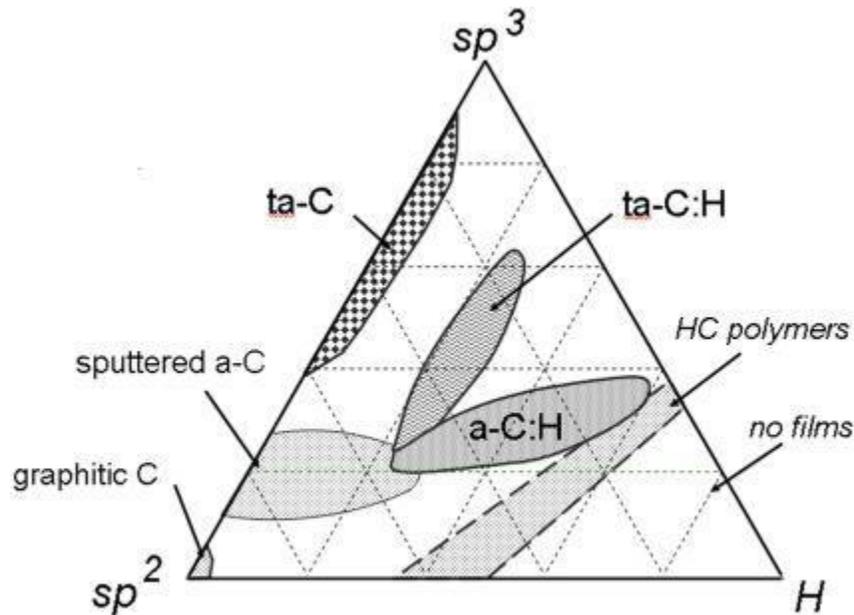
Figure 3.5. Phase map showing the different kinds of depositable carbon films incorporating hydrogen. DLC falls in the middle of the triangle with typical compositions combining sp^2 and sp^3 bonded carbon, and an amorphous structure.

As compared to crystalline diamond coatings which require a high degree of control over the

surface reaction [39, 40], amorphous DLC can be deposited relatively cheaply, with less

difficulty, and in a number of different ways, including sputtering, chemical vapor deposition,

ion beam deposition, and vacuum arc. [36] This flexibility adds to their usefulness as coatings, as

it improves the chances that they can be easily engineered to desired specifications. The

composition varies with deposition method, but the resulting thin film is usually chemically

passivated by hydrogen attachment to dangling bonds. [41]

In vacuum or an inert gas environment both friction and wear are normally very low, as one

would expect from a nonreactive surface with high elastic modulus. Still, much depends on the

deposition method, the exact composition, and the testing environment. [42-44] By varying the environment and the hydrogen content of the film, the coefficient of friction and wear rate can change by several orders of magnitude. [27, 37, 45-51] Interestingly, significant mechanical and chemical changes occur in the film as a result of sliding. Increases in the sp^2/sp^3 bonding ratio after tribotesting have been observed in several macroscale experiments [15, 17, 52-54] and called graphitization due to the observation of graphitic wear particles *post facto.* The formation of tribolayers[55, 56] has also been observed, while *in situ* experiments at the nanoscale indicate a partial transformation of sp^3 bonded carbon to more graphitic sp^2 bonding. [57, 58] Molecular dynamics simulations agree that tribochemistry – the cooperation of mechanical (from sliding) and chemical (from the film or environment) deformation processes – has a large effect on the frictional forces at small scales. [59, 60] This suggests that performance depends not only on initial composition, but on sliding-induced changes.

If we want to thoroughly understand how DLC films interact with counterfaces and the environment during sliding contact, then characterization after the fact is insufficient. Being able to directly observe and characterize both physical and chemical changes in the film in real time during a sliding experiment is a distinct advantage of *in situ* TEM techniques.

Since the sample holder accepts standard 3 mm TEM grids, copper grids with a lacey carbon support film were used. Grids with no carbon support were also tried, but resulted in much easier fracture of the films. The electron beam alone at high doses was enough to cause significant local stresses in the film – this was ameliorated by avoiding high doses and spot focusing the beam, as well as with the lacey carbon backing. Sample films were deposited on crystalline NaCl cubes,

and subsequently floated off in a deionized water bath. From there they were rinsed, placed on

the grid, allowed to dry, and mounted in the sample holder.
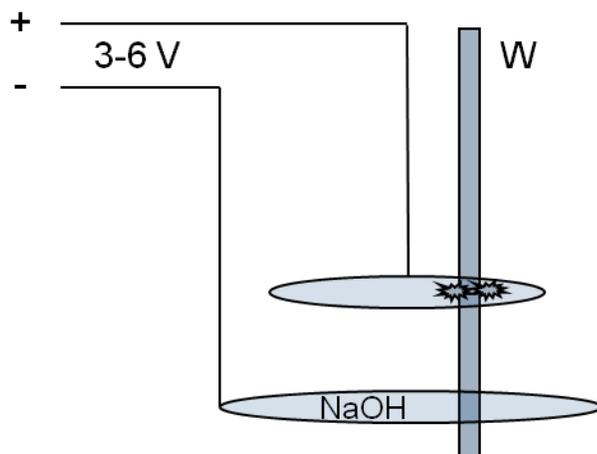
Figure 3.6. Schematic of the electrochemical etching (electropolishing) apparatus. The NaOH solution is held in tension inside loops of gold wire. With an applied bias, etching takes place in the meniscus formed about the vertically placed tungsten wire. When the wire is etched through, the circuit is broken and etching ceases. Both halves of the wire often have usable sharp tips.

3.3.2 Probe Fabrication

The probe tips were electrochemically etched to a sharp point from 0.25 mm tungsten wire

using a solution of 0.5-5 N NaOH. A schematic of the process is shown in Figure 3.6. The aspect

ratio and sharpness of the tips depends on the concentration of the etching solution and the

applied voltage, which was 3-6 V. The sharpness also strongly depends on the shape of the

solution meniscus formed during etching and how quickly the solution can be removed after a tip

is formed. As opposed to the concave aspect ratio typically used in STM for the smallest possible

aspect ratios, I decided to use more conical tips (such as those in Figure 3.7) in order to minimize

the potential for fracture. The sharpest tips used had radii of curvature under 50 nm, as seen in

Figure 3.8.

Figure 3.7. SEM image of prepared tungsten probes showing the desired tip aspect ratio.
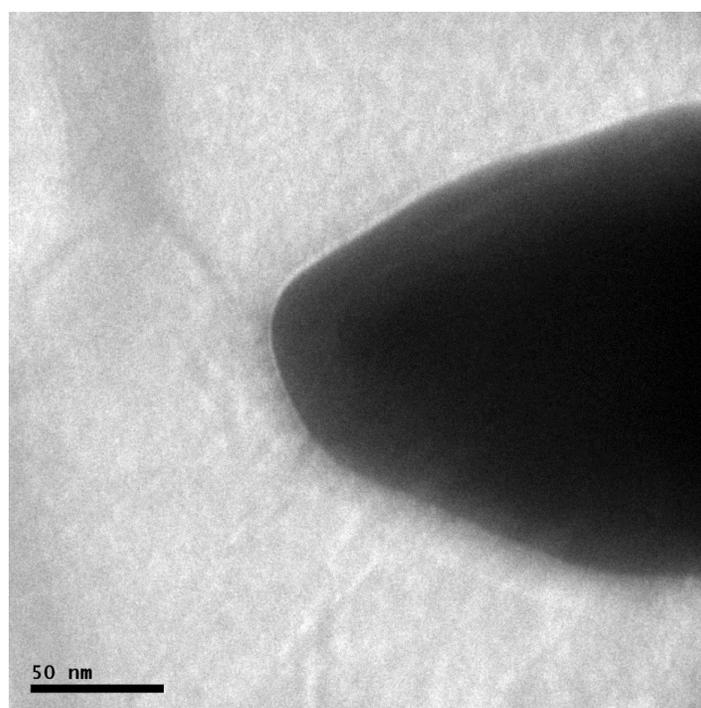
Figure 3.8. TEM micrograph of a typical tungsten probe tip prepared by electrochemical etching.

3.3.3 *In Situ* Sliding Test

Contact was carefully made with the sample by oscillating the high voltage or similar techniques to determine and match up the defocus distances of the probe and sample. I made the sliding contact as delicately as possible in order to limit the mechanisms at work and ease analysis. Adhesive forces caused the tip to snap to the surface when it is in close proximity, and this provided another cue for when contact was made. The tip was then rastered in the $\pm x$ direction (as illustrated in Figure 3.3) using the piezoelectric tube at approximately 2 μm/s. Visual confirmation that sliding is taking place is obtained. Once repeatable sliding passes can be performed without destroying or moving the film, EELS spectra and other measurements can be taken periodically without disturbing the sample or changing the electron dose. Eventually, the film will undergo enough stress that it will tear, delaminate from the grid, roll up, or otherwise deform in such a way that it can no longer be compared to its original state. At this point the sliding test is over.

The possible measurements include electron diffraction patterns, which offer information on long range order in the sample volume, bright field micrographs (including energy filtered (EFTEM) micrographs to increase contrast by filtering out inelastically scattered electrons), video recording, and EELS. Energy-dispersive x-ray spectroscopy (EDX) and dark field imaging (using diffracted electrons) are also possible, but did not prove useful for looking at the sample films in this case, as I investigated primarily diamond-like carbon and other amorphous carbon films.

3.3.4 EELS Measurement

Interpreting electron energy loss spectroscopy measurements is a nontrivial task. Theoretical modeling and accurate quantification efforts are fields of study in and of themselves. In these experiments I avoid much of this complication by focusing on relative changes in the signal, but it is still important to consider the method in depth. First I will briefly describe the origin of the EELS signal, what it measures, and its sensitivity. Second I will discuss some experimental factors, including dose and sample orientation. Lastly I will go through the analysis done, from the raw spectrum to the signal used to make conclusions and the error involved.

When electrons pass through a sample they may undergo inelastic scattering. Interactions with phonons and plasmons are possible, as are electronic band transitions and valence and core ionizations. It is the latter sort of excitation which provides elemental composition information: when a large amount of collected electrons all have energy losses corresponding to the core ionization energy of a certain element, we can deduce that element's presence in the sampled volume and even quantify the amounts in certain cases. As a result, EELS spectra are comprised of a zero-loss peak, which represents unscattered or elastically scattered electrons (the vast majority), a low-loss region which includes plasmonic interaction, and a high-loss region where core ionization edges appear at specific energies, with near edge regions that represent slight deviations from the core energy due to bonding and secondary scattering events.

The resolution of EELS is only limited by the electron beam, so nanometer-scale spatial resolution is possible. The energy resolution can vary but is generally around 0.5 eV. This is sufficient to differentiate between the carbon ionization K-edge resulting from the 1s→σ* transition (290 eV, corresponding to sp^3 bonding), and the 1s→π* edge at 286 eV from sp^2 bonded carbon. It is worth mentioning that the radiation dose can affect the EELS spectrum by

breaking certain types of bonds preferentially. [61] This should be accounted for in any serious

elemental quantification. Similarly, for crystalline samples, the orientation dependence must be

taken into account since anisotropy in the density of states will result in an anisotropic EELS

signal.
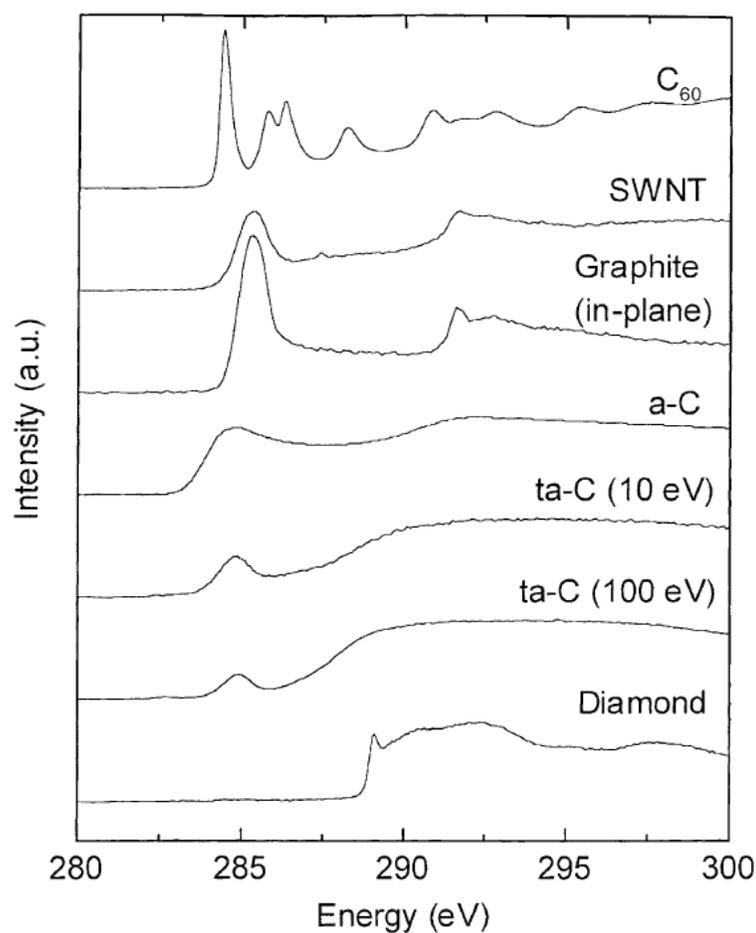
Figure 3.9. EELS carbon K-edge spectra for various forms of carbon, as seen in [62].

In these experiments, I analyze the signal by first subtracting the background using power

law extrapolation, and integrating the remaining signal. To compare specific edges, the integral

is taken from the beginning of the edge to the peak maximum; this will be illustrated later. [63,

64] Gaussian functions were used to fit certain edges in order to consistently compare energy

loss values and full widths at half maximum. Note that these were not used to model the edge shape, as Lorentzian functions are often used for that purpose. When comparing spectra to each other, it is important to normalize the counts, and this is done by comparing a portion of the spectrum that only exhibits background and performing the necessary multiplication.

EELS spectra, being essentially an electron counting process, should generally exhibit noise following Poisson statistics, although the use of a charge-coupled device camera to record the data slightly complicates this. [65] After calculating the statistical and integration error for the measurements, it was found to be negligible in light of the high numbers of counts collected, and the goodness of fits. However, it is safe to assume larger systematic errors on the order of 5-10%. Significant sources of error include the relatively high background levels which must be subtracted, the deconvolution of the signal from the low-loss spectrum, and the count integration. Each of these three processes must be done by the user and lacking clear standards are subject to human variability.

3.4 Modern Theoretical Methods

On the theoretical side, there is a strong history of using modeling to understand friction. Engineering models, such as those of boundary lubrication, have for decades used contact mechanics and geometry to predict frictional behavior in the presence of lubricants. [66-68] While these methods have been successful in predicting phenomena such as stick-slip [69], more fundamental atomistic analysis on a smaller scale is still desirable. An important distinction to make is between atomic and molecular tribology models and analytical modeling. Molecular dynamics and similar first principles models deal rigorously with small scale forces, and in some

cases with enough computing power can simulate all the atomic interactions in a nanoscale

contact for a short time. However, physics alone has difficulty explaining larger conceptual

ideas, and it can be difficult to draw broad conclusions from narrowly focused simulations. By

contrast, analytical modeling attempts to apply established theoretical frameworks to model a

variety of problems. One reason why I use this approach here is to highlight connections between

fields and gain a more comprehensive understanding of the subject from a broader point of view.

3.5 Analytical Dislocation Theory

As part of understanding nanotribology, we need to recognize that atomic-scale interactions,

often involving defects, form the basis for friction and wear at the asperity level. Complicating

this small scale analysis are scale-dependent changes in material behavior that often differ from

the bulk, as well as new deformation mechanisms that may come into play at the nanoscale. Still,

by focusing on dislocation theory we can construct analytical models that use established

dislocation theory and contact geometry to form well supported models of specific kinds of

material deformation with great predictive power.

Deformation of a material due to an applied stress can be broken down into two categories.

Elastic deformation moves the atomic structure into a strained state, but the structure itself is not

permanently affected and no energy is required to move the system back to pre-stress

equilibrium. Plastic deformation involves irreversible structural changes, and precludes adiabatic

processes. This latter case therefore is of primary interest to tribologists. These structural

changes from one equilibrium state to another occur in a manner which minimizes the required

energy. In many cases, this involves the creation, motion, and interaction of defects, which can

accommodate stresses throughout a crystal without large amounts of bonds needing to be broken at once. In particular, analyzing deformation through the characterization and motion of linear defects called dislocations has proven to be a consistently valuable strategy.

Dislocations have long been used as a framework for understanding crystalline materials, particularly under applied stress. It has been found that the properties and interactions of dislocations have a significant effect on macroscale behavior, and dislocation theory has well-established predictive power. This dislocation framework can be extended beyond plastic deformation to include the modeling of more general friction and wear phenomena, including contact mechanics. [70] Using these concepts also gives us new tools and insights useful for analyzing more complicated tribological systems. [71-73] For instance, previous work in my research group has shown that it is feasible to express friction at a crystalline interface in terms of misfit dislocation drag, and in general it is valid to make connections between dislocation drag and dissipative forces at the macroscale. [74]

The dislocation framework extends beyond dislocations themselves to more complicated deformation modes. Grain boundaries are one example of a nanoscale structure with significant implications for macroscale performance, and are often thought of as collections of dislocations. Indeed, deformation by grain boundary rotation, recrystallization, and grain boundary sliding all play a role in the performance of crystalline materials. Modeling these phenomena using dislocation theory allows for analytic solutions that have a wide range of applicability.

Chapter 4

Sliding Induced Transformation of DLC Bonding Structure

4.1 Carbon Bonding in DLC Thin Films

There are several proposed mechanisms for the low friction of hydrogenated DLC films. One possibility is hydrogen termination minimizing adhesive contact, another is the formation of graphitic material either at the surface or within the transfer layer. The latter is of particular interest because graphite formation during sliding has implications for film properties such as wear, friction, and mechanical behavior. [52] Experimentally, so-called "graphitization" has been observed by both chemical and structural observation. [15-17] These experiments show a clear increase in the ratio of sp^2 to sp^3 bonding over the course of sliding experiments, often with *post facto* evidence of graphitic carbon. Less clear is how the changes in sp^2 bonding occur, leaving questions: do large volumes of ordered graphite only form under high stress conditions, are disordered sp^2 bonds likely to form first, is the transformation limited to the surface, etc.

In situ tribology is well suited to answer dynamic questions such as the evolution of sp^3 to sp^2 bonding during sliding. By performing a simple experiment as outlined in Chapter 2, a clear view of the process as it happens can be achieved with structural context. In doing so, I hope to reduce the confusion around the effects of graphitization in DLC. In some studies, low friction is attributed to the formation of a lubricious graphitic layer; in others, increased sp^2 content is seen to adversely affect friction and wear properties. I demonstrate that for the conditions of the

experiment only disordered sp^2 forms, not crystalline graphite, that the transformation is not limited to the surface, and that the sp^2 content is proportional to the number of sliding passes.

4.2 Experimental Details

4.2.1 Sample Preparation

I used a Nanofactory HS-100 Scanning Tunneling Microscopy TEM sample holder to perform the experiment *in situ* inside a Tecnai F20ST TEM at 200 kV and approximately 10^{-7} torr; I used the sliding method outlined in Chapter 3. [13, 15, 75-77] Post-specimen electrons were collected using a Gatan Imaging Filter (GIF) CCD camera.

N3FC "nearly frictionless carbon" thin films were prepared at Argonne National Laboratory using a magnetron sputtering process. The films were deposited onto an NaCl crystal random cutting [18], which was then dissolved in water and the film transferred to a copper TEM grid with a lacey carbon film support. The film thicknesses were measured by EELS to be 30-35 nm by the standard log/log relative method. [78] A typical micrograph and EELS spectrum of film as-deposited can be seen in Figure 4.1.

It is important to note that the growth process and the specific parameters (including the precursor) used therein play a crucial role in determining the properties of the resulting carbon film. Not only is there variability in the sp^2/sp^3/hydrogen bonding ratio, but the grain size and the scale of the ordering as well. Even within a broad category such as DLC or nanocrystalline diamond, there is significant differentiation based on the specific methods used, which only creates more of a need to quantifiably understand behavior in order to tweak these parameters.
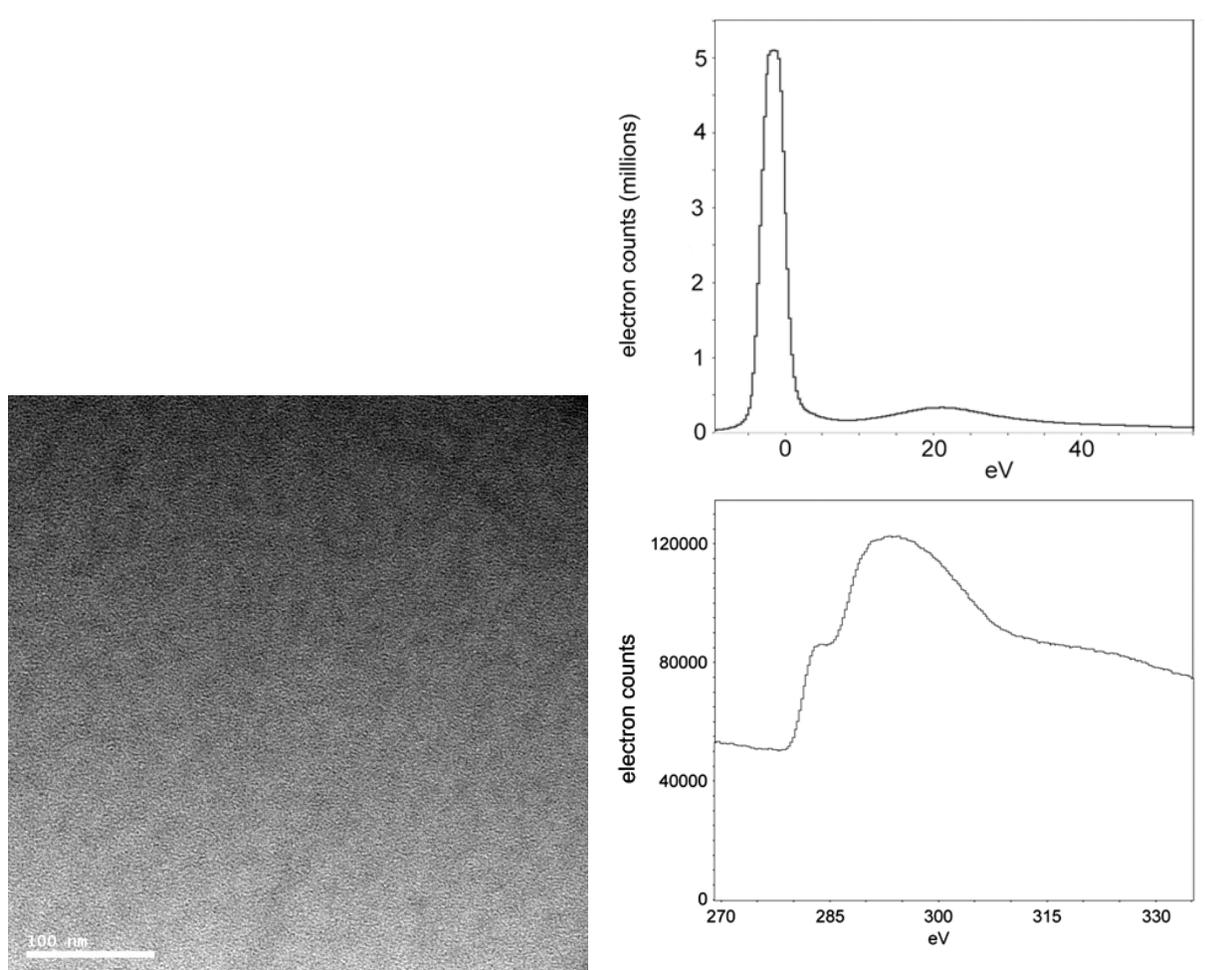
Figure 4.1. Left: DLC film bright field electron micrograph from a pristine region of the sample. Right: Zero-loss and carbon K-edge EELS spectra from the same area.

4.2.2 *In Situ* Sliding Procedure

The sliding experiment was performed by manually approaching the sample until contact was made, and then rastering the tip back and forth using the piezoelectric tube. Given the approximate 800-900 nm range of the motion, and a cycle speed of one per second, the sliding speed was estimated to be 2 μm/s. Before and after the experiment, nanodiffraction patterns were recorded to look for significant structural changes during the experiment. These diffraction patterns sampled a cylindrical volume approximately 800 nm in diameter around the sliding

region. For completeness, it is worth noting that due to well known projection issues with amorphous or highly disordered materials it is unwise to over-interpret minor changes in image or diffraction pattern details, only major ones (e.g. the formation of crystals > 2 nm) are detectable.

For all sliding experiments, the maximum contact pressure was estimated using a Hertzian contact model in order to provide a context for comparison with other experiments such as AFM. It is also important to have an idea of the normal load because of the different deformation mechanisms which can activate at different loads and the general importance to friction and wear behavior. [79] Because no actual forces are measured in the experiment, I consider this an upper bound estimation based on the literature values for the Young's modulus E and Poisson's ratio v for similar DLC films as well as tungsten. [80-83] According to Hertzian theory for a spherical tip impacting a flat surface,

(4.1)
$$\frac{1}{E'} = \frac{1 - v_{DLC}^2}{E_{DLC}} + \frac{1 - v_W^2}{E_W}$$

(4.2)
$$F_N = \frac{4E'a^3}{3R}$$

(4.3)
$$p_{max} = \frac{1}{\pi} \sqrt[3]{\frac{6F_N E'^2}{R^2}}$$

Equation (4.1) is a determination of the equivalent modulus of the contact, and (4.2) is a calculation of the normal load F_N as a function of contact radius a and tip radius of curvature R. The maximum contact pressure p_{max} can be calculated from Equation (4.3). This analysis when

measuring a contact radius of ~2 nm leads to a contact pressure estimate of 5 GPa for tips with radii of 50 nm. However in order to measure the necessary contact areas and tip deformation, much stronger contact than normal had to be made. In addition, I used a Young's modulus of 340 GPa for the DLC film, which is generously high. Therefore I estimate that the actual contact pressures during the experiment are likely less than 1 GPa. For completeness, note that while adhesion will add to the normal load – something taken into account by more comprehensive contact mechanics models [84] - the effect is small, on the order of 10^{-2} GPa [85], and for hydrogen-passivated surfaces much less. [86] I therefore neglected this effect when estimating the forces at the contact.

4.2.3 EELS Acquisition Procedure

Periodically between sliding passes, the screen was lifted to capture an EELS spectrum, as shown in Figure 4.2. By measuring the background-subtracted integrated counts at the carbon K-edge from 1s→σ* and 1s→π* transitions, the ratio of sp^2 to sp^3 bonding electrons can be determined. [63]
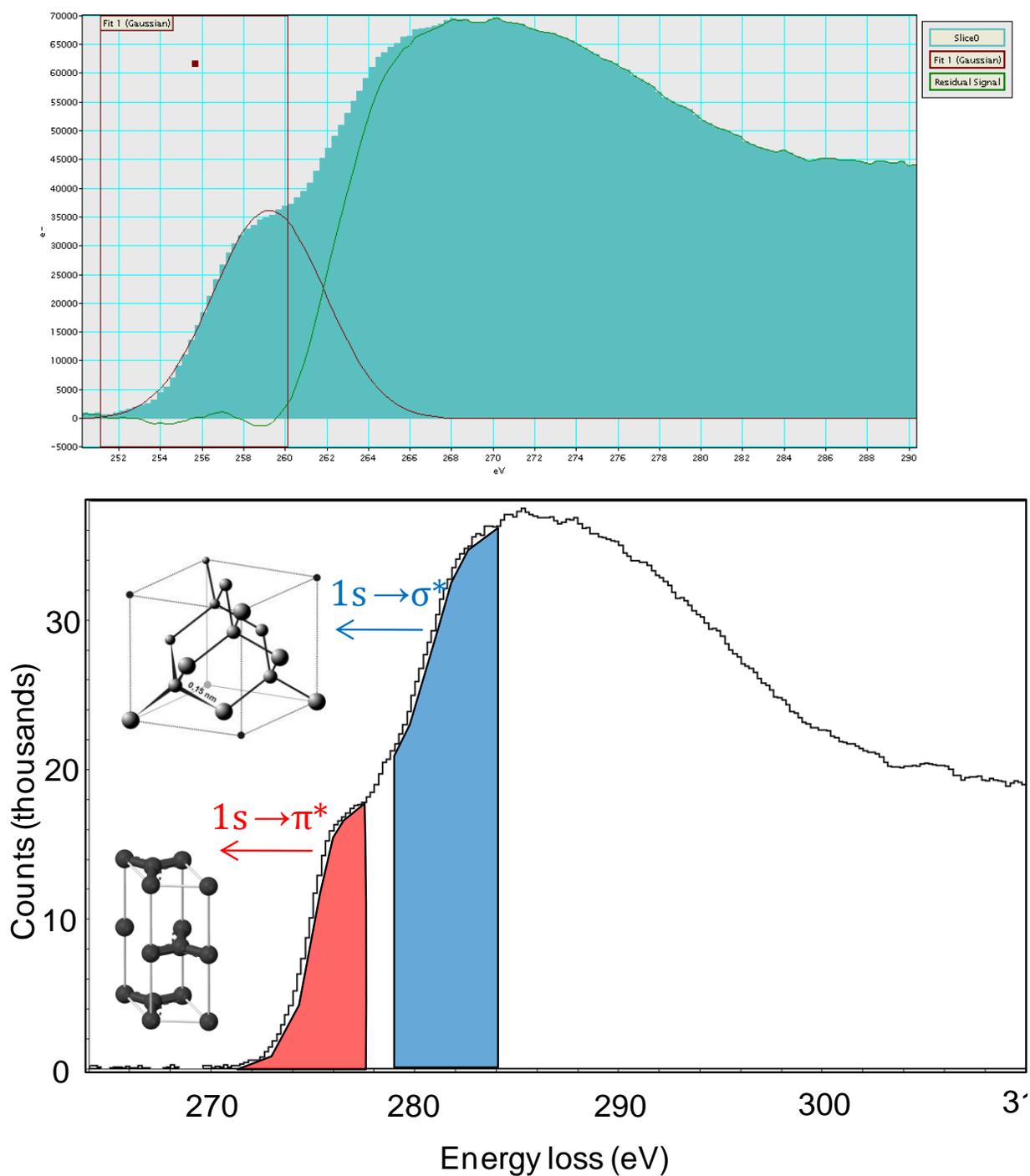
Figure 4.2. Top: Experimental EELS spectrum showing Gaussian fitting in order to calculate sp^2 and sp^3 signals. Small amounts of energy shift tend to occur over time, and are taken into account during the analysis of sequential spectra.The energy loss is also calibrated before each sliding test. Bottom: Experimental EELS spectrum showing how count integration is done and different electron transitions correlated with sp^2 or sp^3 carbon bonding.

In practice, however, the EELS measurement is often dependent on the electron dose [64] and can also depend upon other instrumental parameters such as collection angle, variations in the beam intensity during a long experiment and spectrometer resolution. Therefore some care is needed to be quantitative. I measured the dose rate for each GIF entrance aperture and magnification: the dose rate R (e$^-$/Å^{2}s) is given by:

$$R = \frac{B \cdot M^2}{K \cdot A}$$

Where K is the electronic charge, B the beam current in amperes, A the collection area on the screen, and M the magnification. The beam current (C/s) itself was measured using the microscope's displayed screen current. [87] The electron counts are then normalized to the lowest dose (i.e. 3 mm GIF entrance aperture) to reflect the fact that high-dose measurements result in sp^2/sp^3 ratios that are higher than they should be.

Dose (C/m^{2}s)	26,000 x	38,000 x	63,000 x
3 mm aperture	2590	1290	2161
0.6 mm aperture	13381	11583	6146

Table 4.1. Electron dose rate in the TEM as a function of magnification and GIF entrance aperture. Lower dose rates are associated with wider GIF entrance apertures (which require lower beam intensity to achieve a good signal-to-noise ratio).

In addition, we measured a "baseline" of EELS spectra as a function of time on an adjacent region of the sample, without any sliding taking place. We can subtract this from the sliding results to compensate for the effect of electron irradiation on the sample bonding. In this case we see a decrease in the ratio of sp^2 to sp^3 bonding with increasing exposure time, which could be

explained by hydrogen migration (probably caused by broken C-H bonds) or carbon polymerization. [88]

The true sp^2/sp^3 bonding ratio cannot be directly measured using this method; to do so requires modeling and calibration with pure graphite samples. However, we can safely measure the proportional changes of the sp^2 and sp^3 signal, because of the proportionality of EELS counts to bonding electrons in the sample. [64] Using the percentage change per minute of sp^2 and sp^3 bonds and subtracting the baseline rate yields the change in adjusted sp^2/sp^3 counts ratio as a function of time.

Finally, the results can be expressed as a number of monolayers representing the total volume transformed. The film density can be estimated from literature to be 1.6 ± 0.4 g/cm^3 [78, 89] which yields an estimate of 96 ± 24 carbon atoms per nanometer assuming hydrogen's contribution to mass is negligible. Using micrographs the sampled area can be obtained (typically a circle with radius 400 nm) and multiplied by the calculated thickness to get the total sampled volume. The sp^2/sp^3 ratio at each data point then translates into a specific number of bonding electrons transformed when compared to a pre-sliding measurement and normalized. This can be represented volumetrically as a number of equivalent monolayers of film transformed.

Looking at rates of change of the $1s \rightarrow \pi^*$ edge avoids issues with dose and aperture effects, as well as those arising from convolution with C-C bonding, C-H bonding, etc. I take the normalized, background-subtracted signal and integrate the counts and quantifiably report the relative differences in these values over the course of an experiment. Gaussian fitting is also used

to examine features like the full width at half maximum. Looking only at rates of change removes the need to perform the complex task of calibration and absolute quantification of the EELS data.

4.2.4 Transmission Electron Diffraction

Diffraction techniques were used in conjunction with typical bright field microscopy to investigate any long range ordering in the sample. As deposited, an amorphous diffraction pattern is expected, however diffraction patterns were taken at regular intervals to measure any periodicity developed in the film over the course of the experiment.

4.3 Results

Although the variable dose prevented a good absolute measurement of the sp^2/sp^3 bonding ratio in the film, the change over time was consistently positive during sliding and consistently negative for the electron beam baseline condition as shown in Figure 4.3. The total counts were seen to increase and decrease over the course of the experiment, which is attributed to sample drift, the changing amount of contaminants on the surface, and in general a changing sample volume.
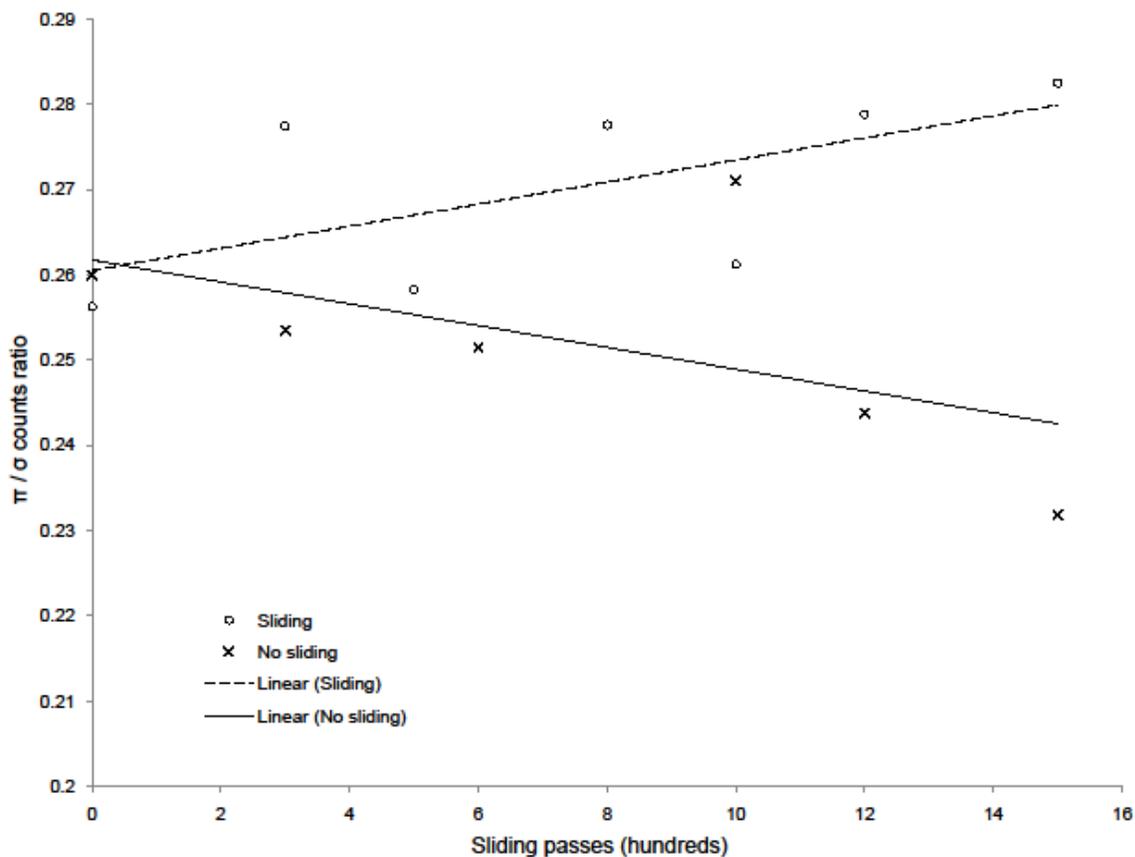
Figure 4.3. Baseline performance of an untested film (29.5 nm thickness) under the electron beam. Columns show sp^2 and sp^3 counts respectively, and points represent the sp^2/sp^3 count ratio. The sp^2 counts decreased by a linear average of 1.47% per minute, while the sp^3 counts decreased by an average of 1.1% per minute. This corresponds to the overall downward trend in sp^2/sp^3 ratio.

While the exact sp^3 to sp^2 conversion rates varied from sample to sample and even among entrance aperture sizes, the measurements in Figure 4.4 show a consistent increasing trend in the sp^2 to sp^3 bonding ratio, with the adjusted sp^2 counts increasing approximately 1% more per minute than the adjusted sp^3 counts over the course of the experiment. For the first series shown, the sample thickness was approximately 35 nm. The GIF entrance aperture was 3 mm. The adjusted sp^2 counts increased on average by 3.04% every 50 passes, while the sp^3 counts increased on average by 2.5%. For series 2 and 3, sample thickness was approximately 32.5 nm, with entrance aperture 2 mm. Every 50 passes, sp^2 counts increased 2.11% and 5.54%, while sp^3

counts increased 1.03% and 4.8% respectively. This held for each sample tested, regardless of

the increase or decrease in the overall number of counts.
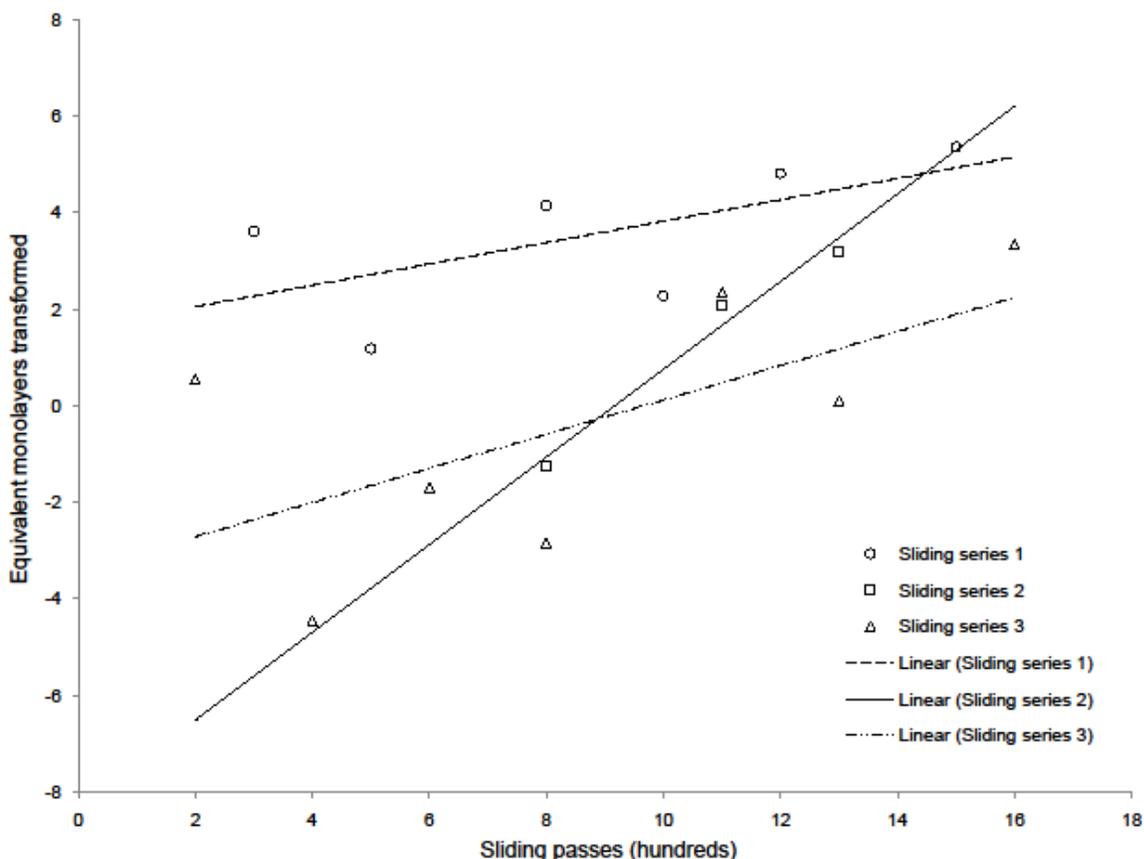
Figure 4.4. Trendlines of equivalent monolayers transformed for three sliding series. The data points show the equivalent number of monolayers transformed from sp^3 to sp^2 bonding. Negative values represent a transformation in the opposite direction, something which is attributed to drift and other factors near the beginning of the sliding experiment. A trendline is shown for the data points measured relative to the initial condition.

Similar behavior was seen at all the tested areas. Averaging the equivalent monolayers

transformed data to a linear trend, the rate of sp^3 to sp^2 transformation is between 0.009% and

0.018% of the total sampled volume per pass. Extrapolating these rates under constant conditions

would correspond to transformations of 13.5% to 27% after approximately 1500 sliding passes at

a given sample volume. The variability that sample drift confers on the results must be taken into

account, but otherwise I expect the same systematic error bars of 10% for these rate of change measurements as is used for the EELS quantification.

4.4 Discussion

We can see from the nanodiffraction patterns shown in Figure 4.5, as well as the full width at half maximum of the EELS spectra, that from the beginning to the end of the experiment, there was no significant long range ordering in the sampled volume – which would have been evident in a diffraction spot, sharper rings in the diffraction pattern, and possibly a narrowing of the carbon $1s \rightarrow \pi^*$ edge. This indicates that delocalized amorphous regions of sp^2 bonding are forming, as opposed to large regions of crystalline graphite. Since graphite is thermodynamically more stable than amorphous carbon or diamond, any stimulus (mechanical, thermal, etc) will move the system to the lower free-energy state, hence increased sp^2 content is to be expected.

The linear rate of transformation through the end of the experiment suggests that sliding has not created sp^2 bonds solely on the surface. The thickness of a hypothetical sp^2 surface layer can be calculated by looking at the equivalent monolayers transformed, and for the second series this was over 12 Å. If the changes in the bonding were limited to the immediate surface, a decreasing rate of transformation would be expected due to saturation, which is not observed.

This clears up some of the mystery of so-called graphitization effects. At small scales and relatively low loads, ordered graphite does not form, and we can expect the film behavior to become less diamond-like, moving towards the sp^2 corner of the phase map. The consequences of this include changing film hardness, modulus, and other properties. [90, 91] However, it is expected that with more extensive formation of sp^2 bonding due to more severe deformation,

crystalline graphite would form, consistent with other reports. [15, 17, 52-54] In this case, graphitic mechanisms could come into play, adding new layers of complication.
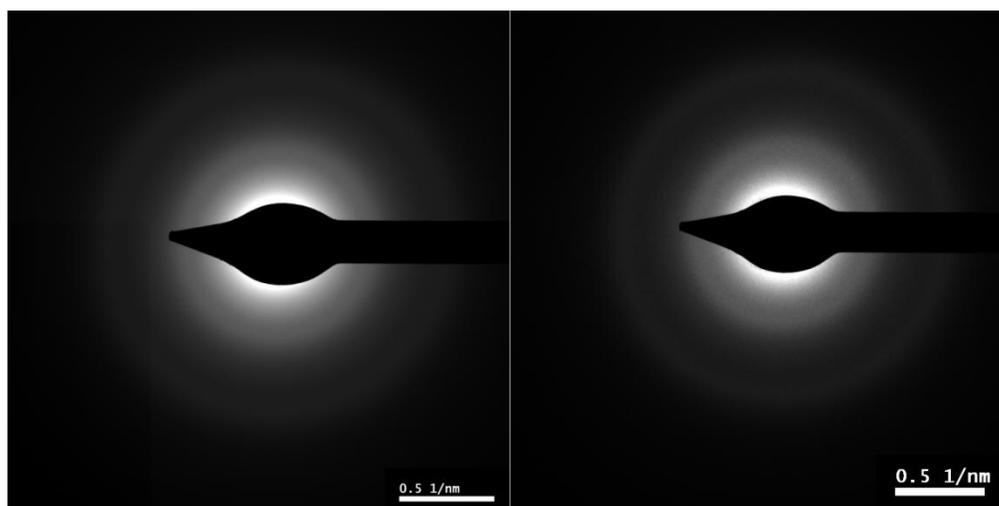
Figure 4.5: Nanodiffraction patterns of the same region of film before (left) and after (right) a sliding experiment. The approximate sample area is 800 nm in diameter.

The immediate linear trend of the transformation rate also has implications for the possibility of hydrogen migration contributing to the sp^3-sp^2 transformation. Preliminary results on "NFC6" DLC films [15], which contain a much thicker dead zone on the top surface, show a nonlinear rate of transformation, initially slow but sharply increasing after a certain time. The dead zone refers to the near surface layer of the film where the hydrogen is incorporated chemically in e.g. CH_3 configurations, as opposed to deeper layers where displaced hydrogen may exist in H_2 or radical form, outside the amorphous structure. [92] The N3FC films tested in this study have a much smaller dead zone, perhaps providing a constant migration of free and active hydrogen at the surface from the very beginning of the experiment.

In summary, under the conditions of the experiment herein, disordered sp^2 bonding is formed in response to the mechanical stimulus of a sliding tip, the rate being linear with the number of

sliding passes. This is consistent with my hypothesis, as well as the literature's observation of graphitization phenomena. It is important to have quantifiable data points at this particular scale and stress condition in order to build up a full picture of DLC's tribological behavior.

Chapter 5

Sliding Induced Tribochemical Wear of DLC in Gas Environments

5.1 Interdependence of Mechanical and Chemical Phenomena

In the previous chapter I discussed how tribology is responsible for both structural and chemical changes during a sliding contact. However, these processes do not occur independently of each other. The carbon bonding changes I observed in vacuum were dispersed throughout the film volume, suggesting the influence of relatively delocalized film stress. Here, however, I will focus on a much more localized connection between the mechanical action of the probe tip and chemical reactions on the surface. This tribochemical link is found to play a significant role in the nanoscale wear of these diamond-like carbon films.

5.1.1 Influence of the Testing Environment

The sensitivity of DLC's sliding behavior to its gas environment has been well-studied in the literature. [18, 25-27, 37, 41, 45, 49, 50, 55, 93-100] In general, these *ex situ* experiments measure macroscale qualities such as the friction coefficient and amount of wear after the tests. However, indirect measurements such as these cannot shed any definitive light on the nature of the underlying mechanisms. Specifically, they may be complicated by the involvement of multiple processes, and they result in often conflicting theories as to the role of various gaseous species that may be present in the test environment. In the previous chapter I performed the experiments in vacuum, but it makes sense to take the further step of examining the effect of

different gas environments. Similarly to the previous experiments, I aim to use the same sliding experiment with structural and chemical measurements to obtain a comprehensive and direct look at the film behavior during the tests. The combination and correlation of different kinds of measurements of the same phenomena allow us to make stronger conclusions and fill in the gaps between already existing theories.

It has been widely observed that the testing environment may affect the behavior of DLC films in a number of ways. The formation of transfer layers often contributes to lowered friction coefficients by acting as a solid lubricant layer. Studies show that these tribolayers are affected by the presence of oxygen, hydrogen, and water vapor in the environment, with mixed results on tribological performance. For instance, some studies attribute low friction coefficients to wear-induced graphitization of the tribolayer. In these cases, a reduction in wear due to a lubricating environment may actually increase friction. In other situations, passivating effects from gaseous species have been seen to reduce friction. Hydrogenated DLC as deposited has very few dangling bonds at the surface, which leads to its chemical inertness. During sliding, some passivating bonds are broken, and the availability of re-passivating species in the environment can result in more long-lasting low friction regimes. [27, 41, 95, 97, 98]

5.1.2 Tribochemical Wear

The specific nature of chemical reactions during sliding, what is called tribochemistry, is not well-developed at the nanoscale. Whereas in Chapter 4 I looked at chemical bonding states within a DLC film, here actual chemical reactions between the film and its environment are considered. Due to the amorphous, metastable nature of DLC, it should be expected to have a

fairly high potential for chemical activity, and this is likely responsible in part for the variability in its performance in different environments.

While numerous phenomena can affect the tribological behavior of DLC films, wear is of particular interest because it permanently changes the film surface. DLC is known for its resistance to mechanical wear due to the hardness and high modulus of the diamond-like structure, but wear can also occur via chemical processes – chemical reactions can form volatile products, removing material from the film. Tribochemical wear occurs when these processes are assisted or catalyzed by mechanical activity.

One example of the interdependence of multiple processes is tribo-oxidation. Metallic surfaces in many cases form oxide layers when exposed to atmosphere, but oxide layers several times thicker have been observed to form as a result of sliding contact. The oxidation is seen to vary as a result of sliding speed and normal load, but it is surmised to actually be a function of the size of a subsurface plastic zone. This plastic zone will dissipate heat from friction at the sliding contact at a different rate than unstrained regions, leading in turn to different rates of oxidation. [96, 101, 102] In this case, the interplay of several processes, acting at different rates, determines the end result (which itself may have positive or negative consequences for the tribology of the system depending on the metals and the relative hardness of the oxide layers). Again, this highlights the advantages of *in situ* techniques for studying such dynamic interactions in a controlled way. Regardless of method, the cooperation of mechanical and chemical processes is an important factor in real-world performance, and it therefore behooves us to consider both simultaneously.

5.1.3 Bridging Molecular and Macro Scales

There has been a reasonable amount of experimental work on nanoscale tribochemical wear, primarily using AFM. [28, 103-106] Other work uses spectroscopy or other methods to determine the thermodynamical and chemical reactions that occur during sliding. [18, 21, 22, 29, 99, 107-110] These studies attempt to look at the fundamental chemistry of the interaction of gaseous and other third party molecules with the film: starting with the potential chemical activity, to the likelihood and rates of different chemical reactions, and the resulting impact on the film.

However, to date there is a gap in our understanding connecting monolayer level measurements to tribochemical wear at the nano and microscale and linking these to macroscopic results, something which is needed if tribological phenomena are to be comprehensively understood. My aim is to observe the sliding contact inside the TEM in order to build connections between these different paradigms of tribology and deformation. The increasing level of complexity at larger scales requires that experiments take more direct, easily interpretable measurements, a strength of the technique used here. I expect that making more definitive statements regarding the origins of DLC friction and wear behavior at this sort of microscale tribological contact will follow naturally from nanoscale ideas, explain macroscale observations, and shed light on the nature of tribochemical reactions in general.

These experiments were performed in both wet N_2 and H_2 gas, and the resulting micrographs, videos, and EELS spectra show the structural and chemical evolution of the surface structure as a function of time and sliding duration.

5.2 Experimental Details

Standard sized copper TEM grids with lacey carbon support were attached to a Nanofactory HS-100 STM-TEM sample holder by conductive epoxy to a gold wire. Transmission electron micrographs, videos, and electron energy loss spectra were obtained using an FEI Titan 80-300 ETEM at Brookhaven National Laboratory. Sliding experiments were performed at 300 kV under 0.15 torr N_2, 0.15 torr H_2, and 1.5 torr H_2 gas, as well as corresponding non-sliding time series to measure the effect of the electron beam alone. The probe tips were tungsten wire, electrochemically etched in NaOH with radius of curvature approximately 100 nm. The stroke length and tip velocity varied, but were on the order of 1 μm and 2 μm/s, respectively.

Estimations of the volume of worn material were done by assuming the measured intensity of the film is linearly proportional to its thickness. This is a good approximation for materials where diffraction is so weak that mass and thickness dominate the contrast. Because my samples were largely amorphous and homogenous, relating micrograph brightness to thickness is a valid approach.

Every wear track with significant enough area to be outlined in two dimensions was highlighted manually and the average intensity in that region compared to the average intensities in vacuum and a nearby unscratched area of the film to determine the volume of material removed: the surface area given by the outline and the depth given by where the average pixel brightness fell between the vacuum and unscratched film values. Essentially, knowing the thickness of the film from EELS, the vacuum and unscratched film values yield the slope of the

brightness-thickness linear relation, and from there the thickness of any given brightness value can be calculated.

Wear particles that remained on the sample were also highlighted using a brightness threshold, and the estimation of volume was made using the thickness contrast of the particles in linear relation to the film thickness determined by EELS. The sample area was kept constant by virtue of the delicate sliding motion which did not physically cause the sample to move, and by use of landmarks to ensure that the examined areas remained the same.

The ratio of sp^2 to sp^3 carbon bonding over the course of the experiment was measured by integrating normalized, background-subtracted EELS spectra. The proportional rate of change over the course of the experiment is measured to avoid inaccuracies with absolute measurement. The energy shifts of nitrogen and oxygen features were measured with respect to the carbon K-edge. Additionally, the spectra were fit using Gaussian functions to distinguish between energy-loss features at close to the same energy.

5.3 Results
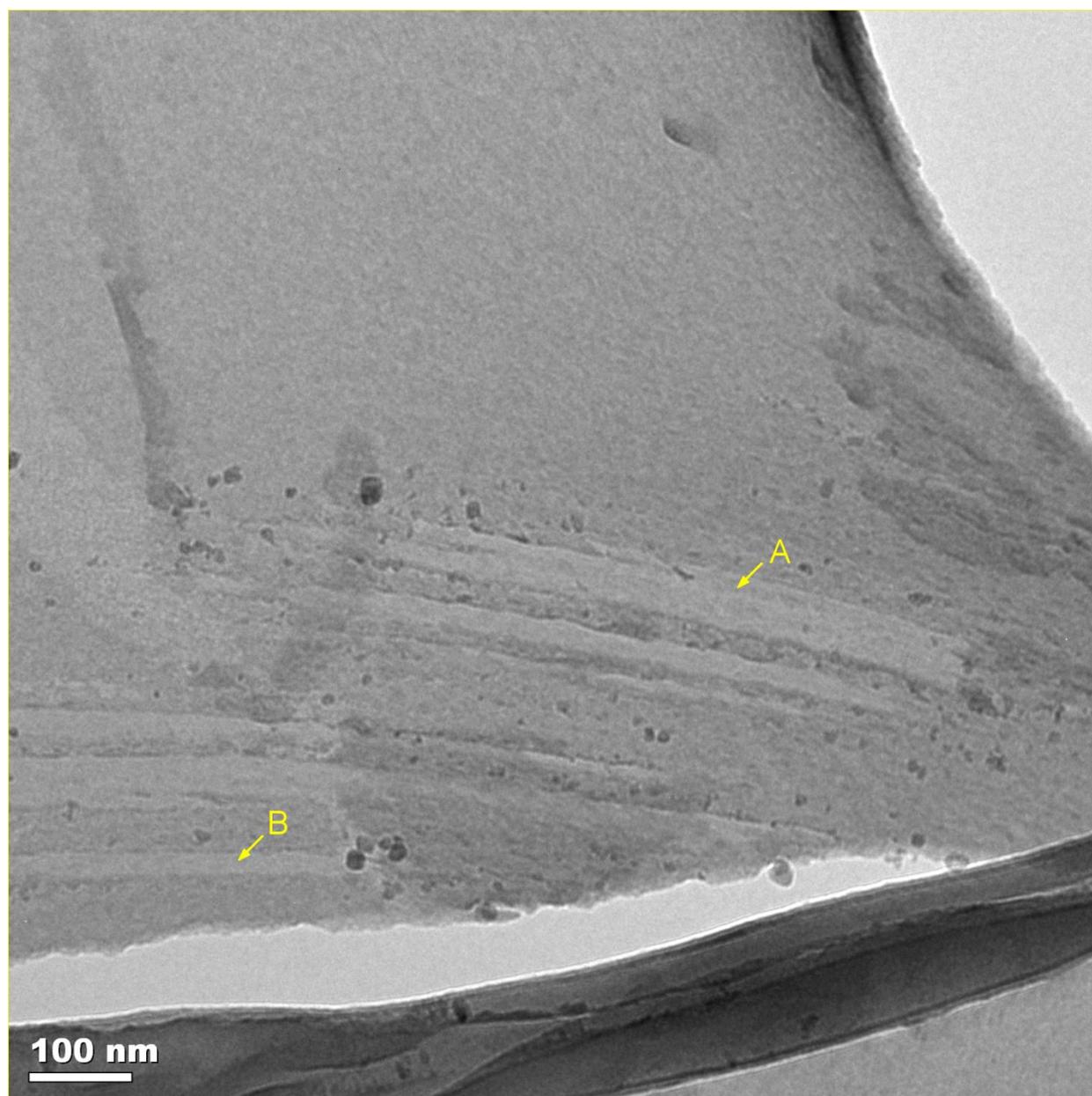
Figure 5.1. Energy filtered (zero-loss) TEM micrograph showing the surface of a 26 nm thick DLC film during a wet N_2 sliding experiment after 20 sliding passes. Arrows indicate lighter regions, which are interpreted as thinner due to the amorphous nature of the film. As A and B have different background brightness levels, separate calculations were done in each part of the micrograph in order to determine the estimated volume lost.

The results in wet N_2 show classic wear behavior as shown in Figure 5.1, an energy-filtered micrograph of the film mid-experiment. An energy-filtered video of the sliding test is provided (Video V1), where the lighter regions are interpreted as thinner regions where material has worn away. Even though this is taking place at the nanoscale, the reduction in the total thickness indicated by the brighter regions is very similar to what one observes for wear tracks at the macroscopic scale; one could increase the scale bar by a factor of 1000-10,000 in which case the results would look similar to typical scanning electron micrographs of wear tracks.

The wear volume calculation was carried out on the 0.15 torr N_2 sliding series, and the results are shown in Table 5.1 and Figure 5.2.

All values in nm^3	Wear track volume	Wear particle volume	Net tribochemical volume lost	Wear rate per sliding pass
20 sliding passes	363,620	114,169	249,450	18,181
40 sliding passes	820,703	136,653	684,050	22,854
60 sliding passes	1,210,198	133,492	1,076,706	19,475
80 sliding passes	1,307,474	145,278	1,162,195	4,864
100 sliding passes	1,391,718	133,706	1,258,012	4,212

Table 5.1. Material lost to tribochemical wear over the course of a sliding experiment in 0.15 torr N_2 gas. Average measured brightness values (0-256) for this test were ~195 in vacuum regions, ~140 at full film thickness, and ~160 in wear tracks. Wear particles averaged ~120. The net tribochemical volume lost is a measure of material which is actually removed from the film as compared to wear particles. Each measurable wear track in the micrographs was individually selected, area and mean brightness measured, and summed to get the totals shown here.
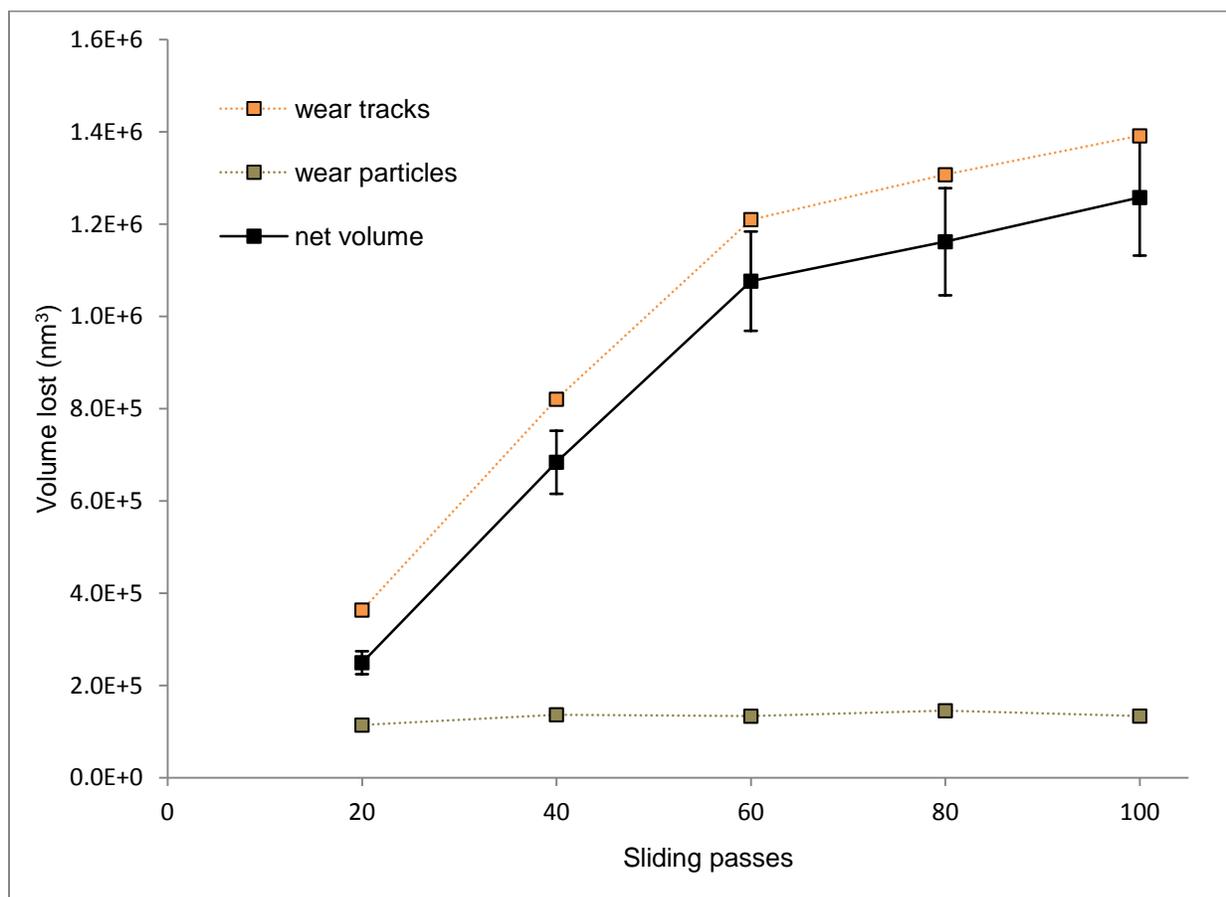
Figure 5.2. Estimated volume loss from the film in both the observed wear tracks and the wear particles. During sliding in wet N_2, the estimated volume of wear particles remains relatively constant, although the average particle size increases over the course of the experiment. The estimated volume of material removed from the wear tracks continues to increase until the film curls up at 120 sliding passes and measurement becomes too difficult. Because the delineation of the edges of wear tracks was done by hand, a human error of 20% is assigned conservatively based on the repeatability of measurements of the same micrograph.

Electron energy-loss data as shown in Figure 5.3 clearly shows a strong oxygen edge at ~525 eV which is unsurprising considering a known 10^{-5} torr water vapor impurity in the environmental system. The presence of chemisorbed oxygen species on the film surface implies their likely involvement in tribochemical wear. Consistent with this, there is little to no wear debris, an indication that the wear tracks are forming volatile species as would be expected if the tribochemical reactions taking place formed molecules such as carbon monoxide. During sliding

in wet N_2, the ratio of adsorbed oxygen to nitrogen is also seen to increase by 2-4 times over the course of the experiment: Figure 5.4 shows the changes in O/N ratio of normalized, background subtracted integrated counts.
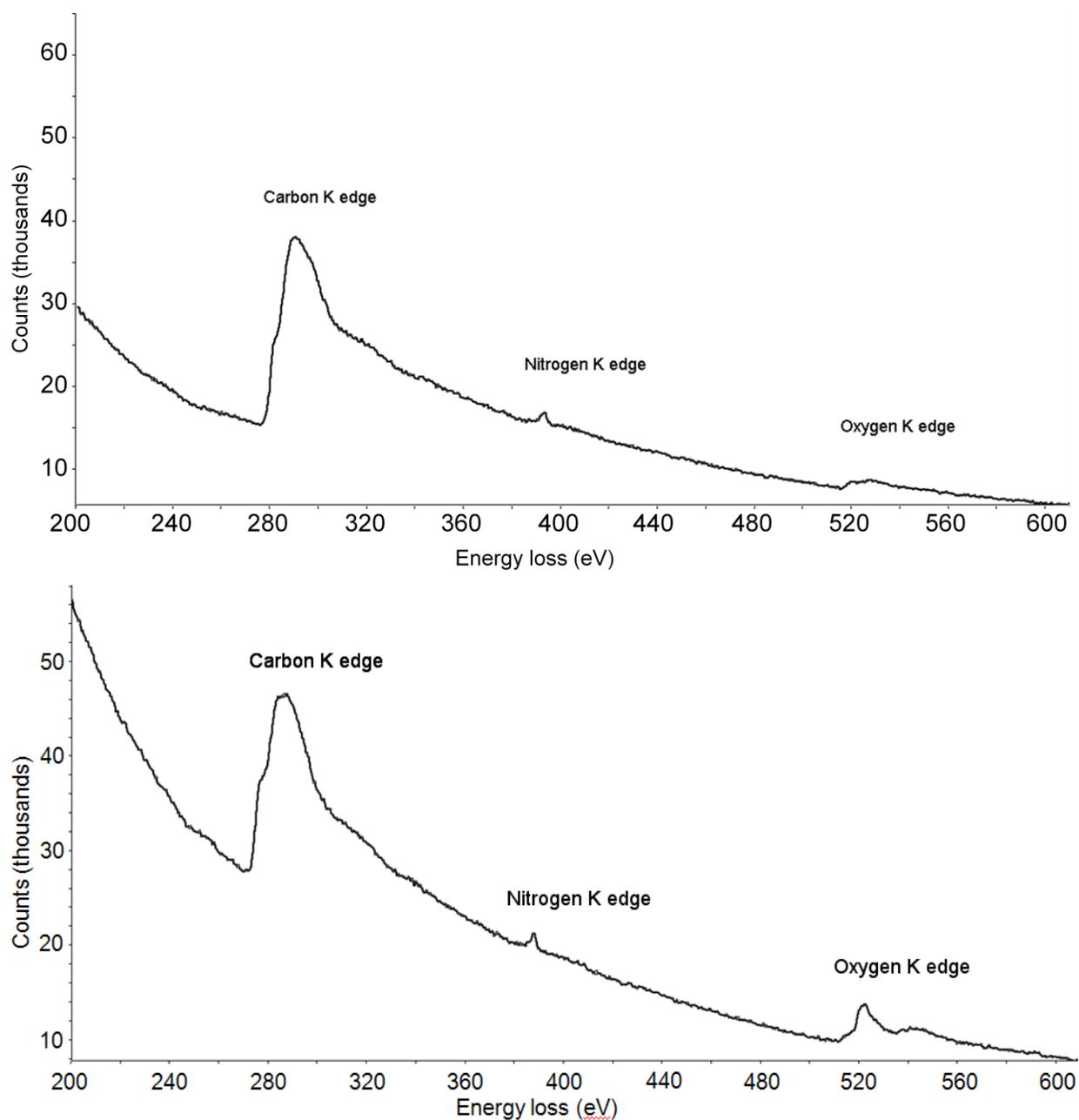
Figure 5.3. EELS spectrum after 0 (top) and 110 (bottom) sliding passes in wet N_2 showing the relative prevalence of chemisorbed oxygen to nitrogen. Quantification suggests a two- to four-fold increase in the relative amount of oxygen compared to nitrogen present in the sampled volume over the course of a sliding experiment.
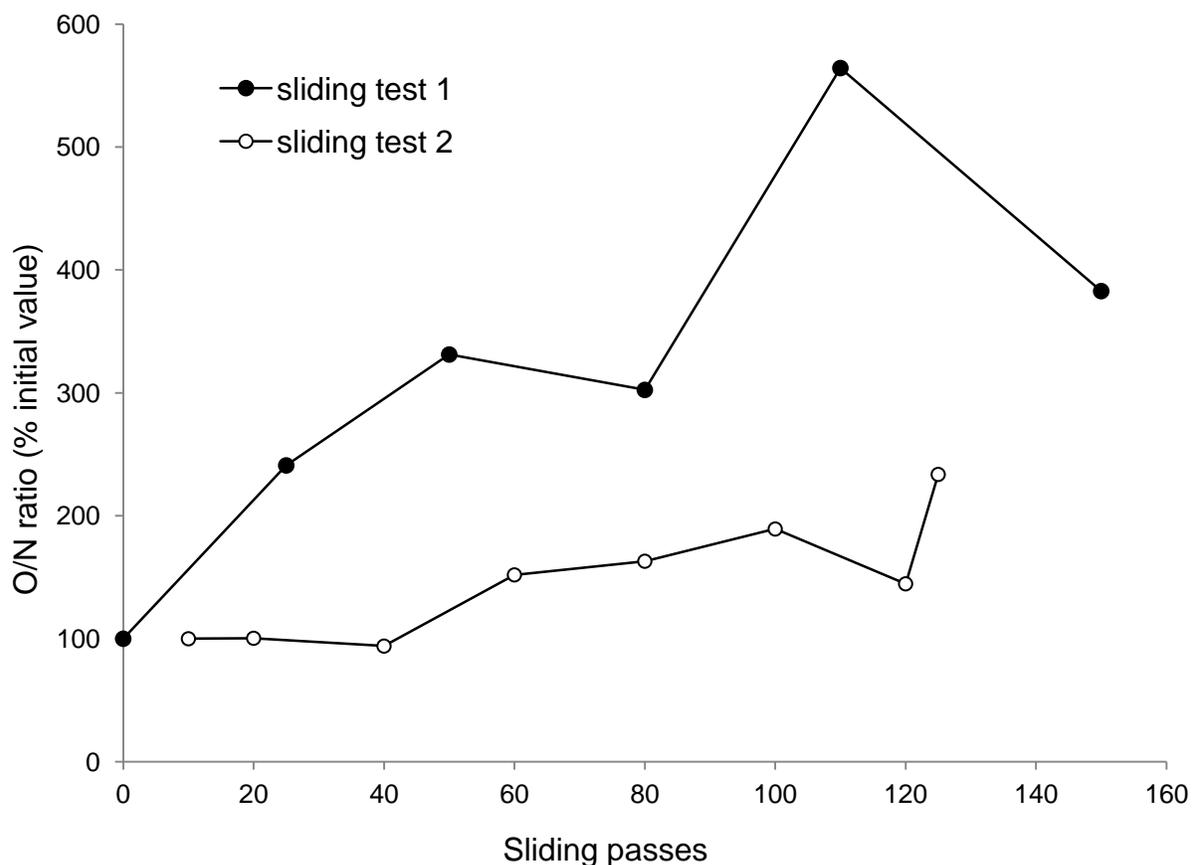
Figure 5.4. The ratio of oxygen to nitrogen edge counts is measured using EELS to increase over the course of the sliding experiments in wet N_2. The percentage increase of the ratio of the signal reflects the actual proportional change in bonding in the sampled area. The EELS counting process has negligible error, although there are systematic errors associated with sample drift, etc. The increasing O/N ratio suggests incorporation of oxygen into the solid phase during sliding.

These results can be compared to those in wet H_2 (see Figure 5.5 and Video V2) where there are no significant wear tracks. Despite the presence of chemisorbed oxygen, the amount of wear observed in these tests was too small to be measured. The results can also be compared with sliding in vacuum[58] where there are no significant wear scars or wear debris – see Figure 5.6. These earlier vacuum experiments with the same films, same method of contact, and same sliding procedure, result in little structural evidence of wear on the same scale as in N_2.
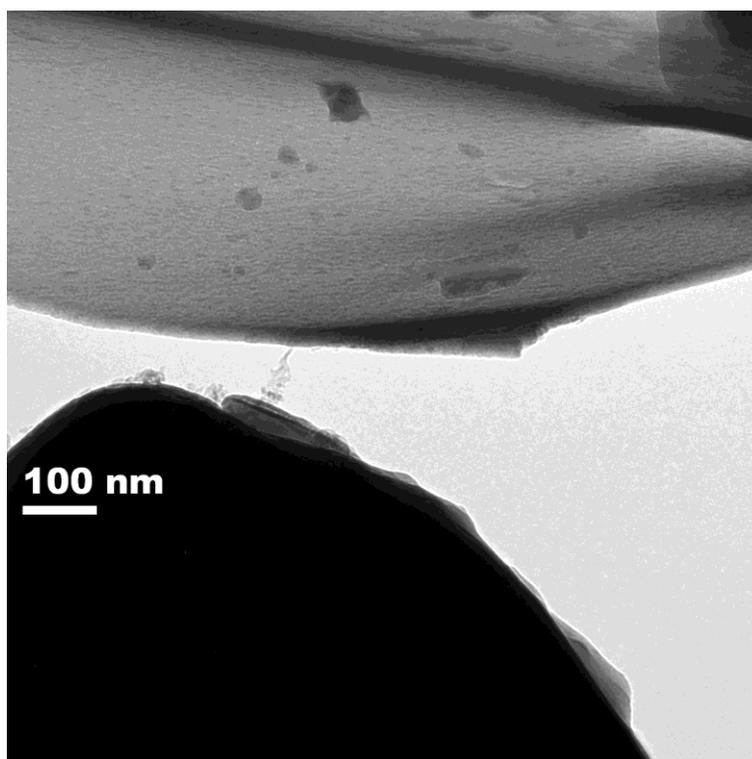
Figure 5.5. Bright field TEM micrograph at the conclusion of a wet H2 sliding experiment. No significant wear tracks are observed at the conclusion of the test, which used the same type of contact and sliding speed as previous tests. Some light markings and wear particles are visible at the end of the test, but not at the scale as N_2 experiments.
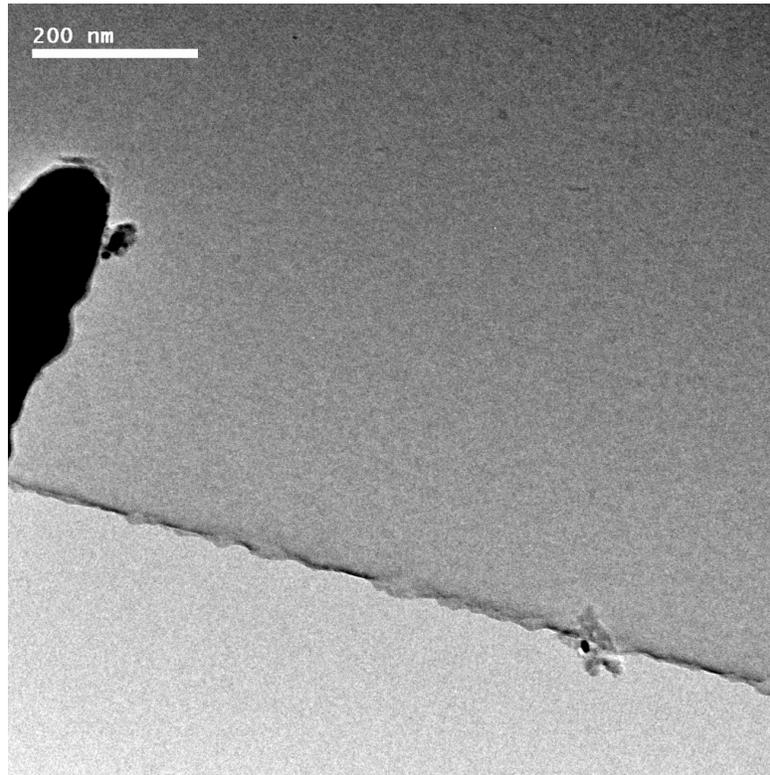
Figure 5.6. Bright field TEM micrograph of a DLC film after the conclusion of a sliding experiment in vacuum. No significant wear tracks are observed in these experiments.

Lastly, the rate of the carbon $sp^3 \rightarrow sp^2$ phase transition induced by sliding is measured and compared to previous work. [58] The rate is substantially increased in wet sliding tests as shown in Table 5.2. Figure 5.7 shows the effects of beam-induced damage, which can result in significant amounts of material removal over time. This damage was also seen to be dependent on the gas pressure with much faster damage observed in 1.5 torr experiments.

Experiment	Percentage change of carbon sp^2/sp^3 edge ratio	Number of sliding passes or minutes
Vacuum baseline	-10.8%	30 minutes
Vacuum sliding	+10.3%	1500 passes
0.15 torr wet H2 baseline	-8.2%	40 minutes
0.15 torr wet H2 sliding	+35.4%	125 passes
1.5 torr wet H2 baseline	-28.4%	12 minutes
1.5 torr wet H2 sliding	+66.8%	175 passes
0.15 torr wet N2 baseline	-2.7%	35 minutes
0.15 torr wet N2 sliding	+5.1%	150 passes

Table 5.2. Comparison of the percentage increase of the carbon sp^2/sp^3 edge ratio over the course of various sliding experiments. The ratio is determined by integrating the normalized, background subtracted signal at the beginning and end points of the experiments. Negative numbers therefore represent a relative decrease of sp^2 hybridized bonds compared to sp^3. My results confirm the acceleration of the $sp^3 \rightarrow sp^2$ transformation in a gas environment and also highlight a gas pressure dependence.
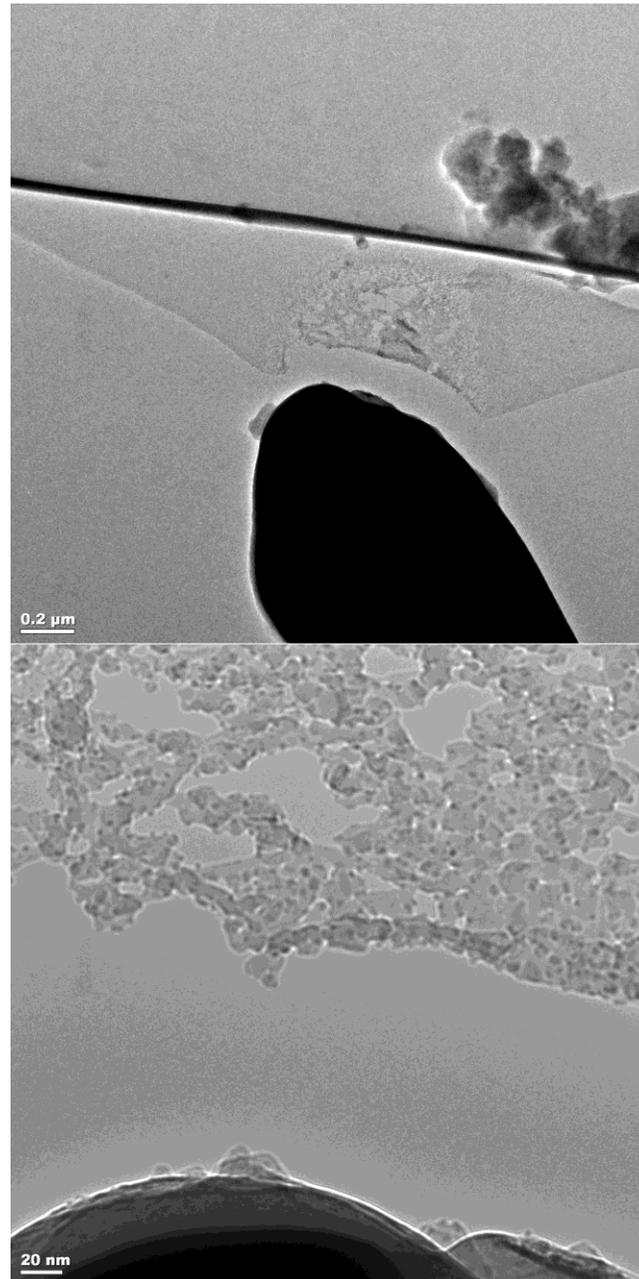
Figure 5.7. TEM micrographs showing DLC film damage after long term exposure under the electron beam. In higher gas pressures, the general etching of the films occurred faster.

For completeness, it should be noted that electrons can etch carbon in the presence of water vapor[111], probably involving electron-activation of the water-gas shift reaction ($H_2O + CO \leftrightarrow H_2 + CO_2$). [100, 112] While this was also taking place during observation, the rate of etching

was much slower than the wear directly due to sliding of the tip over the surface. Isolating this kind of simultaneous reaction is one reason extensive baseline measurements are taken. Finally, it is worth mentioning that at this scale the thermal contribution from the electron beam is minimal, and therefore the localized character of the wear suggests that thermal processes are not involved.
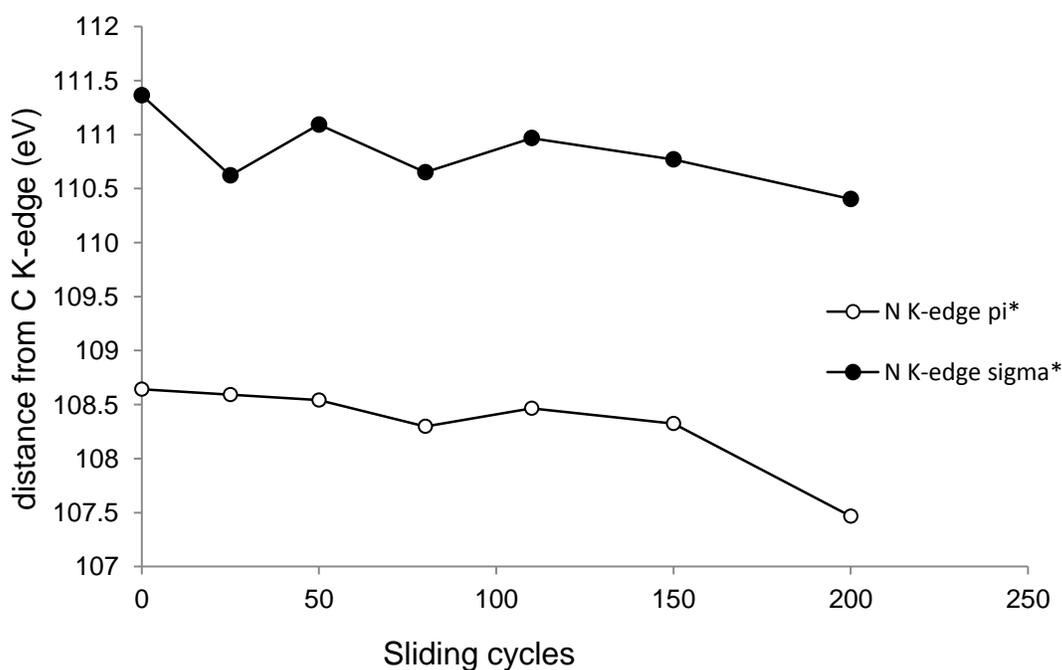
Figure 5.8. Nitrogen edge energy loss changes over the course of an experiment measured with EELS. This indicates a change in the behavior of adsorbed nitrogen electrons, and therefore the chemical activity of nitrogen species. The measurement is done in comparison to the carbon edge, whose features can be linked with specific energy losses. The near edge structure of the nitrogen K-edge also changed over the course of the experiment to indicate different bonding environments of the adsorbed nitrogen.

5.4 Discussion

We can look at these results from several perspectives, in line with the previous work on the subject. One obvious starting point is at the scale of chemical reactions, where reaction rates and

chemical activities are used to understand the molecular level film-atmosphere interactions. As noted previously, there are many such possible reactions that result in carbon atoms actually being removed from the film, ranging from carbon etching in the presence of water vapor to oxidative products (the simplest of which are CO and CO_2), carbon nitrogen compounds such as HCN, or aromatic compounds like pyridine (C_5H_5N) or pyrrole (C_4H_4NH). EELS spectra show clearly that oxygen and nitrogen become incorporated in the film during sliding, and even change their bonding energy as the experiment progresses. These changes are shown in Figures 5.4 and 5.8. This evidence points to their involvement in chemical reactions, though that cannot be measured directly using this method.

Considering the bond dissociation energy of the N-N bond (945 kJ/mol) when compared to O-H (460 kJ/mol) or H-H (436 kJ/mol)[113], the low quantity of chemisorbed nitrogen is not surprising. Still, some interactions are observed, meaning that there is likely a corrosive process occurring that is not as fast or significant as the observed oxidative processes. The measured increase of adsorbed oxygen compared to nitrogen in EELS further suggests that the oxidation processes are not limited to the film surface. That is, there are oxidative reactions that result in volatile compounds, but an increasing amount of oxygen compounds also become incorporated into the solid phase. [36, 58, 114, 115]

Another perspective to consider is a more macroscale observation of tribochemical wear. While this has been widely observed in the literature, these experiments reveal the high degree of spatial localization: micrographs like Figure 5.1 show that wear does not occur evenly on the surface but is quite limited to nanometer-scale areas where the probe tip has made contact.

While this is interesting, a combination of both viewpoints leads to a more comprehensive theory. The observation of wear tracks (evidence of chemical wear, not just mechanical as discussed above) where the tip passes indicates that sliding is the primary cause of chemically activated atoms in the film which then react with either gas-phase water or, more likely, chemisorbed oxygen or hydroxyl species in the immediate vicinity. Note that a sliding interface is intrinsically similar to a sliding fracture zone, and there is strong evidence that fracture can lead to highly activated species which are capable of emitting x-rays [116] or creating oxygen vacancies at the surface of strontium titanate. [117] In effect, after the trailing edge of the tip passes there will be carbon radicals present which will be very reactive to a variety of chemical processes.

The absence of wear tracks in wet H_2 experiments indicate that these highly active carbon radicals at the trailing edge of the tip are passivated in a nonvolatile manner, almost certainly due to chemisorption of hydrogen. Despite the presence of water vapor, the lower bond-dissociation energy of H_2 and the high activity of H^+ support the observed dominance of passivation over tribochemical wear reactions in these tests. [113]

Lastly, the measured increase of the sp^2/sp^3 ratio for carbon in a wet environment compared to dry also points to tribochemical causes, but here having a secondary effect. Even in an amorphous structure, the more thermodynamically stable in-plane sp^2 bonding would be expected to react slower with oxygen/hydroxides than sp^3-hybridized carbon or radicals which may be present immediately after sliding. As a result, all other things being equal, any gaseous species would preferentially react with a dangling sp^3 bond, increasing the proportion of sp^2 bonds remaining in the film.

What should be apparent is that the results are surprisingly similar to what one would expect for mesoscale experiments, with much higher tribochemical wear in the presence of water and clearly indicate that tribochemical processes are only taking place in the immediate vicinity of a sliding interface. It has been known that this sort of tribo-corrosion synergy plays a role at the macroscale, and that chemically this is quite reasonable at the atomic scale. What is shown here is that there is little difference between the processes taking place across many length scales, beyond the obvious effects due to multiple asperity contacts at the mesoscale and different rate terms that are predictable based upon differences in contact areas. Tribochemical reactions in general, including wear, will likely show little nanoscale variation, with the obvious exception of possible secondary effects associated with the enhanced reactivity of nanoparticles which is well known in heterogeneous catalysis.

Chapter 6

Analytical Friction Model Using Dislocation Mediated Deformation

6.1 Shear and Plowing Friction

The aim of this chapter is to reconcile the ideas of tribology and materials science to create a

model for friction that incorporates analytical dislocation theory. Building on previous work in

this area, I show that the deformation of a material due to dislocation motion by creep is a viable

way of modeling the plowing wear of a material in contact with a single asperity.

As discussed in Chapter 3, we have seen that using dislocation theory to understand tribology

is not only possible, but a fruitful approach. It is helpful to step back though, and look at

tribology as, broadly speaking, the result of deformation mechanisms – particularly plastic,

irreversible deformation that dissipates energy. It is possible to describe the behavior of a

stressed material using deformation modes rather than individual dislocation stresses. In order to

connect these two ideas, it is important to think about how dislocations participate in

deformation.

One of the earliest attempts to account for the effects of deformation on friction was made by

Bowden and Tabor in 1942 [118], and hereafter abbreviated as the BT model. By considering the

contact mechanics of an asperity sliding across a flat surface, they realized that not only should

there be a shearing component of friction at the interface, but the plowing of material in front of

the tip should contribute as well. The sum of these two retarding forces was taken to be the effective frictional force experienced by the asperity.

The model is quite simple conceptually, and is described more fully below. The only parameters are the contact area, shear strength, and flow pressure. As a result, the BT model has been widely used as a starting point for determining the components of friction. Efforts to introduce material property dependencies such as the Young's modulus into the BT model include work by e.g. Bull [119], Malzbender and de With [120], and Komvopoulous. [121] In these cases, the modeling is used to predict or explain the measured friction coefficient or wear performance. The relevant terms in these models are the resistance of the material to plowing (flow pressure) and the resistance of the material to shear stress (shear strength).

However, both of these variables are empirical in nature, as they are derived experimentally and depend on many factors. In an actual experiment, flow pressure may be thought of as a kind of hardness representing the resistance to plastic deformation, and the shear strength as the average resistance to a number of shearing stresses in the near surface region. It would be difficult and usually inappropriate to use theoretical values in every scenario. Furthermore, measuring these values during an experiment designed to measure tribological quantities often involves assumptions and estimations. This can result in difficulty when attempting to reproduce or compare results.

Attempts have also been made to extend the BT model to take into account additional forms of material deformation, such as asperity creep, asperity deformation in general, etc. These extensions can range from rock friction to aerospace applications. [122-125] This kind of

approach has been useful for making sense of more and more complex data sets, but fundamentally it still relies on the experimental measurements to determine the friction force. Additionally, these empirical models present a challenge to understanding the details of a sliding interface at a more fundamental level.

The focus of this chapter is to develop a formulation of the BT model in terms of the underlying materials science of plastic deformation. Instead of extending the BT model, I aim to limit the dependence on empirical terms with an analytical formulation. In particular, I equate the shear strength to the retardation of dislocations at the sliding interface, and consider the plowing in front of a rigid asperity as a creep process. I will still need to consider variables such as the material hardness, but it will be incorporated into a larger structure. I will focus on copper as a model system, but the results are extendable to other materials. The aim of the model is not to exhaustively take into account all mechanisms of friction, but to use dislocation theory to approximate the frictional force of a crystalline material at steady state without needing empirical parameters, and using the substantial existing knowledge on asperity contact mechanics. Due to the non-specific analytical nature, the model can then be checked against a wide range of experimental and other results.

6.2 Model Framework

I will first develop the model by equating the two components of the BT approach to retardation of dislocation motion at the interface, and creep. As an overview, the assumptions and inputs necessary are listed here, and a schematic is shown in Figure 6.1.

1.   The grain size is taken to be 0.1 mm. This is important for diffusional creep and for limiting the length of dislocations.

2.   The dislocation density (as calculated using a misfit angle of 10°).

3.   Material flow around the asperity tip is horizontal.

4.   The reference length for measuring strain is taken to be 100 times the Burgers vector.

5.   The hardness used for calculating the contact area is taken from literature values.

6.   Various material constants are used, and shown in Table 6.1.

7.   The primary variables used in the model are temperature, normal load, sliding velocity, and asperity size (radius of curvature or cone angle).

   a.   Asperity size and shape will influence the relative strength of plowing vs. shear friction. I consider spheres, cones, and square pyramids here with size as a variable (size meaning radius of curvature for spheres and tip angle otherwise).

   b.   The temperature is taken to be in the appropriate regime for power law creep (see Figure 6.2).

```
┌─────────────────────┐      ┌─────────────────────┐      ┌─────────────────────┐
│ Shear strain rate   │      │ Solve the strain    │      │ The force needed to │
│ while in the creep  │─────→│ rate equation for   │─────→│ push aside material │
│ regime.             │      │ the shear stress    │      │ by creep is         │
└─────────────────────┘      │ experienced by the  │      │ essentially a drag  │
                             │ asperity.           │      │ force on the        │
                             └─────────────────────┘      │ asperity, which is  │
                                                          │ effectively the     │
          ┌─────────────────────┐   ┌──────────────┐     │ plowing friction    │
          │ Relate the velocity │   │ Asperity     │     │ force Fᴄ            │
          │ of the asperity     │   │ cross-       │     └─────────────────────┘
          │ with the shear      │   │ sectional    │
          │ strain rate of the  │   │ area         │        ┌──────────────┐
          │ plowed material     │   └──────────────┘        │ Drag force   │
          │ geometrically.      │                           │ due to shear │
          └─────────────────────┘                           │ developed    │
                                                             │ by Merkle,   │
                           ┌──────────────────┐              │ Fᴅ           │
                           │ Bowden & Tabor's │              └──────────────┘
                           │ model:           │
                           │ Shear + Plowing =│──────────────────────────→
                           │ Total friction   │
                           └──────────────────┘
       ┌─────────────────────┐              ┌──────────────────────┐
       │ The friction        │              │ Total friction force │
       │ coefficient μ is the│←─────────────│ F                    │
       │ net frictional force│              └──────────────────────┘
       │ divided by the      │
       │ normal load.        │
       └─────────────────────┘
```

Figure 6.1. Flowchart of the analytical friction model.

6.2.1 Interfacial Shear and Misfit Dislocations

The BT friction model is a simple summation of shear and plowing forces: $S + P = F$. The shear component of friction in this model essentially considers the normal contact area during sliding interacting with the shear strength of the material. As mentioned above, this term is complicated by the details of the experiment, but is conceptually analogous to the critical resolved shear stress: the threshold stress necessary for continued plastic deformation at any given moment. This shear term is described by the total contact area (as given by the Hertzian model [126] for a spherical asperity as πa^2 where a is the contact radius) multiplied by the shear strength of the softer material s, so $S = \pi a^2 s$.

It is known that in many materials, shear forces result in bulk deformations that are accommodated by dislocation motion. Furthermore, it is known that interfacial sliding also has to do with dislocation motion, and indeed the forces on the dislocations can be considered to be representative of the macroscale forces on the material. [74] Therefore if we are interested in a more theoretical framework to look at the tribology of shear friction, we should be able to use dislocation mechanics to grasp the behavior.

The problem of drag forces on dislocations in the bulk is well studied as a form of internal friction. That is, when bulk deformation occurs by dislocation motion, the forces that resist that motion dissipate some of the applied energy. Similar behavior is expected for the surface: in addition to stress or strain-induced dislocations, any two contacting surfaces with imperfect registry will form misfit dislocations at the interface, which also must move if sliding is to occur. [74] Therefore, I can consider the dissipative drag forces on interfacial dislocations as related to the tribological losses at the sliding contact.

The drag forces on dislocation motion through crystals can be generally grouped into either thermal or viscous effects. Thermal processes have to do with the mobility of dislocations through various potential barriers in the elastic field, and are generally relevant when the applied stresses are low. When stresses are high, so-called "overbarrier" motion results, and the drag force becomes viscous – proportional to velocity – as dislocations interact with phonons, electrons, and other excitations in the crystal. [127]

By using this interpretation the empirical shear term *S* can be redefined as a viscous

dislocation drag force F_D. Both terms effectively try to capture the interfacial resistance

generated by sliding one material over another.

One of the key results of Merkle's work [74] is the macroscale friction force (per unit length)

due to the dislocation drag: F_D. Here, the thermal and viscous dissipation mechanisms

experienced by a dislocation are combined into one equation. A net drag coefficient B_{tot}

comprises the viscous phenomena of electron and phonon wind as well as the thermal flutter

effect, while the contribution from radiation friction is incorporated via the hyperbolic cotangent

function:

$$(6.1) \qquad F_D = \frac{N_d(\sigma_p b)(\sin\varepsilon + \cos\varepsilon)}{2} \coth\left[\frac{2(\sigma_p b)\sin\left(\frac{\Delta\varepsilon}{2}\right)}{B_{tot}v}\right]$$

Where *v* is the velocity of the dislocation, *b* the Burgers vector of the dislocation, σ_p is the

Peierls stress, N_d is the number of dislocations in the contact area, ε is the misorientation angle

from a commensurate surface, and B_{tot} is the sum of the electronic, flutter, and phonon wind

contributions to dislocation drag. For these purposes I consider only incommensurate surfaces

and set ε to be a constant 10° angle. Then, for a given velocity of relative motion, only B_{tot} and N_d

need to be determined.

For the calculation of B_{tot} (which can be decomposed into different crystalline interactions

with the moving strain field of a dislocation), the reader is referred to the paper by Merkle and

Marks [74] and references therein, including Al'shitz [128] as the derivations are quite complex.

N_d is simply determined by multiplying the areal density of dislocations by the contact area πa^2 (spheres and cones) or $2a^2$ (square pyramids) as determined by force equilibrium:

$$\frac{F_N}{\pi a^2} = H \Rightarrow a = \sqrt{\frac{F_N}{\pi H}} \quad (spheres, cones)$$

(6.2)

$$a = \sqrt{\frac{F_N}{2H}} \quad (square\ pyramids)$$

Where F_N is the normal load and H is the generalized hardness, or resistance to plastic deformation, which combines the elastic and plastic material responses – increasing H will reduce the contact area for a given normal load. Both H and F_N may vary from experiment to experiment, but H was held constant in this model while the variability of F_N is explored. Hardness values may vary by hundreds of percent depending on treatment of course, but 500 MPa was chosen as a typical value based on reported Brinell and Vickers hardnesses in literature. [129]

Lastly, since Equation (6.1) is the macroscopic force per unit length, I multiply by the dislocation length to get the total force experienced by the asperity. I use the grain size of 0.1 mm as an upper bound for this value.

6.2.2 Plowing via Dislocation Power Law Creep

The plowing component of friction deals with the force necessary to physically push the material in front of the asperity aside. The plowing term in the BT model is given by the cross-sectional area of the groove track caused by the asperity, multiplied by the "flow pressure" (i.e. the necessary instantaneous stress to cause or continue plastic deformation).

Rather than analyzing this along the same lines as in the original BT model, I use a more standard materials science approach and deal with the plastic deformation as creep. The deformation mechanisms maps for copper, seen in Figure 6.2, show us which mechanisms are dominant in which temperature-stress regimes. For high-temperature (relevant at approximately half the melting temperature and up), power law creep, the semi-empirical relationship between shear strain rate and shear stress is known:

$$\dot{\gamma} = A_2 \frac{D_v Gb}{kT}\left(\frac{\sigma_s}{G}\right)^n$$

(6.3)

where D_v is the diffusion coefficient (neglecting dislocation core diffusion), b is the relevant Burgers vector, G the shear modulus, σ_s is the shear stress, n is the power law creep exponent, and A_2 is the appropriate Dorn constant. For $n = 3$ and $A_2 = 1$, this relation is quite general and can be derived from physical models of dislocation mechanics. [130] However, most materials require variation of these two parameters to fit experimental data, for reasons which are not completely clear. As a result, experimental analysis of copper is required to determine the values of A_2 and n.
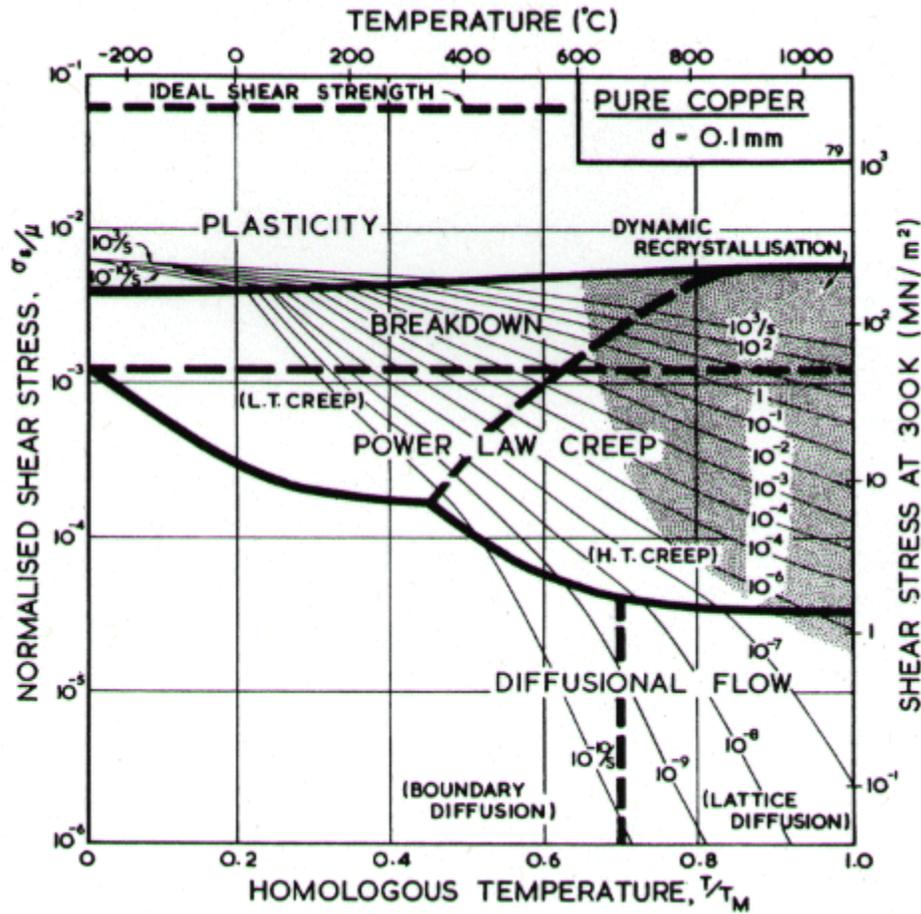
Figure 6.2: Deformation mechanisms map for copper, showing the temperatures and stresses where power law creep dominates. [130]

An Arrhenius-like temperature dependence is built in for the diffusion constant D_v, and the

modulus G has a temperature dependence as well: [130]

$$D_v = D_{0v}e^{-\frac{Q_v}{RT}}$$

(6.4)

$$G = G_0\left(1 + \frac{T-300}{T_m}\right)\frac{T_m}{G_0}\frac{dG}{dT}$$

(6.5)

Where D_{0v} is the pre-exponential component, Q_v is the activation energy for lattice diffusion,

and RT is temperature times the gas constant. Similarly G_0 is the pre-modified modulus with T_m

being the melting temperature. Table 6.1 is a summary of the material specific constants used in

the above equations, as collected in [130].

Name	Symbol	Value	Source
Dorn constant for shear stress	A_2	1.79×10^7	[3, 62]
Lattice diffusion coefficient (pre-exponential)	D_{0v}	2×10^{-5} m^2/s	[4]
Lattice diffusion activation energy	Q_v	197 kJ/mol	[4]
Shear modulus (at 300 K)	G_0	4.21×10^4 MPa	[131, 132]
Shear modulus temperature dependence	$\dfrac{T_m}{G_0}\dfrac{dG}{dT}$	-0.54	[131, 132]
Power law creep exponent	n	4.8	[3, 62]
Melting temperature	T_m	1356 K	[130]
Burgers vector	b	2.56 Å	[130]

Table 6.1. Material specific constants for copper from literature.

Now, for a given asperity velocity, the shear strain rate in the material can be geometrically

determined. This rate is solely dependent on the velocity and the relevant distance over which the

dislocation deforms the material. This distance, the reference length for plastic deformation,

allows us to calculate the normalized strain by comparing the material deformation at one point

with another. The reason the asperity contact radius is not taken as the reference length is that the

material deformation takes place as the material moves around the asperity regardless of its size.

In this case, the distance from the dislocation core where the typical stationary strain field drops

off to 1% is used. For a screw dislocation, the strain field at a distance *r* is proportional to 1/*r*,

leading to a reference length of ~100*b*.

I assume, purely geometrically, that material in front of the tip must travel on a horizontal

flow line around the tip to the side (one quarter circle or along one edge, as seen in Figure 6.3) at

the same time as the tip progresses forward one radius.
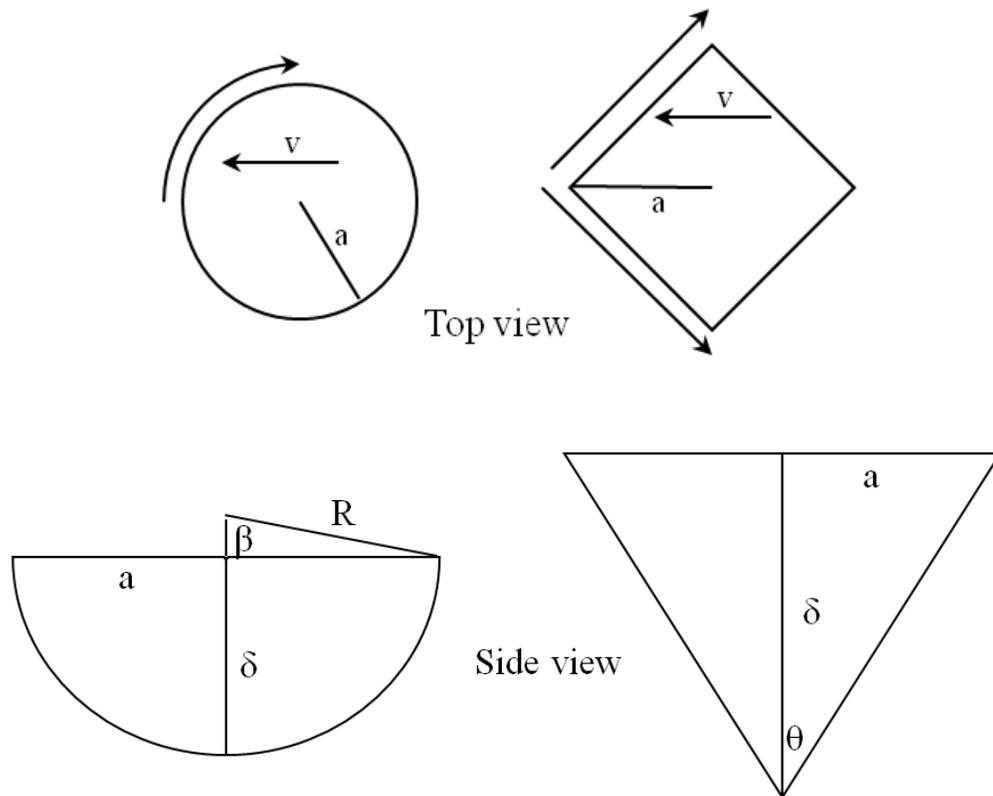
Figure 6.3. Top: The top view of (left) spherical and conic asperities and (right) square pyramidal asperities as they plow through material. The arrows show the distance the plowed material has to travel whenever the asperity advances by one radius. The contact radius a actually cancels out resulting in the same strain rate regardless of size.

Bottom: The cross sectional areas where plowing occurs for sphere (left) and cone/square pyramid asperities (right). The penetration depth δ is marked along with the contact radius a and cone angle θ.

Since the velocity of the tip is known, the time it takes to travel one radius forward can be

calculated: $t = a/v$. Plugging this in to the motion of the plowed material yields an expression for

the rate the material must move: $\dfrac{2\pi a}{4} \cdot \dfrac{v}{a} = rate = \dfrac{\pi v}{2}$, or for a square pyramid,

$\sqrt{2}a \cdot \dfrac{v}{a} = rate = \sqrt{2}v$. The shear strain rate that the plowed material must experience is this rate

divided by the reference distance: $\dot{\gamma} = \dfrac{\pi v}{200b}$ or $\dot{\gamma} = \dfrac{\sqrt{2}v}{100b}$ for a square pyramid.

In the shear stress and temperature regime where power law creep is the dominant deformation mechanism, the two shear strain rates can be equated. In the case of a cone-shaped asperity:

$$\dot{\gamma} = A_2 \frac{D_v G b}{kT}\left(\frac{\sigma_s}{G}\right)^n = \frac{\pi v}{2 \cdot 100b}$$

Rearranging to solve for the shear stress,

(6.6)
$$\left(\sigma_s{}^n\right)^{\frac{1}{n}} = \sigma_s = G \cdot \left(\frac{kT\pi^2 v}{200 A_2 D_v G b^2}\right)^{\frac{1}{n}}$$

The form is identical for spheres and square pyramids with slightly different constants. The final step is to multiply the shear stress by the cross-sectional area of the asperity responsible for plowing, e.g. Figure 3b. This will result in the plowing force that the asperity needs to exert in order to move material out of the way through creep. That is the frictional force we're looking for.

The contact radius is determined from force equilibrium as mentioned above, but the penetration depth is needed as well. For conic and square pyramid asperities the penetration

depth will depend on the angle of the tip θ (smaller angles result in greater penetration for the same contact area and force), which will vary. It can be seen from Figure 2b that $\tan\theta = a/\delta$, therefore $\delta = a\cot\theta$. For a sphere, the geometry is a bit more complicated but it should be clear that $\delta = R - R\cos\beta$, where $\beta = \sin^{-1}(a/r)$.

The frictional force due to plowing can then be easily written since the cross-sectional area A is simply the area of a triangle for a cone or pyramid, and the area of a circular segment for a sphere:

$$F_C = \sigma_s A$$

(6.7)
$$F_C = Ga^2 \cot\theta \cdot \left(\frac{kT\pi^2 v}{200 A_2 D_v Gb^2} \right)^{\frac{1}{n}}$$

(6.8)
$$F_C = Ga^2 \cot\theta \cdot \left(\frac{\sqrt{2}kT\pi v}{100(2+\sqrt{2}) A_2 D_v Gb^2} \right)^{\frac{1}{n}}$$

(6.9)
$$F_C = G \cdot \left(\frac{kT\pi^2 v}{200 A_2 D_v Gb^2} \right)^{\frac{1}{n}} \cdot \left[R^2 \cos^{-1}\left(\frac{R-d}{R} \right) - (R-d)\sqrt{2Rd - d^2} \right]$$

Where Equation (6.7) is for a cone with angle θ, Equation (6.8) is for a square pyramid with angle θ, and Equation (6.9) is for a sphere with radius of curvature R. See Goddard and Wilman for an analysis of the contact mechanics of differently-shaped asperities. [133]

These equations for the creep force F_C combine with the F_D term given by Equation (6.1) and the appropriate dislocation length l to give the friction coefficient μ:

$$(6.10) \qquad \mu = \frac{F_D l + F_C}{F_N}$$

6.3 Results and Discussion

In general, modeling the plowing component of friction as a result of material deformation –

in this case, power law creep – seems to be a feasible approach. As will be shown below the

trends and values are in general consistent with the literature.
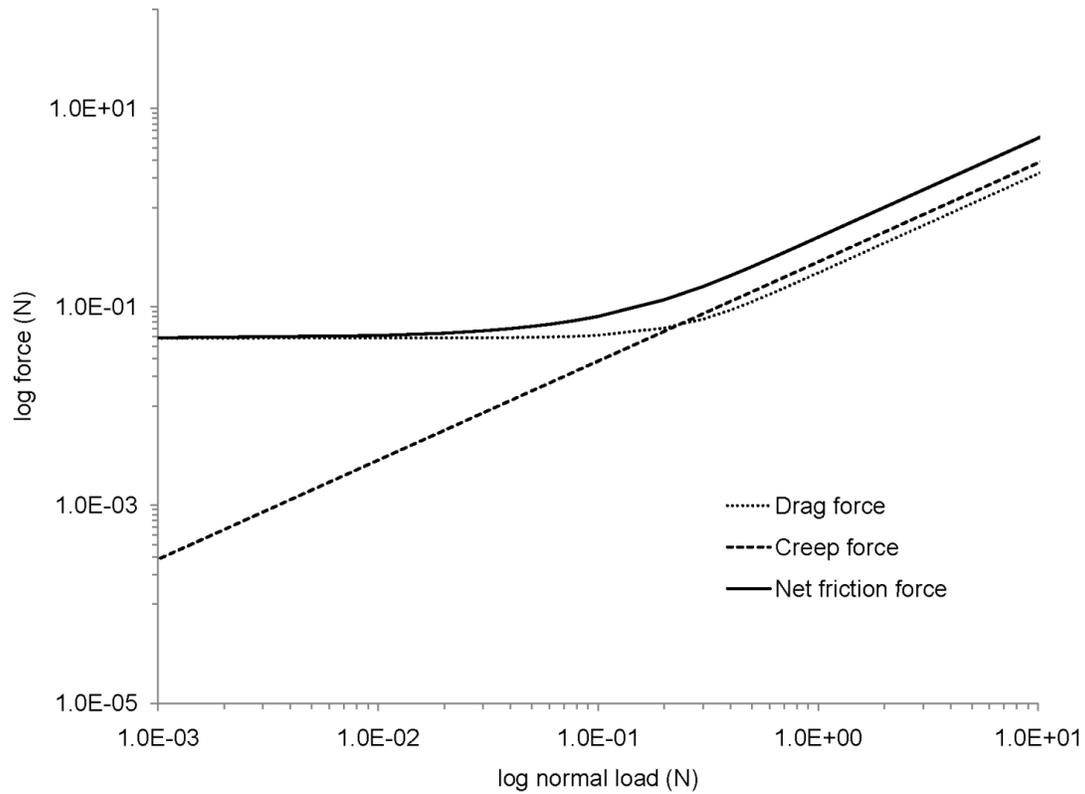
Figure 6.4. Friction force vs. normal load. 100 m/s sliding velocity, and cone angle 10º.

At high normal loads, shown in Figure 6.4, the increase in net friction force becomes directly proportional to load, meaning the coefficient of friction becomes a constant. The increasing normal load in this model is tied to increasing contact area, and it is evident that at high loads, the increase in the drag force becomes dominated by the increase in contact area, and corresponding increase in the number of dislocations at the sliding interface. The creep force has the same dependence on the horizontal projected contact area regardless of the force, so this result is to be expected.

Figure 6.5 compares the drag (adhesive) and creep (plowing) components to total friction. The dislocation model predicts a transition (curved region on the plot) where the dominant source of drag goes from radiative to viscous effects. The influence of plowing friction is most felt in this regime, where the total friction deviates most from the adhesive force. Also note, under similar circumstances, the spherical asperity produces less plowing due to the higher aspect ratio of the cone and square pyramid. For these parameters, the ratio of plowing to adhesive components of the friction coefficient falls within the reported range for measured metal-on-metal friction. [134]
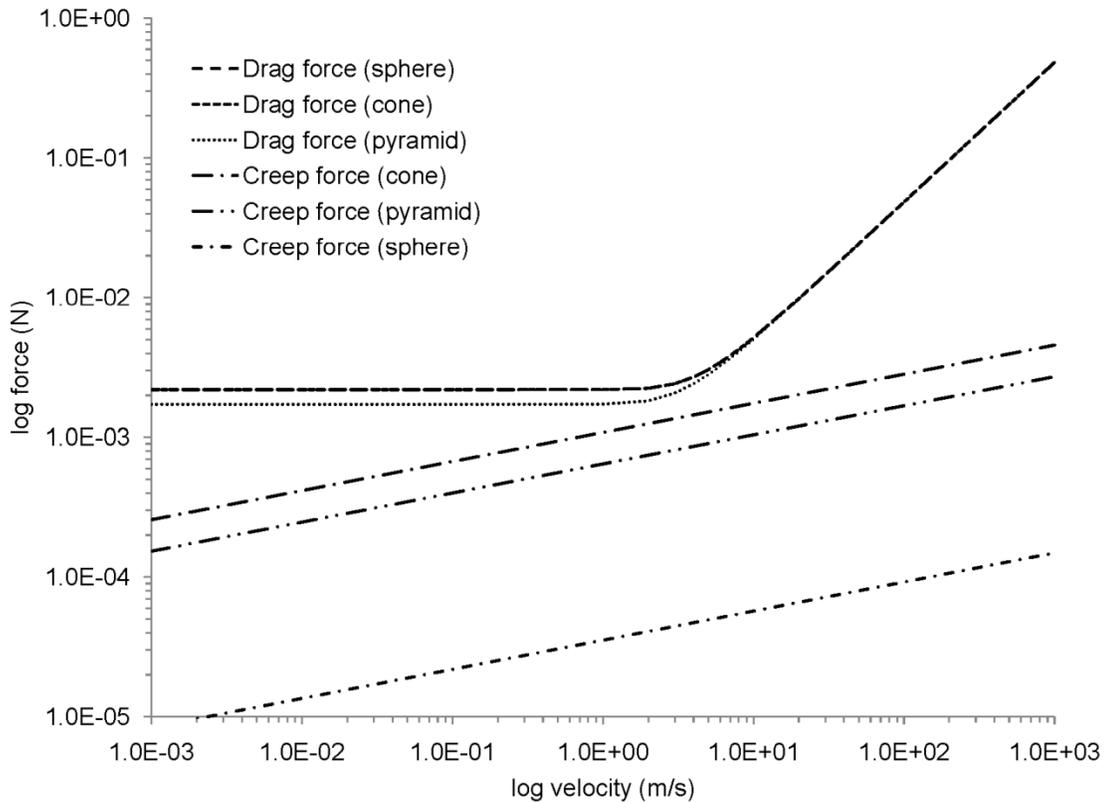
Figure 6.5. Creep and drag forces vs. sliding velocity and asperity shape. Normal load 10 mN, temperature 0.8 T_m, cone/pyramid angle 20º, and sphere radius of curvature 1 µm.

Figure 6.6 shows the isolated effect of increased plowing severity while holding the drag force constant. A similar plot will be obtained if you plot the data vs. penetration depth. As the cone angle decreases for a given load, the asperity must penetrate deeper into the material to maintain force balance. Under significant plowing (0.1 radians corresponds to a 3.55 µm penetration depth), the plowing force will dominate. This trend is consistent with reported experimental and theoretical penetration depth dependence, considering an asperity with finite penetration depth would result in a constant creep force once the cone angle becomes small enough. [120, 135] It is also clear that increasing temperatures not only increase the absolute contact areas, increasing friction overall, but increase the creep component of the total friction.

At higher temperatures, the material deforms more easily by creep, resulting in lower frictional

forces.
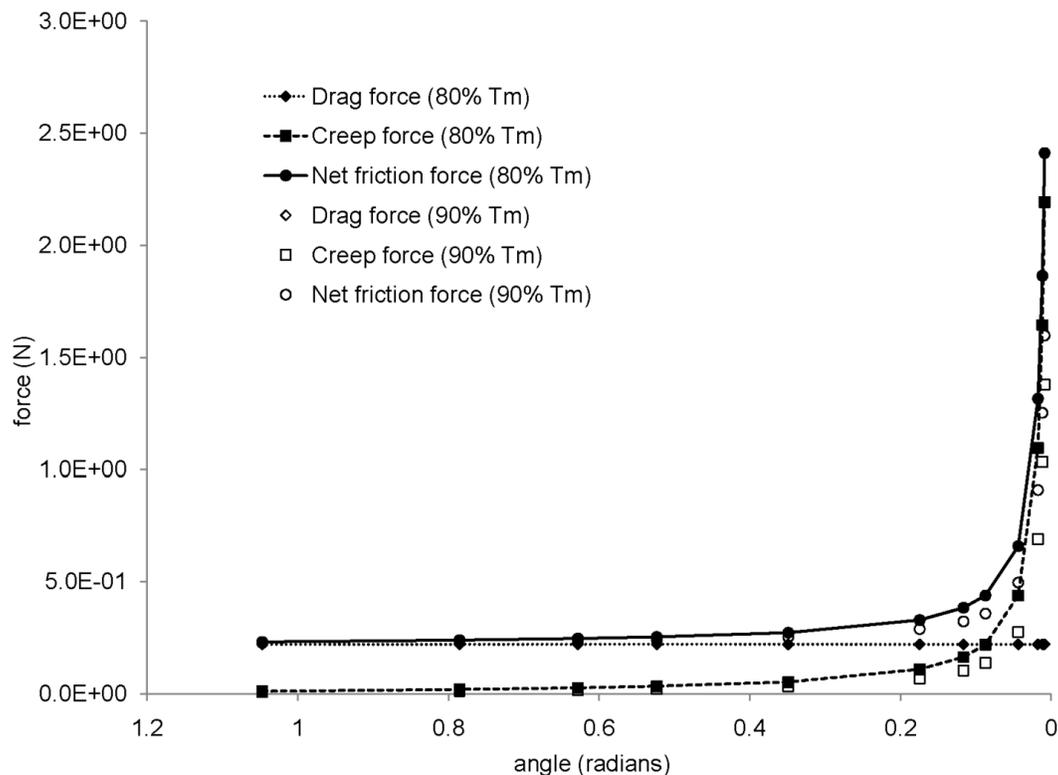
Figure 6.6. Friction force vs. cone angle and temperature. For a cone-shaped asperity, 1 m/s, 1 N load. A decrease in the cone angle corresponds directly to an increase in the penetration depth of the asperity, for the same normal load.

I have presented a straightforward dislocation-based interpretation of the BT shear and

plowing model. The formulation uses an analytical continuum approach to predict the steady-

state friction forces to first order at a sliding interface, with only a few well-known

experimentally-derived parameters necessary. The predictions from this model – in particular,

the power law creep mechanism for plowing friction – have good correspondence with measured

results, and using only dislocation-based deformation mechanisms can account for a good deal of

tribological behavior. Not only is this approach easily modifiable and extendable to other

materials, but it is able to offer alternative explanations for known phenomena in a materials science context. In that sense, we have seen that this approach can be quite effective in understanding fundamental trends in friction behavior and therefore, how they can be affected by materials design.

Chapter 7

Evaluation of Shielding Effects on the Drag of Dislocation Arrays

7.1 Phonon Drag on Moving Dislocations

As we've argued, the link between tribology and materials science can be explored through dislocations. Dislocations in crystals are often the preferred deformation mechanism, and I have used that idea in the previous chapter to connect what we know about that deformation process to what we know about how energy is dissipated during a sliding contact. In this chapter I will take the idea one step further, by looking at the dissipative forces acting on dislocations themselves. If dislocation motion represents the dissipation of energy that corresponds in some sense with friction, then the resistance to dislocation motion through a crystal must also be implicated as a tribological process. In this chapter, we will widen our scope to consider arrays of dislocations. Throughout literature, dislocation arrays have been treated equivalently to single dislocations when it comes to interaction and drag forces. The premise is that since drag results from directional forces that dissipate energy, arrays of dislocations should behave differently than single dislocations due to shielding effects.

Stable arrays of dislocations form when nearby dislocations are attracted into an energy-lowering configuration. Many such equilibrium distributions of dislocations are possible, including tilt and twist boundaries, but non-equilibrium configurations are also seen. Read and Shockley showed that any low-angle grain boundary can be thought of as an array of

dislocations. [136] Arrays of dislocations are therefore involved in material deformation, in an accommodating way such as glide on a slip plane or grain boundary rotation [137-140], or as barriers such as in the cases of dislocation pile-up. [141-143] The motion of such arrays is therefore important to understanding the deformation, and by extension, the tribological behavior of the crystal. I concentrate here on the effects of phonons on that motion.

The viscous interaction between phonons and the stress fields of dislocations is well-understood and a significant contributor to the drag force on moving dislocations in crystalline solids. [128, 144-146] Phonons can be generally thought of as elastic waves with a frequency and energy, with a density of states throughout k-space. Like other collective oscillations, phonons can be considered quasiparticles carrying a pseudomomentum $\hbar k$ where k are the reciprocal lattice vectors and $\hbar$ is Planck's constant. The phonon frequencies are given by the Bose-Einstein distribution up to what is called the Debye limit – the upper bound to phonon energy at which the wavelength would become shorter than the lattice spacing.

When they fall within the appropriate energy range, phonons can be scattered inelastically by dislocations. There are two distinct scattering mechanisms. The static mechanism, which will be considered in this work, involves the anharmonic interaction between the strain fields of the phonon and the dislocation. There is also a vibrational mechanism – known as fluttering – where a pinned length of dislocation has a resonant frequency that matches a phonon frequency. During either scattering event, momentum can be exchanged between the phonon and dislocation; therefore a moving dislocation will encounter a net loss in momentum in a viscous manner, due to the anisotropy of incident phonons. Particularly at low temperatures where thermally activated dissipation mechanisms are limited, this phonon wind effect can be an important component of

dislocation drag, and by extension, frictional losses. [147] To put this in perspective, these drag forces are not of the same order of magnitude as most externally applied stresses, but they can comprise a significant part of the dissipative forces at work, particularly in certain regimes. [74]

Like other forms of macroscale viscous drag, it is a reasonable hypothesis that the drag force due to the phonon wind should be partially shielded when incident on a moving array of dislocations. In particular, first-order shielding effects should cause the array as a whole to experience proportionally less drag than a single dislocation in isolation. By first-order, I am referring to the shielding from the nearest neighbor with no other consideration. Depending on the array, other dislocations may contribute to the shielding to a lesser extent. It is also conceivable that shielding effects may change the equilibrium spacing of the array and therefore contribute higher order terms to the outcome. I will ignore these factors here and concentrate on the result from the closest dislocation. I use a geometric model to estimate the magnitude of the shielding effects and determine the validity of the ubiquitous single dislocation approximation.

7.2 Model Framework

a   b
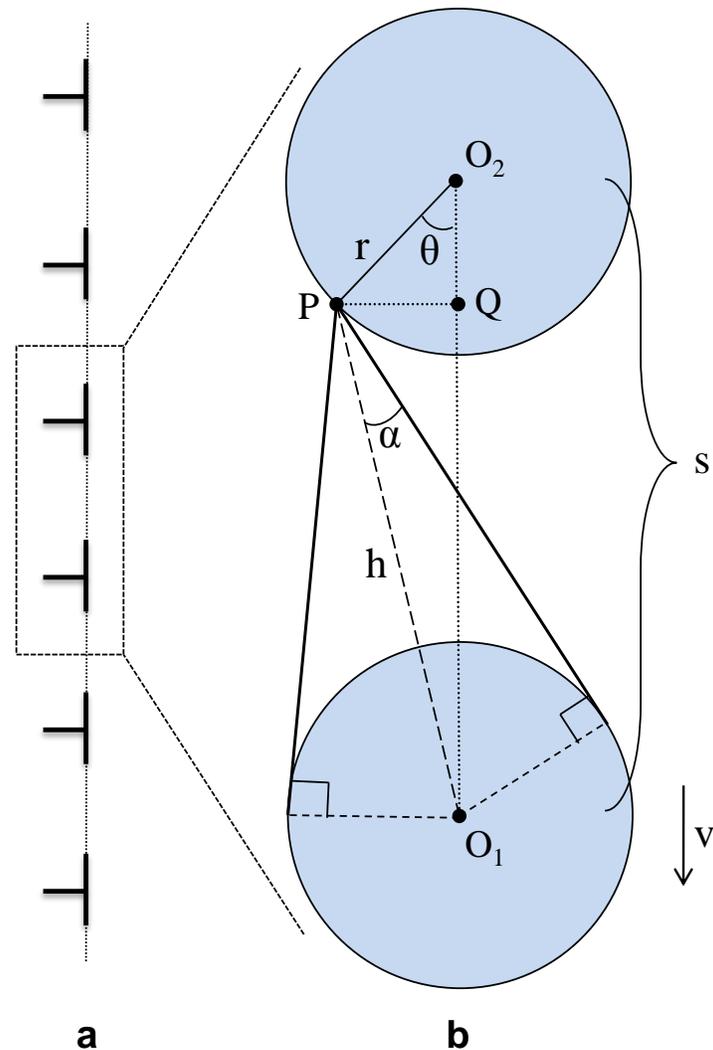
Figure 7.1. Schematic of the shielding geometry. **a)** A typical array of edge dislocations with the same Burgers vector glide through a crystal on a slip plane. Phonons incident on the array with momentum counter the direction of motion are considered. **b)** Nearest neighbor dislocations in a 1-D array are represented as spheres, and reduced here to circles due to spherical symmetry. Their spacing is s, their scattering cross-section is r, and they move with velocity v. At every point P on the forward-facing hemisphere of the shielded dislocation O_2, the angles occluded due to O_1 are calculated using h and θ and integrated to yield the total percentage of the hemisphere shielded.

Consider a one-dimensional array of dislocations in copper gliding on a slip plane, as shown in Figure 7.1a. The amount of shielding is geometrically determined, and depends on the scattering cross-section r of a dislocation to an incident phonon wavetrain, as well as the spacing s between dislocations.

The dislocations are represented in two dimensions as circles with radius equal to the scattering cross-section for the phonon scattering interaction. Phonon scattering events are assumed to prevent 100% of the phonon momentum from being transmitted farther along that vector. That is to say, the proportion of phonons prevented from interacting with the shielded dislocation is the same as the proportion of opposing momentum that the dislocation does not feel. When considering the incident phonon momentum, the contribution to the drag force (in Figure 7.1b, the vertical component in the $-v$ direction) depends on the cosine of the angle between the phonon wavetrain and the dislocation motion – in this system, this adds a factor of $\cos\theta$. For a typical shielding of 15° around the vertical, however, the contribution to the drag from shielded dislocations is greater than 96%, and in the model the contribution is considered to be 100%, which is a slight overestimate. In this treatment, the horizontal momentum components cancel out.

The greatest amount of shielding will be from the nearest neighbor, so a two-dislocation system is utilized as shown in Figure 7.1b. From the coordinate system of a dislocation, incident phonons that have a component coming from the direction of motion $\vec{v}$ in the figure will contribute to drag. That is to say, all phonons incident between $\theta = -90°$ and $\theta = 90°$, as measured from the vertical, are taken into account. The shielded angles α can then be determined at each angle θ on the forward-facing half-circle of the dislocation. Taking the ratio of the

shielded to unshielded angles, integration yields the amount of phonon momentum shielded as a percentage of the total momentum.

Consider first the right triangle with hypotenuse h formed by points O_1, P, and Q. The horizontal and vertical sides can be calculated using the trigonometry of the circle O_2. Using the Pythagorean theorem and simplifying:

$$(7.1) \qquad h = \sqrt{(r\sin\theta)^2 + (s - r\cos\theta)^2} = \sqrt{r^2 + s^2 - 2sr\cos\theta}$$

Next consider the right triangle formed by O_1, P, and a tangent point to circle O_1. Again the hypotenuse is h, so the equation for α is written by rearranging the trigonometric relationship:

$$h\sin\alpha = r$$
$$2\alpha = 2\sin^{-1}\left(\frac{r}{h}\right)$$

Lastly I integrate over the edge of the shielded dislocation. The occluded portion of the half-circle, integrating over θ, is given by:

$$2\int_{0}^{\frac{\pi}{2}} \frac{2\alpha}{\pi} d\theta$$

This is subtracted from the total integral over the half-circle, and using (7.1) this yields the proportion of incident phonon momentum exposed to the shielded dislocation, (7.2).

$$(7.2) \qquad 2\int_{0}^{\frac{\pi}{2}} 1\, d\theta - 2\int_{0}^{\frac{\pi}{2}} \frac{2\alpha}{\pi} d\theta = \pi - \frac{4}{\pi}\int_{0}^{\frac{\pi}{2}} \sin^{-1}\left(\frac{r}{\sqrt{r^2 + s^2 - 2sr\cos\theta}}\right) d\theta$$

The dislocation Burgers vector b is taken to be that of a typical FCC metal slip plane, which encompasses a range of 2.5 Å to 2.88 Å, including copper, aluminum, nickel, silver, gold, and platinum. [148, 149] The relevant scattering cross-section is taken to be twice the Burgers vector as suggested by Hikata et al. [150] Due to the anisotropy of a dislocation's displacement field in the crystal, the scattering cross section is also dependent on the incident phonon angle. For random incident angles the adjustment to r can be calculated to be between 0.5 and 2 times. [146, 151] Results are presented for a variety of dislocation spacings, as this will be determined by the experiment.

7.3 Results and Discussion

Figure 7.2 shows the phonon exposure of the shielded dislocation as a percentage of the full unshielded exposure, calculated numerically from Equation (7.2).
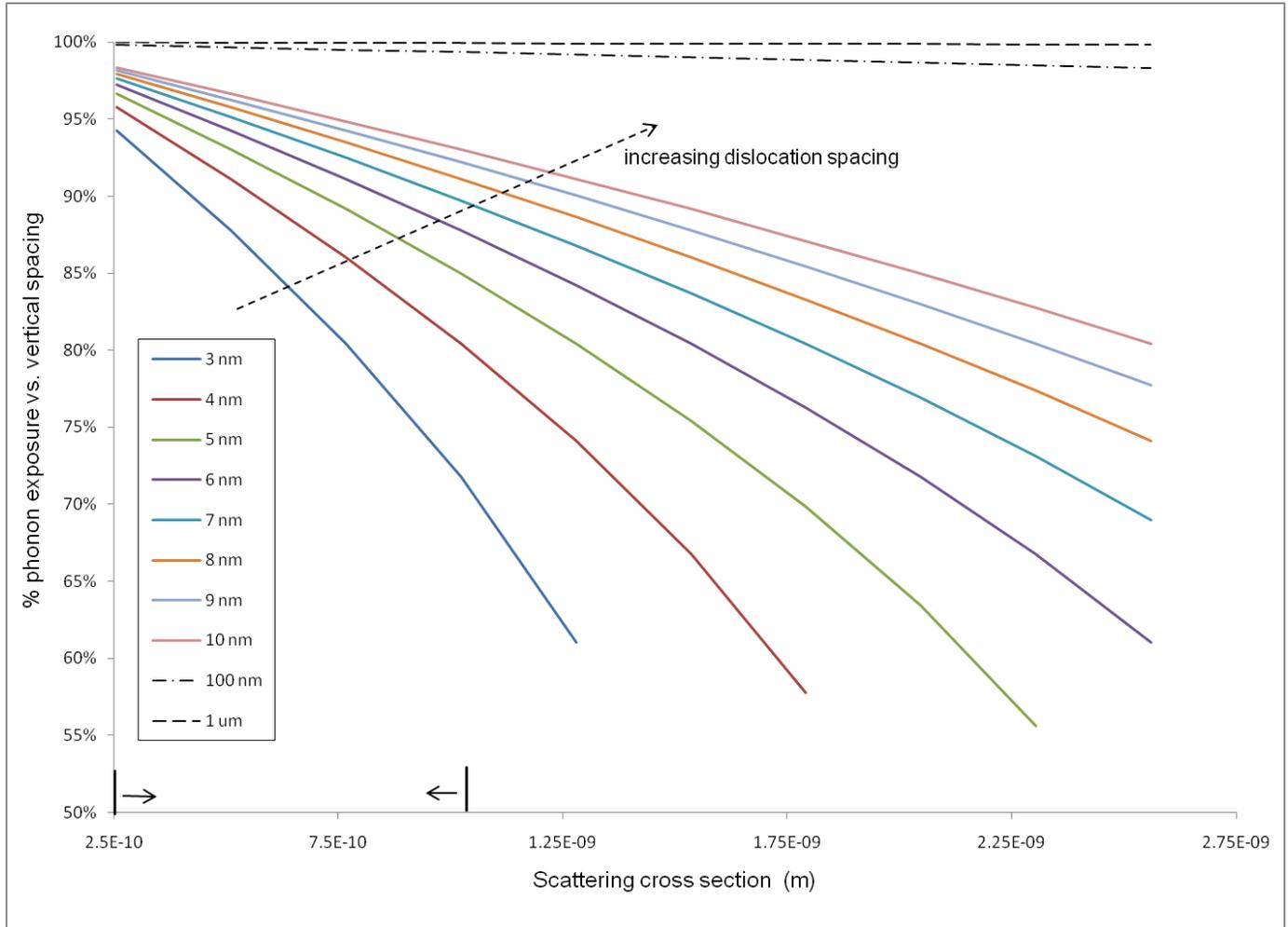
Figure 7.2. The percentage of phonons that will be incident on the shielded dislocation, as a function of scattering cross-section – 100% represents no shielding effect, 0% represents complete shielding. Results for a range of spacings are shown. The relevant cross-sections are indicated with bounding arrows, encompassing the range between one-half and twice the average $\sigma = 2b$.

Under these conditions the model shows that for $r = 2b$, the exposure is 88% at the closest geometrically possible spacing.

The model shows the effect of shielding as a function of scattering cross-section and dislocation spacing. Realizing that in actual materials, phonon momentum will not be completely absorbed by the first interaction, it seems clear that unsurprisingly, only a negligible effect will

remain in most situations. Throughout these calculations the maximum possible drag reduction at the closest possible spacing was considered, and the result was still a small effect. This is consistent with the typical experimental result that matches single-dislocation theory within 10-15%.

The three-dimensional symmetry of the system means the proportional reduction in drag is the same as the two-dimensional result, when all dislocations have the same length. However, the model could be extended to take into account more complicated arrays of dislocations in more than two dimensions. However, because of the previously mentioned diminishing component of shielded momentum in the drag direction with higher angles θ, the nearest neighbor dislocation in the direction of motion – as discussed above – will be the dominant scatterer.

It is important to remember that phonons are collective oscillations of the entire crystal lattice and therefore a long-range phenomenon. Local disruptions in the strain field, such as point defects, would not be expected to affect an array of dislocations any differently than a single dislocation.

In summary, a geometric model is used to account for the shielding effect of nearest neighbors on the phonon wind drag experienced by moving dislocations in a one-dimensional array. In order to calculate the theoretical maximum reduction in drag due to this effect, the case where scattering events shield 100% of the phonon momentum is considered. As expected, even with these assumptions creating an overestimate of the true effect, the shielding effect is relatively small. For the relevant scattering cross-section for copper, the reduction in phonon

momentum incident on shielded dislocations is calculated as not exceeding 12%, the shielded portion of the half-circle at the closest spacing. Considering the variability in the scattering cross-section, the model concludes that treating an array of moving dislocations as a single dislocation is an approximation accurate to within 6-25%, which can be considered valid. Although dislocation arrays remain important structures with distinct properties, this modeling shows that shielding effects are not a significant factor in their drag behavior.

Chapter 8

Future Directions for Research

8.1 *In Situ* TEM Experimentation

The work described here has several avenues which could be further explored. One of course is the extension of the chemical bonding analysis to similar films as a function of hydrogenation or dopant. While we know that the sp^3 to sp^2 phase transformation occurs during sliding, determining whether the process is aided or inhibited by various additives will be useful for engineering design. Several other variables could also be explored, particularly the sliding velocity and the normal load. For a more thorough normal load experiment, an AFM-TEM holder might be more suitable for its force measurement capability.

Another opportunity for future work is an extension to measuring actual friction coefficients. While this does not shed any light on the nanoscale mechanisms, it does provide indirect information on the effects of differing film bonding composition on actual performance. Because the sp^3 to sp^2 transition has been observed to occur in a dispersed way throughout the film, the effect on surface tribology will likely be different than a surface layer of graphite. Testing of hardness and other mechanical characteristics of films post-sliding would also make for a more comprehensive understanding of the implications of changes to the chemical bonding, both in terms of magnitude and how quickly the behavior changes as a function of sliding passes.

Bonding state analysis can prove useful in many other contexts as well, including characterization. A similar technique could be used to infer compositional information on a precise scale by looking at bonding environments in carbide samples. Because of the direct correlation between the observable sample area and the measurement, localized experimentation such as applied bias through the tip or nanoindentation can also benefit from this sort of analysis.

I also demonstrated here a strong, localized connection between the mechanical activity of the probe tip and the rate of tribochemical wear. However, this could be established with more precision by carefully measuring the chemical composition as a function of position relative to a wear track, using line scans or elemental mapping in scanning TEM mode, or energy-filtered mapping with the GIF. It might also be feasible to perform a sliding test on a marked grid, turn the grid over and do localized chemical analysis on the underside of the film, for films of varying thickness. This would require a surface sensitive technique such as x-ray photoelectron spectroscopy.

Furthermore, it is clear that relatively small impurities may play a large role if the chemical activity is high enough. A useful test would be to determine the correlation between, for example, water vapor partial pressure and wear rate. This could be done using a system with a more carefully controlled environment. In my vacuum experiments, the overall pressure was 10^{-7} torr, with water vapor partial pressure likely 1-2 orders of magnitude smaller, and some variability would be expected in the range between those and these environmental TEM experiments.

Not only are different environments expected to have differing chemical activities, but to interact with the film in different ways, as seen with the hydrogen passivation. It should be possible and useful to measure, in this case, how much hydrogen pressure is necessary to maintain low chemical wear rates. This kind of study could be done not only with hydrogen gas and water vapor, but with nitrogen and oxygen gases as well.

The question also remains, with chemical reaction studies such as these, what differences can be observed in closed atmospheres versus those that have flowing sources of gas. In particular, if there are equilibrium states that occur during a sliding test where the chemical wear rate stops despite continued mechanical activation of the film, this can provide quantitative evidence of the involvement of a particular species.

8.2 Defect Based Analytical Modeling

The structure of the model – and its basis in the BT approach – provides the ability to easily incorporate additional phenomena, such as asperity deformation [152], shear-localized chip formation [153], dislocation pinning, grain boundaries, and other energy dissipation mechanisms.

This work has focused on a specific temperature-pressure regime, and therefore there are large pieces of the dislocation theory - tribology relationship left to fill in. Other relationships, involving creep and otherwise, can certainly be fleshed out, although what is possibly of more interest are the boundaries between regions on the deformation map. At these boundaries, the material deforms in multiple ways simultaneously, and the situation is more complicated – and more realistic – than the case of a single dominant deformation mechanism.

In effect, it is postulated that once the material can no longer easily deform via dislocation motion, there are sharp increases in the friction from the change in deformation mechanism. Speculating further, because wear rates are analytically linked directly to friction [133], the inability for a material to deform easily via dislocations should lead to a sharp increase in the material ejected from the interface as wear. Any boundary regimes between two deformation mechanisms might experience a similar increase in friction and wear.

When it comes to drag, the details of the phonon-dislocation interaction are complex, and are one aspect of this work which could be further explored. In particular, the amount of phonon momentum that is actually transferred to the dislocation is likely to vary as a function of the type of dislocation (or other line defect) involved, as well as the incident angle. Similar dependencies are likely for the scattering cross-section of the dislocation itself. More accurate modeling will be useful for those systems where phonon wind drag plays a large part in the overall behavior of the system.

The effect of defect arrays on not just thermal but electrical conductivity could also be explored, if one considers dislocations or other defects such as twin boundaries as exerting a drag on the conduction of phonons or free electrons. Much work has already been done on the effects of dislocations on electron transport. [72] It may be that highly ordered defects reduce conductivity by a lesser amount than randomly oriented defects. In fact, for both phonons and electrons, the difference between uniform and random angles of incidence may be striking. In this work I assumed that the randomness resulted in an error to the scattering cross-section of plus or minus a factor of two. It is likely that uniform angles will affect momentum transfer as well.

There is also work to be done in the details of how arrays of dislocations form and move together, in terms of the energy required and the various forces involved. Certainly, equilibrium dislocation distributions exist, but how are they affected by motion in different crystal directions? As alluded to in the background, any viscous drag force must be opposed to some degree by the ideal equilibrium spacing in the array, and so there will be second and higher order effects to consider.

In a more general sense, interaction effects between defects will be a relevant aspect of many deformation situations, yet are often neglected. Further theoretical and experimental investigation into the effect of defect density and structure on performance is warranted, although it remains difficult to isolate higher order interaction effects from phenomena like tangling, pinning, and defect formation or destruction due to external factors.

References

[1] Dowson, D.: History of tribology, Professional Engineering Publishing, London (1998)

[2] Jost, H. P.: Tribology - Origin and Future. Wear 136, 1-17 (1990)

[3] Barrett, C. a. S., OD: Steady-state creep characteristics of polycrystalline copper in the temperature range 400 degrees to 950 degrees C. Trans Metall Soc AIME 230, 1322-1327 (1964)

[4] Kuper, A., Letaw, H., Jr., Slifkin, L., Sonder, E., Tomizuka, C. T.: Self-Diffusion in Copper. Physical Review 96, 1224-1225 (1954)

[5] Whelan, M. J.: Reminiscences on the early observations of defects in crystals by electron microscopy. Journal of Electron Microscopy Technique 3, 109-129 (1986)

[6] Couret, A., Crestou, J., Farenc, S., Molenat, G., Clement, N., Coujou, A., Caillard, D.: In situ deformation in T.E.M.: recent developments. Microsc Microanal Microstruct 4, 153-170 (1993)

[7] Lockwood, A. J., Anantheshwara, K., Bobji, M. S., Inkson, B. J.: Friction-formed liquid droplets. Nanotechnology 22, 105703 (2011)

[8] Kopac, J., Sokovic, M., Dolinsek, S.: Tribology of coated tools in conventional and HSC machining. Journal of Materials Processing Technology 118, 377-384 (2001)

[9] Merkle, A. P., Marks, L. D.: Liquid-like tribology of gold studied by in situ TEM. Wear 265, 1864-1869 (2008)

[10] Simões, S., Calinas, R., Vieira, M. T., Vieira, M. F., Ferreira, P. J.: In situ TEM study of grain growth in nanocrystalline copper thin films. Nanotechnology 21, 145701 (2010)

[11] Legros, M., Gianola, D. S., Hemker, K. J.: In situ TEM observations of fast grain-boundary motion in stressed nanocrystalline aluminum films. Acta Materialia 56, 3380-3393 (2008)

[12] Sasaki, K., Murase, T., Saka, H.: In-situ transmission electron microscopy of grain boundaries in CuGa2. Ultramicroscopy 56, 184-192 (1994)

[13] Liao, Y., EswaraMoorthy, S. K., Marks, L. D.: Direct observation of tribological recrystallization. Philosophical Magazine Letters 90, 219-223 (2010)

[14] Wang, J. J., Lockwood, A. J., Peng, Y., Xu, X., Bobji, M. S., Inkson, B. J.: The formation of carbon nanostructures by in situ TEM mechanical nanoscale fatigue and fracture of carbon thin films. Nanotechnology 20, 305703 (2009)

[15] Merkle, A. P., Erdemir, A., Eryilmaz, O. L., Johnson, J. A., Marks, L. D.: In situ TEM studies of tribo-induced bonding modifications in near-frictionless carbon films. Carbon 48, 587-591 (2010)

[16] Liu, Y. A. N., Meletis, E. I.: Evidence of graphitization of diamond-like carbon films during sliding wear. Journal of Materials Science 32, 3491-3495 (1997)

[17] Kanda, K., Yamada, N., Okada, M., Igaki, J.-y., Kometani, R., Matsui, S.: Graphitization of thin films formed by focused-ion-beam chemical-vapor-deposition. Diamond and Related Materials 18, 490-492 (2009)

[18] Eryilmaz, O. L., Erdemir, A.: TOF-SIMS and XPS characterization of diamond-like carbon films after tests in inert and oxidizing environments. Wear 265, 244-254 (2008)

[19] Enke, K.: Some new results on the fabrication of and the mechanical, electrical and optical properties of i-carbon layers. Thin Solid Films 80, 227-234 (1981)

[20] Bhaskaran, H., Gotsmann, B., Sebastian, A., Drechsler, U., Lantz, M. A., Despont, M., Jaroenapibal, P., Carpick, R. W., Chen, Y., Sridharan, K.: Ultralow nanoscale wear through atom-by-atom attrition in silicon-containing diamond-like carbon. Nat Nano 5, 181-185 (2010)

[21] Jacobs, T., Gotsmann, B., Lantz, M., Carpick, R.: On the Application of Transition State Theory to Atomic-Scale Wear. Tribology Letters 39, 257-271 (2010)

[22] Olsen, J. E., Fischer, T. E., Gallois, B.: In situ analysis of the tribochemical reactions of diamond-like carbon by internal reflection spectroscopy. Wear 200, 233-237 (1996)

[23] Peng, L., Lee, H., Teizer, W., Liang, H.: Nanowear of gold and silver against silicon. Wear 267, 1177-1180 (2009)

[24] Ribeiro, R., Shan, Z., Minor, A. M., Liang, H.: In situ observation of nano-abrasive wear. Wear 263, 1556-1559 (2007)

[25] Kim, D. S., Fischer, T. E., Gallois, B.: The effects of oxygen and humidity on friction and wear of diamond-like carbon films. Surface and Coatings Technology 49, 537-542 (1991)

[26] Park, S. J., Lee, K.-R., Ko, D.-H.: Tribochemical reaction of hydrogenated diamond-like carbon films: a clue to understand the environmental dependence. Tribology International 37, 913-921 (2004)

[27] Sánchez-López, J. C., Erdemir, A., Donnet, C., Rojas, T. C.: Friction-induced structural transformations of diamondlike carbon coatings under various atmospheres. Surface and Coatings Technology 163-164, 444-450 (2003)

[28] Miyoshi, K.: Friction and wear of plasma-deposited amorphous hydrogenated films on silicon nitride. Adv Info Storage Syst 3, 147-160 (1991)

[29] Strom, B. D., Bogy, D. B., Walmsley, R. G., Brandt, J., Bhatia, C. S.: Tribochemical wear of carbon films in oxygen. Journal of Applied Physics 76, 4651-4655 (1994)

[30] Harrison, J. A., Brenner, D. W.: Simulated Tribochemistry: An Atomic-Scale View of the Wear of Diamond. Journal of the American Chemical Society 116, 10399-10402 (1994)

[31] Martin, J. M., Le Mogne, T., Boehm, M., Grossiord, C.: Tribochemistry in the analytical UHV tribometer. Tribology International 32, 617-626 (1999)

[32] Zhao, J., Zhu, J.: Electron microscopy and in situ testing of mechanical deformation of carbon nanotubes. Micron 42, 663-679 (2011)

[33] Merkle, A., Marks, L.: Dynamic In-Situ TEM Investigations of Tribological Interfaces. Microscopy and Microanalysis 12, 950-951 (2006)

[34] Merkle, A., Marks, L. D.: Friction in Full View. Applied Physics Letters 90, 64101 (2007)

[35] Ferrari, A. C., Robertson, J.: Interpretation of Raman spectra of disordered and amorphous carbon. Physical Review B 61, 14095 (2000)

[36] Grill, A.: Review of the tribology of diamond-like carbon. Wear 168, 143-153 (1993)

[37] Erdemir, A., Nilufer, I. B., Eryilmaz, O. L., Beschliesser, M., Fenske, G. R.: Friction and wear performance of diamond-like carbon films grown in various source gas plasmas. Surface and Coatings Technology 120-121, 589-593 (1999)

[38] Erdemir, A., Eryilmaz, O. L., Fenske, G.: Synthesis of diamondlike carbon films with superlow friction and wear properties. Journal of Vacuum Science & Technology A 18, 1987-1992 (2000)

[39] Jawid Askari, S.: Tribological characteristics of nanocrystalline diamond films grown on titanium. Surface Engineering 25, 482-486 (2009)

[40] Waqar, A., Mark, J., Htet, S. CVD Diamond Technology for Microtools, NEMS, and MEMS Applications. Microfabrication and Nanomanufacturing. CRC Press, 2005. p.187-220.

[41] Fontaine, J., Belin, M., Le Mogne, T., Grill, A.: How to restore superlow friction of DLC: the healing effect of hydrogen gas. Tribology International 37, 869-877

[42] Donnet, C., Erdemir, A.: Historical developments and new trends in tribological and solid lubricant coatings. Surface & Coatings Technology 180-81, 76-84 (2004)

[43] Erdemir, A.: Review of engineered tribological interfaces for improved boundary lubrication. Tribology International 38, 249-256 (2005)

[44] Erdemir, A.: Genesis of superlow friction and wear in diamondlike carbon films. Tribology International 37, 1005-1012 (2004)

[45] Andersson, J., Erck, R. A., Erdemir, A.: Friction of diamond-like carbon films in different atmospheres. Wear 254, 1070-1075 (2003)

[46] Heimberg, J. A., Wahl, K. J., Singer, I. L., Erdemir, A.: Superlow friction behavior of diamond-like carbon coatings: Time and speed effects. Applied Physics Letters 78, 2449-2451 (2001)

[47] Donnet, C., Mogne, T. L., Ponsonnet, L., Belin, M., Grill, A., Patel, V., Jahnes, C.: The respective role of oxygen and water vapor on the tribology of hydrogenated diamond-like carbon coatings. Tribology Letters 4, 259-265 (1998)

[48] Sánchez-López, J. C., Belin, M., Donnet, C., Quirós, C., Elizalde, E.: Friction mechanisms of amorphous carbon nitride films under variable environments: a triboscopic study. Surface and Coatings Technology 160, 138-144 (2002)

[49] Erdemir, A.: The role of hydrogen in tribological properties of diamond-like carbon films. Surface and Coatings Technology 146-147, 292-297 (2001)

[50] Erdemir, A., Eryilmaz, O. L., Nilufer, I. B., Fenske, G. R.: Effect of source gas chemistry on tribological performance of diamond-like carbon films. Diamond and Related Materials 9, 632-637 (2000)

[51] Voevodin, A. A., Phelps, A. W., Zabinski, J. S., Donley, M. S.: Friction induced phase transformation of pulsed laser deposited diamond-like carbon. Diamond and Related Materials 5, 1264-1269 (1996)

[52] Liu, Y., Erdemir, A., Meletis, E. I.: An investigation of the relationship between graphitization and frictional behavior of DLC coatings. Surface & Coatings Technology 86-7, 564-568 (1996)

[53] Liu, Y., Erdemir, A., Meletis, E. I.: A study of the wear mechanism of diamond-like carbon films. Surface and Coatings Technology 82, 48-56 (1996)

[54] Sumant, A. V., Grierson, D. S., Gerbi, J. E., Carlisle, J. A., Auciello, O., Carpick, R. W.: Surface chemistry and bonding configuration of ultrananocrystalline diamond surfaces and their effects on nanotribological properties. Physical Review B (Condensed Matter and Materials Physics) 76, 235429-235411 (2007)

[55] Erdemir, A., Bindal, C., Pagan, J., Wilbur, P.: Characterization of transfer layers on steel surfaces sliding against diamond-like hydrocarbon films in dry nitrogen. Surface and Coatings Technology 76-77, Part 2, 559-563 (1995)

[56] Ronkainen, H., Varjus, S., Holmberg, K.: Friction and wear properties in dry, water- and oil-lubricated DLC against alumina and DLC against steel contacts. Wear 222, 120-128 (1998)

[57] Cheng, C. L., Chia, C. T., Chiu, C. C., Wu, C. C., Cheng, H. F., Lin, I. N.: In situ observation of atomic hydrogen etching on diamond-like carbon films produced by pulsed laser deposition. Applied Surface Science 174, 251-256 (2001)

[58] M'Ndange-Pfupfu, A., Eryilmaz, O., Erdemir, A., Marks, L. D.: Quantification of sliding-induced phase transformation in N3FC diamond-like carbon films. Diamond and Related Materials 20, 1143-1148 (2011)

[59] Harrison, J. A., White, C. T., Colton, R. J., Brenner, D. W.: Molecular-Dynamics Simulations of Atomic-Scale Friction of Diamond Surfaces. Physical Review B 46, 9700-9708 (1992)

[60] Harrison, J. A., White, C. T., Colton, R. J., Brenner, D. W.: Investigation of the atomic-scale friction and energy dissipation in diamond using molecular dynamics. Thin Solid Films 260, 205-211 (1995)

[61] Partridge, R. H.: Excitation Energy Transfer in Alkanes. I. Exciton Model. The Journal of Chemical Physics 52, 2485-2490 (1970)

[62] Feltham, P., Meakin, J. D.: Creep in face-centred cubic metals with special reference to copper. Acta Metallurgica 7, 614-627 (1959)

[63] Berger, S. D., McKenzie, D. R., Martin, P. J.: EELS analysis of vacuum arc-deposited diamond-like films. Philosophical Magazine Letters 57, 285-290 (1988)

[64] Ponsonnet, L., Donnet, C., Varlot, K., Martin, J. M., Grill, A., Patel, V.: EELS analysis of hydrogenated diamond-like carbon films. Thin Solid Films 319, 97-100 (1998)

[65] Verbeeck, J., Van Aert, S.: Model based quantification of EELS spectra. Ultramicroscopy 101, 207-224 (2004)

[66] Bowden, F. P., Tabor, D.: The Friction and Lubrication of Solids, Clarendon Press (1958)

[67] Hamrock, B. J., Schmid, S. R., Jacobson, B. O.: Fundamentals of Machine Elements (2004)

[68] Bhushan, B., Israelachvili, J. N., Landman, U.: Nanotribology: friction, wear and lubrication at the atomic scale. Nature 374, 607-616 (1995)

[69] Weiss, M., Elmer, F.-J.: Dry friction in the Frenkel-Kontorova-Tomlinson model: dynamical properties. Zeitschrift fur Physik B: Condensed Matter 104, 55-69 (1997)

[70] Polonsky, I. A., Keer, L. M.: Scale Effects of Elastic-Plastic Behavior of Microscopic Asperity Contacts. Journal of Tribology 118, 335-340 (1996)

[71] Deshpande, V. S., Needleman, A., Van der Giessen, E.: Discrete dislocation plasticity analysis of static friction. Acta Materialia 52, 3135-3149 (2004)

[72] Look, D. C., Sizelove, J. R.: Dislocation Scattering in GaN. Physical Review Letters 82, 1237-1240 (1999)

[73] Gutkin, M. Y., Ovid'ko, I. A., Skiba, N. V.: Crossover from grain boundary sliding to rotational deformation in nanocrystalline materials. Acta Materialia 51, 4059-4071 (2003)

[74] Merkle, A. P., Marks, L. D.: A predictive analytical friction model from basic theories of interfaces, contacts and dislocations. Tribology Letters 26, 73-84 (2007)

[75] Merkle, A. P., Marks, L. D.: Liquid-like tribology of gold studied by in situ TEM. Wear 265, 1864-1869 (2008)

[76] Marks, L. D., Warren, O. L., Minor, A. M., Merkle, A. P.: Tribology in Full View. Mrs Bulletin 33, 1168-1173 (2008)

[77] Merkle, A. P., Marks, L. D.: Friction in full view. Applied Physics Letters 90, 064101 (2007)

[78] Shindo, D., Musashi, T., Ikematsu, Y., Murakami, Y., Nakamura, N., Chiba, H.: Characterization of DLC films by EELS and electron holography. J Electron Microsc (Tokyo) 54, 11-17 (2005)

[79] Erts, D., Lõhmus, A., Lõhmus, R., Olin, H., Pokropivny, A. V., Ryen, L., Svensson, K.: Force interactions and adhesion of gold contacts using a combined atomic force microscope and transmission electron microscope. Applied Surface Science 188, 460-466 (2002)

[80] Martínez, E., Andújar, J. L., Polo, M. C., Esteve, J., Robertson, J., Milne, W. I.: Study of the mechanical properties of tetrahedral amorphous carbon films by nanoindentation and nanowear measurements. Diamond and Related Materials 10, 145-152 (2001)

[81] Cho, S.-J., Lee, K.-R., Yong Eun, K., Hee Hahn, J., Ko, D.-H.: Determination of elastic modulus and Poisson's ratio of diamond-like carbon films. Thin Solid Films 341, 207-210 (1999)

[82] Johnson, J. A.: Insights into "near-frictionless carbon films". Journal of Applied Physics 95, 7765-7765 (2004)

[83] Yeldose, B. C., Ramamoorthy, B.: Characterization of DC magnetron sputtered diamond-like carbon (DLC) nano coating. The International Journal of Advanced Manufacturing Technology 38, 705-717 (2007)

[84] Maugis, D.: Contact, Adhesion, and Rupture of Elastic Solids, Springer, Berlin ; New York (2000)

[85] Bhushan, B., Dandavate, C.: Thin-film friction and adhesion studies using atomic force microscopy. Journal of Applied Physics 87, 1201-1201 (2000)

[86] Carpick, R. W., Flater, E. E., Sridharan, K.: The effect of surface chemistry and structure on nano-scale adhesion and friction. Polymeric Materials: Science & Engineering, 198-198 (2004)

[87] Company, F. E. I.: Tecnai F20/F30 Operating Manual, FEI Company, The Netherlands (1999)

[88] Adliene, D., Laurikaitiene, J., Kopustinskas, V., Meskinis, S., Sablinskas, V.: Radiation induced changes in amorphous hydrogenated DLC films. Materials Science and Engineering: B 152, 91-95 (2008)

[89] Lockwood, A. J., Inkson, B. J.: In situ TEM nanoindentation and deformation of Si-nanoparticle clusters. Journal of Physics D: Applied Physics 42, 035410 (2009)

[90] Kizuka, T., Yamada, K., Deguchi, S., Naruse, M., Tanaka, N.: Cross-sectional time-resolved high-resolution transmission electron microscopy of atomic-scale contact and noncontact-type scannings on gold surfaces. Physical Review B 55, R7398-R7401 (1997)

[91] Bobji, M. S., Pethica, J. B., Inkson, B. J.: Indentation mechanics of Cu–Be quantified by an in situ transmission electron microscopy mechanical probe. Journal of Materials Research 20, 2726-2732

M2723 - 2710.1557/JMR.2005.0332 (2005)

[92] Johnson, J. A., Holland, D., Woodford, J. B., Zinovev, A., Gee, I. A., Eryilmaz, O. L., Erdemir, A.: Top-surface characterization of a near frictionless carbon film. Diamond and Related Materials 16, 209-215 (2007)

[93] Fontaine, J., Donnet, C., Grill, A., LeMogne, T.: Tribochemistry between hydrogen and diamond-like carbon films. Surface and Coatings Technology 146-147, 286-291

[94] Donnet, C., Belin, M., Augé, J. C., Martin, J. M., Grill, A., Patel, V.: Tribochemistry of diamond-like carbon coatings in various environments. Surface and Coatings Technology 68-69, 626-631 (1994)

[95] Sánchez-López, J., Donnet, C., Belin, M., Le Mogne, T., Fernández-Ramos, C., Sayagués, M. J., Fernández, A.: Tribochemical effects on CNx films. Surface and Coatings Technology 133-134, 430-436 (2000)

[96] Li, H., Xu, T., Wang, C., Chen, J., Zhou, H., Liu, H.: Effect of relative humidity on the tribological properties of hydrogenated diamond-like carbon films in a nitrogen environment. Journal of Physics D: Applied Physics 38, 62-69 (2005)

[97] Yen, B. K.: Influence of water vapor and oxygen on the tribology of carbon materials with sp(2) valence configuration. Wear 192, 208-215 (1996)

[98] Park, S.: Tribochemical reaction of hydrogenated diamond-like carbon films: a clue to understand the environmental dependence. Tribology International 37, 913-921 (2004)

[99] Pham, D.-C., Ahn, H.-S., Oh, J.-E., Yoon, E.-S.: Tribochemical interactions of Si-doped DLC film against steel in sliding contact. Journal of Mechanical Science and Technology 21, 1083-1089 (2007)

[100] Olsen, J. E., Fischer, T. E., Gallois, B.: In situ analysis of the tribochemical reactions of diamond-like carbon by internal reflection spectroscopy. Wear 200, 233-237 (1996)

[101] Kim, D. S., Fischer, T. E., Gallois, B.: The effects of oxygen and humidity on friction and wear of diamond-like carbon films. Surface and Coatings Technology 49, 537-542 (1991)

[102] Hon, S., Mathias, W., Zygmunt, R., Czeslaw, K., Michael, F., Joz¡e, V. i., Wilfred, T., Peter, K., Ilia, B., Zinaida, I., Ruvim, Z., Matgorzata, Z.-M., Jeffrey, H., Einar, B., Asgeir, B. Corrosion and Its Impact on Wear Processes. Surface Modification and Mechanisms. CRC Press, 2004.

[103] Martínez-Martínez, D., Kolodziejczyk, L., Sánchez-López, J. C., Fernández, A.: Tribological carbon-based coatings: An AFM and LFM study. Surface Science 603, 973-979 (2009)

[104] Tsuchitani, S., Morishita, S., Kaneko, R., Hirono, S., Umemura, S.: Evaluation of a Lightly Scratched Amorphous Carbon Surface by Contact Resistance of a Conductive Diamond Tip and the Carbon Surface. Tribology Letters 15, 107-113 (2003)

[105] Prioli, R., Chhowalla, M., Freire, F. L.: Friction and wear at nanometer scale: a comparative study of hard carbon films. Diamond and Related Materials 12, 2195-2202 (2003)

[106] R, C.: An AFM study of single-contact abrasive wear: The Rabinowicz wear equation revisited. Wear 267, 1772-1776 (2009)

[107] Papakonstantinou, P., Zhao, J. F., Richardot, A., McAdams, E. T., McLaughlin, J. A.: Evaluation of corrosion performance of ultra-thin Si-DLC overcoats with electrochemical impedance spectroscopy. Diamond and Related Materials 11, 1124-1129

[108] Wang, D.-Y., Chang, C.-L., Ho, W.-Y.: Oxidation behavior of diamond-like carbon films. Surface and Coatings Technology 120-121, 138-144 (1999)

[109] Bennewitz, R., Dickinson, J. T.: Fundamental Studies of Nanometer-Scale Wear Mechanisms. MRS Bulletin 33, 1174-1180

M1173 - 1110.1557/mrs2008.1248 (2008)

[110] McDevitt, N. T., Donley, M. S., Zabinski, J. S.: Utilization of Raman-Spectroscopy in Tribochemistry Studies. Wear 166, 65-72 (1993)

[111] Marks, L. D.: Direct Imaging of Carbon-Covered and Clean Gold (110) Surfaces. Phys Rev Lett 51, 1000-1002 (1983)

[112] Newsome, D. S.: The Water-Gas Shift Reaction. Catalysis Reviews 21, 275-318 (1980)

[113] Blanksby, S. J., Ellison, G. B.: Bond Dissociation Energies of Organic Molecules. Accounts of Chemical Research 36, 255-263 (2003)

[114] Prasad, B. K., Prasad, S. V.: Abrasion-induced microstructural changes during low stress abrasion of a plain carbon (0.5% C) steel. Wear 151, 1-12 (1991)

[115] M'ndange-Pfupfu, A., Marks, L. D.: A Dislocation-Based Analytical Model for the Nanoscale Processes of Shear and Plowing Friction. Tribology Letters 39, 163-167 (2010)

[116] Camara, C. G., Escobar, J. V., Hird, J. R., Putterman, S. J.: Correlation between nanosecond X-ray flashes and stick-slip friction in peeling tape. Nature 455, 1089-U1087 (2008)

[117] Santander-Syro, A. F., Copie, O., Kondo, T., Fortuna, F., Pailhes, S., Weht, R., Qiu, X. G., Bertran, F., Nicolaou, A., Taleb-Ibrahimi, A., Le Fevre, P., Herranz, G., Bibes, M., Reyren, N., Apertet, Y., Lecoeur, P., Barthelemy, A., Rozenberg, M. J.: Two-dimensional electron gas with universal subbands at the surface of SrTiO(3). Nature 469, 189-193 (2011)

[118] Bowden, F. P., Moore, A. J. W., Tabor, D.: The Ploughing and Adhesion of Sliding Metals. Journal of Applied Physics 14, 80-91 (1943)

[119] Bull, S. J.: Can scratch testing be used as a model for the abrasive wear of hard coatings? Wear 233-235, 412-423 (1999)

[120] Malzbender, J., de With, G.: Sliding indentation, friction and fracture of a hybrid coating on glass. Wear 236, 355-359 (1999)

[121] Komvopoulos, K.: Sliding Friction Mechanisms of Boundary-Lubricated Layered Surfaces: Part II—Theoretical Analysis. Tribology Transactions 34, 281 - 291-281 - 291 (1991)

[122] Scholz, C. H., Engelder, J. T.: The role of asperity indentation and ploughing in rock friction -- I : Asperity creep and stick-slip. International Journal of Rock Mechanics and Mining Science & Geomechanics Abstracts 13, 149-154 (1976)

[123] Nam, P. S.: Tribophysics, Prentice-Hall, (Englewood Cliffs, N.J) (1986)

[124] Jaffer, F. Experimental evaluation of sliding friction coefficients for aerospace applications.

[125] Tas, N. R., Gui, C., Elwenspoek, M.: Static friction in elastic adhesion contacts in MEMS. Journal of Adhesion Science and Technology 17, 547-561 (2003)

[126] Hertz, H.: Ueber die Berührung fester elastischer Körper. J Reine Angew Math 92, 156-171 (1882)

[127] Indenbom, V. L., Lothe, J.: Elastic strain fields and dislocation mobility, North-Holland, Amsterdam ; New York (1992)

[128] Al'shitz, V. A., Indenbom, V. L.: Dynamic dragging of dislocations. Soviet Physics Uspekhi 18, 1 (1975)

[129] Institut problem, m., Samsonov, G. V.: Handbook of the physicochemical properties of the elements, IFI/Plenum, New York (1968)

[130] Frost, H. J., Ashby, M. F.: Deformation-mechanism maps : the plasticity and creep of metals and ceramics, Pergamon Press, Oxford [Oxfordshire] ; New York (1982)

[131] Chang, Y. A., Himmel, L.: Temperature Dependence of the Elastic Constants of Cu, Ag, and Au above Room Temperature. Journal of Applied Physics 37, 3567-3572 (1966)

[132] Overton, W. C., Jr., Gaffney, J.: Temperature Variation of the Elastic Constants of Cubic Elements. I. Copper. Physical Review 98, 969-977 (1955)

[133] Goddard, J., Wilman, H.: A theory of friction and wear during the abrasion of metals. Wear 5, 114-135 (1962)

[134] Szeri, A. Z.: Fluid Film Lubrication (1998)

[135] Liu, Z., Sun, J., Shen, W.: Study of plowing and friction at the surfaces of plastic deformed metals. Tribology International 35, 511-522 (2002)

[136] Read, W. T., Shockley, W.: Dislocation Models of Crystal Grain Boundaries. Physical Review 78, 275-289 (1950)

[137] Shan, Z., Stach, E. A., Wiezorek, J. M. K., Knapp, J. A., Follstaedt, D. M., Mao, S. X.: Grain Boundary-Mediated Plasticity in Nanocrystalline Nickel. Science 305, 654-657 (2004)

[138] Ke, M., Hackney, S. A., Milligan, W. W., Aifantis, E. C.: Observation and measurement of grain rotation and plastic strain in nanostructured metal thin films. Nanostructured Materials 5, 689-697 (1995)

[139] Ohmura, T., Minor, A. M., Stach, E. A., Morris, J. W.: Dislocation-grain boundary interactions in martensitic steel observed through in situ nanoindentation in a transmission electron microscope. Journal of Materials Research 19, 3626-3632 (2004)

[140] Van Swygenhoven, H., Derlet, P. M.: Grain-boundary sliding in nanocrystalline fcc metals. Physical Review B 64, 224105 (2001)

[141] Majumdar, B. S., Burns, S. J.: A Griffith crack shielded by a dislocation pile-up. International Journal of Fracture 21, 229-240 (1983)

[142] Pande, C. S., Masumura, R. A., Armstrong, R. W.: Pile-up based hall-petch relation for nanoscale materials. Nanostructured Materials 2, 323-331 (1993)

[143] Van Swygenhoven, H.: Grain Boundaries and Dislocations. Science 296, 66-67 (2002)

[144] Klemens, P. G.: The Scattering of Low-Frequency Lattice Waves by Static Imperfections. Proceedings of the Physical Society Section A 68, 1113 (1955)

[145] Carruthers, P.: Scattering of Phonons by Elastic Strain Fields and the Thermal Resistance of Dislocations. Physical Review 114, 995-1001 (1959)

[146] Kogure, Y., Hiki, Y.: Scattering of Lattice Waves by Static Strain Fields in Crystals. Journal of the Physical Society of Japan 36, 1597

[147] Northrop, G. A., Cotts, E. J., Anderson, A. C., Wolfe, J. P.: Anisotropic phonon-dislocation scattering in deformed LiF. Physical Review B 27, 6395-6408 (1983)

[148] Rui, W., Shaofeng, W., Xiaozhi, W.: Edge dislocation core structures in FCC metals determined from ab initio calculations combined with the improved Peierls–Nabarro equation. Physica Scripta 83, 045604 (2011)

[149] Stephan, H., Ramesh, K. T., Baron, G., Schwerdtfeger, W. K.: Nanomaterials: Mechanics and Mechanisms, Springer (2009)

[150] Hikata, A., Deputat, J., Elbaum, C.: Dislocation Interactions with Phonons in Sodium Chloride in the Temperature Range 70-300°K. Physical Review B 6, 4008-4013 (1972)

[151] Ohashi, K.: Scattering of Lattice Waves by Dislocations. Journal of the Physical Society of Japan 24, 437

[152] Bhushan, B.: Handbook of Micro/Nanotribology, CRC Press, Boca Raton (1995)

[153] Komanduri, R.: Some clarifications on the mechanics of chip formation when machining titanium alloys. Wear 76, 15-34 (1982)

Appendix

The Nanofactory HS-100 STM-TEM holder is a versatile tool, but also very sensitive. Here I will go over some practical aspects to using the holder to perform sliding experiments in the TEM. The holder can be used outside the microscope, although noise will prevent accurate measurements. It can be useful, however to observe the hat moving during coarse motion of different amplitudes – in particular, the effect of gravity.

Often, it is worthwhile to connect the sample holder electronics before inserting it into the microscope. This allows for a readiness check as well as the ability to move the probe tip upwards into a safer position for insertion. Note that connecting the electronics will reset the piezoelectric tube to neutral and if it has not been previously zeroed out, this may cause the probe tip to jump. Because of the rotation and jostling the sample holder will experience during insertion, the tip and sample can easily make a hard, unwanted contact. The best ways to avoid this are by angling the tip away from the sample prior to entry and to perform the insertion as gently and smoothly as possible.

Inside the microscope, locating the probe is usually the first matter at hand. If it is not immediately visible in low-magnification mode, then generally using the coarse motion in the forward direction will make it visible shortly. Keep in mind that any time the tip is moved forward, gravity pulls it downward as well, so it is sometimes prudent to periodically move the tip upward manually to keep from making unwanted contact. Also remember that the coarse

motion amplitude and frequency can be controlled through the software, and at first high amplitude pulses can be used, then scaled down as the probe gets closer to the sample.

Once the probe is located, check its tip to make sure that the point has maintained a decent sharpness. If all is well, it is useful to survey the sample for potential areas that the tip will be able to reach – this may change from experiment to experiment. Keep in mind that for the ideal sliding experiment the tip must be able to move laterally back and forth, whereas for a nanoindentation-like experiment it will move forwards and backwards. If there is a suitable area within reach, then the probe can be moved closer. One further precaution is that only the tip of the probe can be seen. The base of the probe, especially if it is much thicker than the tip, can impact the sample or grid outside your field of view; this is usually noticed by the entire sample moving as you attempt to move the tip, and the probe either needs to be retracted or raised in that event.

Positioning the probe in the z-axis is commonly done by using the high voltage or objective lens current wobble, which will move the image back and forth through defocus. Parts of the image at different defoci will then wobble with different magnitudes. One approach is to focus on the desired sample area, so that it is stationary under the wobbler, then move the probe closer by minimizing the probe's wobble. Because of the two-dimensional view, the probe's position in the x-y plane cannot be accurately determined until it matches the sample's defocus.

Contact with the sample can be seen, as the probe will visibly adhere to the sample once it has been brought within several nanometers. An easy way to see is through the motion of the entire sample – if the entire sample field jostles when the tip is moved closer, continues to move

while the tip is moved further, but stops when the tip is withdrawn, then this is likely a solid, repeatable contact.

Making sure the sliding contact is steady and repeatable is done using the piezoelectric control. A gamepad controller is ideal for moving the tip back and forth a certain amount, as it is less awkward and perhaps more precise than the mouse and keyboard controls. When stopping periodically to take EELS spectra, be careful not to move the sample stage at all, or change the beam intensity. EFTEM lenses can often be used to focus the beam into the GIF aperture, and then reset to resume imaging. It is important to keep track of the energy filter settings, as zero-loss, core-loss, or other various regions may be switched to. In order to prevent the EELS signal from damaging the CCD, do not allow the zero-loss peak to be focused into the GIF when the screen is lifted.

Lastly, if the sample does not support the contact or there is some other problem that requires changing the sample, it is advisable to inspect the probe tip before removing it to see if it warrants replacement as well. If the tip needs to be changed but the same sample area is desired, it is important to note the orientation of the grid in the sample holder, or to use a system of landmarks or grid markings to remember certain locations. Most other operation information can be found in the manual, which also contains instructions for calibration, preparation, care, and cleaning.